

MANIPULATION AND CHARACTERIZATION OF THIN-FILM INTERFACIAL  
CHEMISTRY: SOL-GEL DEPOSITION AND SINGLE  
MOLECULE TRACKING EXPERIMENTS

by

Moussa Barhoum

A dissertation submitted to the faculty of  
The University of Utah  
in partial fulfillment of the requirements for the degree of

Doctor of Philosophy

Department of Chemistry

University of Utah

May 2012

Copyright © Moussa Barhoum 2012

All Rights Reserved



## ABSTRACT

Single molecule trajectories of 1,1'-dioctadecyl-3,3,3'-tetramethylindocarbocyanine perchlorate (DiI) fluorophores diffusing on planar supported 1,2-dimyristoyl-sn-glycero-3-phosphocholine (DMPC) lipid bilayers imaged through total internal reflection fluorescence (TIRF) microscopy at different temperatures are investigated. The spatial resolution limit for detecting molecular motion is evaluated by characterizing the apparent motion which arises from the limited signal-to-noise ratio (S/N) of imaged and simulated stationary DiI molecules. Statistical criteria for reliably distinguishing molecular motion from stationary molecules using F-test statistics, including the computation of local signal-to-noise ratios are then established and used for reliably detecting subdiffraction motion of DiI molecules on DMPC.

The same single molecule tracking concept is used in investigating the temperature dependence of subdiffraction diffusional confinement of single Rhodamine 6G molecules in polymer brushes of poly (N-isopropylacrylamide), pNIPAAm, above and below its lower critical solution temperature (LCST) of 32 °C. Reliably distinguishing subdiffraction molecular motion from stationary events is crucial in validating the application of single molecule tracking experiment in probing nanometer-sized hydrophobic environments of polymer structure.

A versatile and rapid sol-gel technique for the fabrication of high quality one-dimensional photonic bandgap materials was developed. Silica/titania multilayer

materials are fabricated by a sol-gel chemistry route combined with dip-coating onto planar or curved substrate. A shock-cooling step immediately following the thin film heat-treatment process is introduced. The versatility of this sol-gel method is demonstrated by the fabrication of various Bragg stack-type materials with fine-tuned optical properties. Measured optical properties show good agreement with theoretical simulations confirming the high quality of these sol-gel fabricated optical materials.

Finally, magnetic functionalization studies of sol-gel derived Co-ion doped titania thin films using superconducting quantum interference device (SQUID) magnetometry and an attempt to measure their magneto-optical properties using a home-built Faraday rotation setup are discussed. The experimental limitations in reliably measuring magnetization responses of these thin films are introduced and discussed in detail.

The summary and outlook chapters summarize the scientific significance of each research project and briefly introduce ongoing research based on the work and the results presented in this dissertation.

## TABLE OF CONTENTS

ABSTRACT .....	iii
LIST OF FIGURES .....	vii
ACKNOWLEDGEMENTS .....	xiii
1. INTRODUCTION .....	1
1.1 Interfaces and Interfacial Processes .....	1
1.2 Single Molecule Studies of Interfacial Processes .....	2
1.3 TIRF Microscopy and Single Molecule Tracking .....	3
1.4 Manipulating Interfaces via Sol-Gel .....	6
1.5 Sol-Gel Chemistry and Sol-Gel Thin Film Deposition.....	8
1.6 Thesis Overview .....	11
1.7 References.....	13
2. STATISTICAL CRITERIA FOR DETECTING MOLECULAR MOTION IN SINGLE MOLECULE DIFFUSIONAL TRAJECTORIES .....	22
2.1 Introduction.....	22
2.2 Materials and Methods.....	24
2.3 Results and Discussion .....	28
2.4 Conclusion .....	36
2.5 References.....	37
3. SINGLE MOLECULE TRACKING STUDIES OF LOWER CRITICAL SOLUTION TEMPERATURE TRANSITION BEHAVIOR IN POLY(N-ISOPROPYLACRYLAMIDE).....	48
3.1 Introduction.....	48
3.2 Experimental Section .....	50
3.3 Results and Discussion .....	55
3.4 Conclusion .....	66
3.5 References.....	67
4. RAPID SOL-GEL FABRICATION OF HIGH QUALITY THIN-FILM STACKS ON PLANAR AND CURVED SUBSTRATES .....	79

4.1 Introduction.....	79
4.2 Experimental Section .....	83
4.3 Results and Discussion .....	87
4.4 Conclusion .....	94
4.5 References.....	96
5. MAGNETIC FUNCTIONALIZATION STUDIES AND MAGNETO- OPTICAL MEASUREMENTS OF SOL-GEL DERIVED TITANIA AND SILICA THIN FILMS.....	111
5.1 Introduction.....	111
5.2 Experimental Section .....	114
5.3 Results and Discussion .....	117
5.4 Conclusion and Outlook .....	124
5.5 References.....	125
6. SUMMARY AND OUTLOOK.....	140
6.1 Summary .....	140
6.2 Outlook .....	142
6.3 References.....	143

## LIST OF FIGURES

### Figure

- 1.1 Schematic of a TIRF microscope. The evanescent wave penetration depth for the used setup is around 150 nm. Single DiI molecules are excited within the evanescent wave and show additional quantum yield increase when intercalated into the lipid bilayer.....19
- 1.2 Single molecule tracking cycle: A single molecule within a region of interest (ROI) (a) is fitted to a 2D Gaussian function (b) (b1 and b2 represent the 3D plot of the Gaussian fit and the background of the fit).The centroid of the fit represents the subdiffraction position of the single molecule(c). The position is then recorded as a trajectory point (d).....20
- 1.3 A schematic of the sol-gel dip-coating process highlighting the different stages in the formation of a solid gel network .....21
- 2.1 Plot of the mean standard deviation in position-difference (red curve) and the standard deviation in apparent step sizes (green curve) of simulated stationary single molecules at varying S/N. Scatter plot of the apparent step sizes are generated from the same data set (blue squares).....40
- 2.2 Raw data image (2a) and 3D contour plot of stationary DiI molecules fitted to 2D Gaussian functions and their corresponding local S/Ns (2b). The local S/N was determined by computing the ratio of the fitted Gaussian amplitude to the standard deviation of the background. ....41
- 2.3 Histogram plots of the apparent step sizes of (A) simulated and (B) experimentally measured stationary DiI molecules. Fits are to equation 3.....42
- 2.4 Apparent motion plot generated from simulated stationary DiI molecules and a 99% F-test confidence boundary (red line) for no detection of molecular motion (A). Additional scatter plot of the apparent motions of imaged adsorbed DiI molecules (B). ....43



2.5	Trajectory plot of a single DiI fluorophore diffusing on DMPC at room temperature (A). Circle radii represent the boundary for no detection of molecular motion (green segments). Circle color represents the magnitude of the local S/N. (B) Apparent motion error-plot for the corresponding trajectory in (A). Green squares represent the apparent steps and the blue squares the detected steps in the trajectory. ....	44
2.6	Plots of representative DiI trajectories on a DMPC bilayer at varying temperatures and their corresponding apparent motion error plots. The calculated diffusion coefficient at 8°C represents an apparent diffusion coefficient. ....	45
2.7	Zoom-in (red-square in Figure inset) of the DiI trajectory on DMPC at 37°C from Figure 2.6 (Figure inset) including three original images with varying local S/N(A). Local S/N ratios are coded by the frame color of the images. The number in the images represent the trajectory position the image was taken. ....	46
2.8	Automated tracking data from DiI diffusing on DMPC at 37°C. Trajectory table includes the computational results of the local S/N of the trajectory. Three original images represent varying diffusional or photo-physical behavior detected by significant variation in the computed local S/N of the automated tracking software. ....	47
3.1	Ellipsometric measurements of thickness normalized to dry thickness (black) and refractive index (blue) as a function of temperature for hydrated pNIPAAm synthesized on Si. Films displayed 45 nm dry thickness. All films exhibited a ~165% increase from dry to expanded and an 85% decrease from expanded to collapsed hydrated states, which corresponds to single spot measurements on a 80 nm dry sample (not reported). At each temperature, measurements were averaged over at least 10 spots with the standard deviations reported as error bars. ....	71
3.2	Reconstructed SMT trajectories longer than 50 frames for R6G in pNIPAAm on glass at 23°C (polymer brush in expanded state); (Inset) 20 μm x 20 μm expanded view. Different colors represent different trajectories, which may appear to overlap but in fact occur at different times. ....	72
3.3	Reconstructed SMT trajectories longer than 50 frames for R6G in pNIPAAm on glass at 32°C (polymer brush in collapsed state); (Inset) 20 μm x 20 μm expanded view. Different colors represent different trajectories, which may appear to overlap but in fact occur at different times. ....	73

3.4	Root mean square displacement (for 30 ms exposure) for R6G molecules adsorbed to a surface site as a function of the S/N ratio of the single molecule fluorescent image for both simulated (black) and experimental (blue) data. Red squares correspond to the experimentally determined rms displacement and S/N for confined R6G molecules in pNIPAAm both below and above the LCST, as noted. Error bars shown for rms and S/N for all points are the standard error of the mean. ....	74
3.5	Confinement level analysis results for two separate samples of R6G probes in the same pNIPAAm sample on glass at 23°C (dark red, light red) and 32°C (dark blue, light blue). ....	75
3.6	Confinement level analysis for R6G in pNIPAAm at 23°C (dark red, light red) and 32°C (dark blue, light blue), two trials each. Traces are offset for clarity and the inset emphasizes the difference between the tail at 23°C and 32°C. (a) Normalized histograms of the duration of confined events, with fits (dashed lines) for single (23°C) and double (32°C) Lorentzian functions. (b) Distribution of the radius of confined zones. ....	76
3.7	Radius of gyration evolution for trajectories at 23°C (a) and 32°C (b) of R6G in pNIPAAm on glass. Only trajectories longer than 150 steps only are included. ....	77
3.8	Histograms of the final R <sub>g</sub> value for each molecule in SMT movies 23°C (dark and light red) and 32°C (dark and light blue). ....	78
4.1	Thin-film deposition cycle for the fabrication of sol-gel thin-film layers. a) Step 1: dip-coating; b) step 2: dry-blowing; c) step 3: heat-treatment (annealing); d) step 4: shock-cooling. Right. Flow chart depicting the main steps of the deposition cycle. ....	100
4.2	Optical micrographs of 12 alternating silica/titania thin-film layers deposited onto a silicon (100) wafer. Top: Samples fabricated including (a) and omitting (b) the dry-blowing step in the deposition cycle (Figure 4.1). Bottom: Samples fabricated including (c) and omitting (d) the shock-cooling step in the deposition cycle (Figure 4.1). ....	101
4.3	Photograph and cross-sectional SEM image of a thin-film Bragg stack consisting of 14 alternating layers of silica (88±2 nm; dark layers) and titania (75±2 nm; bright layers) deposited onto a silicon (100) wafer (a,b) Corresponding optical reflection spectrum (solid line) and simulated spectrum (c) (dotted line). ....	102
4.4	Photographs of thin-film Bragg stacks consisting of 12 alternating layers of silica (88±2 nm; dark layers) and titania (75±2 nm; bright layers)	

	deposited onto (a) a planar borosilicate glass substrate and (b) a curved quartz-glass substrate. c, d) Corresponding optical reflection spectra (solid lines) of the stacks on (c) a planar borosilicate glass substrate and (d) a curved quartz-glass substrate. Simulated spectra are given as dotted lines.....	103
4.5	Optical reflection spectra of a Bragg stack of 12 alternating silica/titania layers. The silica layer thickness was held constant at $88\pm 2$ nm, whereas the titania layer thickness was varied between $60\pm 2$ and $80\pm 2$ nm, as indicated in the figure. The simulated spectrum is given as dotted line.....	104
4.6	TEM image of a nanoporous titania thin-film sample a). Some of the pores are indicated by arrows. b) Optical reflection spectra of three 14-layer silica/titania Bragg stacks with differing refractive indices of the titania layer deposited onto a silicon (100) substrate. The titania layer refractive indices are $2.34\pm 0.02$ (red spectrum), $2.1\pm 0.1$ (green spectrum), and $1.8\pm 0.1$ (blue spectrum). Simulated spectra are given as dotted lines.....	105
4.7	Cross-sectional SEM image a) and optical reflection spectrum b) of a Fabry-Perot microcavity structure deposited onto a silicon (100) substrate. The microcavity is composed of a central silica defect layer with a thickness of $176\pm 2$ nm sandwiched between two 8-layer silica/titania Bragg stacks with silica and titania thicknesses of $88\pm 2$ nm and $70\pm 2$ nm, respectively. The optical cavity mode occurs at a wavelength position of 568 nm. The simulated spectrum is given as dotted line.....	106
4.8	Cross-sectional SEM image a) and optical reflection spectrum b) of an asymmetric 25-layer silica/titania Bragg stack deposited onto a silicon (100) substrate. The silica layer thickness was held constant at $44\pm 2$ nm, while the titania layer thickness was varied in 5 nm steps from $68\pm 2$ nm to $88\pm 2$ nm and back to $68\pm 2$ nm. The simulated spectrum is given as dotted line.....	107
4.9	Graphs showing thickness of a) silica and b) titania thin films as a function of ethanol content of the respective precursor solutions (in volume percent). Film thicknesses were determined after a single deposition cycle (black) and after an additional heat treatment for at least 1 hour at $500\text{ }^{\circ}\text{C}$ (red). For example, to fabricate a silica film with a thickness of $88\pm 2$ nm (arrow in (a)), 5 mL of the original silica stock solution was diluted with 15 mL ethanol. Likewise, to fabricate a $80\pm 2$ nm titania film (arrow in (b)), 16 mL of titania stock solution were diluted with 4 mL of ethanol.....	108

4.10	Photograph of a large-area (5x4 cm) thin-film Bragg stack consisting of 12 alternating layers of silica (88±2 nm) and titania (70±2 nm) deposited onto a silicon (100) wafer. ....	109
4.11	Optical reflection spectra of three thin-film Bragg stacks consisting of 12 alternating layers of silica and titania with thicknesses of 88±2 nm and 70±2 nm, respectively, deposited onto a silicon (100) wafer. The three samples were fabricated at different times but under the same experimental conditions (i.e., precursor solution composition, dip-coating parameters, drying and heat treatments) and demonstrate the excellent reproducibility of the deposition and processing method.....	110
5.1	XRD pattern (black line) for a sol-gel derived TiO <sub>2</sub> thin film (5.1A) and powder (5.1B) calcined at 450°C for 3 hours. Simulated XRD patterns of anatase TiO <sub>2</sub> are additionally plotted for comparison (red spectrum). ....	129
5.2	RT SQUID hysteresis measurement of a 0.5% Co-doped TiO <sub>2</sub> thin-film sample exhibiting a ferromagnetic response. Inset: Zoomed-in region between ±100 Oe shows a coercivity of ~50 Oersted.....	130
5.3	RT SQUID hysteresis measurements of 0.5% Co-doped mesoporous TiO <sub>2</sub> thin-film sample exhibiting ferromagnetic response (5.3A). Inset: Zoomed-in region between ±100 Oe shows a coercivity of ~50 Oersted. (5.3B) TEM image of a mesoporous sol-gel derived TiO <sub>2</sub> thin-film using Pluronic P123 surfactant chemistry.....	131
5.4	RT SQUID hysteresis measurements of a 0.5% Co-doped TiO <sub>2</sub> thin-film sample exhibiting ferromagnetic response superimposed on a paramagnetic response (5.4A), and measurement of a 0.5% Co-doped TiO <sub>2</sub> thin-film sample exhibiting a purely paramagnetic response (5.4B). Inset of (5.4A): Zoomed-in region between ±100 Oe shows a coercivity of ~50 Oersted.....	132
5.5	A schematic diagram of the home-built Faraday rotation setup utilized in the magneto-optical studies of thin films.....	134
5.6	Magneto-optical measurements of (5.6A) 0.17mm thick VWR glass coverslip and (5.6B) 1nm thick equiatomic CoPt thin-film layer deposited on glass by chemical vapor deposition. ....	135
5.7	Faraday-signal comparison of (5.7A) 0.5% Co-doped TiO <sub>2</sub> and (5.7B) 0.5% Mn-doped TiO <sub>2</sub> (both thin-films deposited on glass) to the glass substrate. ....	136
5.8	VSM hysteresis curve measurements at 400K (black) and 20K (red) of 77nm thick TiO <sub>2</sub> thin-film sample deposited on Si (100) waver (5.8A)	

	and field cooling measurements at a constant magnetic field of 1000 Oe (5.8B). .....	137
5.9	VSM hysteresis curve measurements at 400K (black) and 20K (red) of 77nm thick 0.5% Co-doped TiO <sub>2</sub> thin-film sample deposited on Si (100) waver (5.9A) and field cooling measurements at a constant magnetic field of 1000 Oe (5.9B). .....	138
5.10	VSM hysteresis curve measurements at 400K (black) and 20K (red) of 385nm thick 0.5% Co-doped TiO <sub>2</sub> thin-film sample deposited on Si (100) waver (5.10A) and field cooling measurements at constant magnetic field of 1000 Oe (5.10B). .....	139

## ACKNOWLEDGEMENTS

I would like to take this opportunity to thank everybody who has contributed to the research work presented in this dissertation. This includes foremost my research advisors: I have been privileged to be a group member of two stimulating research groups with inspiring group leaders. I would love to express my sincerest gratitude to both PhD advisors Dr. Joel M. Harris and Dr. Michael H. Bartl. Mike and Joel have been challenging me in their own respective ways and made me the best I can be. Mike inspired me to be scientifically curious and try new things out while Joel pushed me to think harder before jumping into analytical conclusions. Acquiring these tools from both great advisors is a valuable asset that surely will serve me in my ongoing career and in life in general. THANK YOU Joel and THANK YOU Mike!

Not only was my PhD career-path unique by having two research advisors simultaneously but also by the stimulating scientists who have surrounded me and have helped me to develop further and become the researcher I am today. My former Diplom-advisor, collaborator, visitor and friend Charly (Prof. Karl-Heinz Gericke) from the Technische Universität Braunschweig taught me many valuable things from scientific coding to the history of mankind in general. It was always fun to visit Charly in Germany or to have him over in SLC. Thank you for everything Charly! I would also love to express my gratitude to Dr. Peter Flynn. Peter gave me unlimited access to his lab and

and especially to his snack bar to keep my sugar level up during the long working hours. It was always fun to talk to Peter about everything and I will surely miss his conversation opening phrase: “Moussa, what’s happening man?” He further gave me a unique insight about life in academia and compared it to life in industry and therefore helped me to decide my career path less blinded.

My committee members Dr. Michael Morse, Dr. Valeria Molinero, Dr. John Lupton and Dr. Steve Blair were all helpful in shaping my PhD endeavor and made sure that I will finish in a timely manner despite working on two different research topics.

I would love to acknowledge past and current members of the Harris and Bartl research labs, especially my colleagues who became my friends and with whom I had a lot of fun with outside the Department: Dr. Emily Heider, Amy Carr-Spencer, Dr. Christopher Fox, Dr. David Riassetto and Dr. Jacqueline Siy-Ronquillo.

Special thanks go to Jo Hoovey who was always there to help me with the bureaucratic challenges I faced! Dale Heisler and Dennis Romney helped me with instrumentation and machining parts.

I would also love to acknowledge my collaborators Dr. Paul Bohn, Dr. Lindsay Elliott and Dr. Karine Chesnel and all the people who trained me or helped me with my research. This includes Alonso Martinez, Dr. Mohamed Shadid, Susi Podhajsky, Amber McConnell, Jacob Morrill and Dr. Robert Horton. All members of my family, relatives and close friends who were always available to support me deserve my greatest appreciation! Thank you all for everything!

## CHAPTER 1

### INTRODUCTION

#### 1.1 Interfaces and Interfacial Processes

Understanding and manipulating interfaces and interfacial processes is an essential part in developing next generation technologies. Considering an invention or a discovery a potential candidate for next generation technology is often judged by how well it performs or how well it possibly could perform in the near future. Often, the rate limiting step in performance is connected to inefficient interfacial processes. By investigating the nature of these processes, insights about underlying mechanisms can be gained and used in manipulating these processes to increase performance. Examples illustrating this concept are numerous and range, for example, from dye-sensitized solar cells<sup>1-3</sup> to improved drug-delivery vehicles.<sup>4-6</sup>

This dissertation deals with characterization and manipulation of interfaces. While the characterization of interfaces using single molecule studies was carried out in the research laboratory of Dr. Joel Harris, the manipulation of interfaces using sol-gel chemistry was carried out in the research laboratory of Dr. Michael Bartl. In the first part of the introduction the fluorescence microscopy technique and the tracking strategy for evaluating and investigating single-molecule diffusional trajectories used in this dissertation is presented and discussed. The second part of this dissertation deals with sol-



gel science and the dip-coating process for fabricating sol-gel derived thin-film stacks on various substrates. Furthermore, challenges in utilizing the dip coating technique for the deposition of high-quality sol-gel derived thin films are discussed.

### 1.2 Single Molecule Studies of Interfacial Processes

Single molecule studies of interfacial processes have evolved as a powerful tool in elucidating complex interfacial processes, usually not accessible in ensemble measurements.<sup>7-11</sup> The high spatial and temporal resolution of single-molecule studies allow for investigating molecular interaction dynamics between single probe molecules and a target structure.<sup>12-14</sup> Additionally, by selectively choosing fluorophores with specific chemical and physical properties, insights about the nature of the interaction (for example, hydrophobic versus hydrophilic interactions) between the probe molecule and its surrounding are obtained.<sup>11,15-17</sup> Furthermore, attaching or intercalating single fluorophores to a target structure allows for investigating the target structure dynamics with minimal perturbation.<sup>18-20</sup>

Single molecule studies have previously been utilized in real-time tracking of biological motors moving in discrete steps along linear proteins or nucleic acids,<sup>21-24</sup> the investigation of chromatographic interfacial dynamics, biological cell membranes<sup>25-27</sup> and artificial membranes.<sup>28-30</sup> The ability to localize stationary single molecules in an image with subdiffraction resolution in three dimension is the basis of the rapidly emerging field of super-resolution spectroscopy.<sup>31-34</sup>

The spatial resolution for a single molecule experiment relies heavily on the sensitivity of the instrumentation and on the emission characteristics of the probe

molecule used for the study.<sup>16</sup> For example, in Chapter 2 the investigation of the lipid bilayer dynamics is investigated as a function of temperature. The probe molecules chosen in this study are fluorescent DiI-C<sub>18</sub> molecules. DiI molecules are commonly used due to their quantum-yield dependence on their surroundings. An increase in quantum yield indicates an increased hydrophobic environment, and is indicative of the probes intercalation into the lipid bilayer.<sup>17</sup> Therefore, information regarding the polarity of the surroundings of the molecule can be additionally utilized in interpreting diffusional behavior of single molecules.

### 1.3 TIRF Microscopy and Single Molecule Tracking

Studying interfacial processes with high temporal and high spatial resolution requires elaborate instrumentation with the following characteristics: The instrumental setup has to have the capability to access and study interfaces, including the capability to probe nanoscale structures. Furthermore, interface selectivity with high spatial resolution and simultaneously high temporal resolution are required. These conditions are optimized in a Total-Internal-Reflection-Fluorescence (TIRF) microscope.<sup>35-38</sup> TIRF microscopy has the unique property of selectively illuminating and exciting single fluorophores within a limited illumination depth (~150nm) from the interface. The limitation in the illumination depth is due to an evanescent field (nonpropagating electromagnetic wave) which is created by internally reflecting an excitation beam at a planar dielectric interface at an angle greater than the critical angle.<sup>39-41</sup> This effect enables high-contrast imaging of single molecules with high temporal resolution using sensitive CCD-cameras.<sup>9,18,42-44</sup> TIRF microscopy has been successfully applied, for example, in measuring surface

densities of bound fluorescent molecules,<sup>18,43</sup> single molecule diffusion studies on lipid bilayers,<sup>9</sup> in poly(N-isopropylacrylamide) polymer structure<sup>11,45</sup> and in the spectroscopic identification of single fluorescent labels.<sup>46</sup>

In TIRF microscopy, the excitation laser is brought through a high numerical-aperture objective at an angle greater than the critical angle of the coverslip/solution interface, resulting in total internal reflection of the excitation laser. According to Snell's law the critical angle  $\theta(c)$  at an interface is defined as:

$$\theta(c) = \sin^{-1} \left( \frac{n_2}{n_1} \right) \quad [1.1]$$

with  $n_2$  being the lower refractive index and  $n_1$  the higher refractive index respectively. The evanescent electric field intensity  $I(z)$  decays exponentially with distance  $z$  according to:

$$I(z) = I_0 e^{-z/d_p} \quad [1.2]$$

with  $I(0)$  being the intensity at the interface ( $z=0$ ) and  $d_p$  the penetration depth into the higher refractive index medium defined as:<sup>47</sup>

$$d_p = \frac{\lambda_i}{4\pi n_1 [\sin^2 \theta_i - (n_2/n_1)^2]^{1/2}} \quad [1.3]$$

As shown in equation 1.3,  $d_p$  is a function of incident angle,  $\theta_i$ , the refractive index ratio, and the incident wavelength of the excitation source. Using the parameters of our

experimental setup with  $\lambda_i=532\text{nm}$ ,  $n_1=1.58$  (borosilicate glass) and  $n_2=1.33$  (water) and  $\theta_i=65-75^\circ$  a penetration depth between 120-140 nm is achieved.

In TIRF microscopy, the excitation laser is brought through a high numerical aperture objective at an angle greater than the critical angle of the glass coverslip/aqueous solution interface. The fluorescence emission of the excited single fluorophores within a 150 nm depth from the interface is then collected with high efficiency through the same objective and imaged onto a CCD camera; see Figure 1.1 for a schematic diagram and experimental imaging parameters. The images are then analyzed using in-house written software in Matlab (Mathworks).

The single molecule tracking procedure is carried out using in-house tracking software written in Matlab (Mathworks). Figure 1.2 illustrates the tracking procedure. First, a region of interest (ROI) (typically 15x15 pixel) is drawn around the image of the single molecule of interest. The diffraction limited intensity profile of the single molecule is then fitted to a 2D Gaussian function according to:<sup>48</sup>

$$I(x, y) = b + A \times \exp \left\{ - \left[ \left( \frac{(x-x_0)}{r_x} \right)^2 + \left( \frac{(y-y_0)}{r_y} \right)^2 \right] \right\} \quad [1.4]$$

Here,  $b$  is the background,  $A$  the amplitude,  $x$  and  $y$  are the image coordinates,  $(x_0, y_0)$  are the center of the fitted Gaussian function, and  $r_x$  and  $r_y$  are the  $1/e$  widths in the two dimensions. The fundamental principle in localizing fluorescent spots - with precision better than the diffraction limit of light - lies in reliably fitting their spots to 2D Gaussian functions. The center of the Gaussian fit represents the subdiffraction localization of the single fluorophore. The region of interest (ROI) is then automatically positioned at this

center and the same single molecule spot in the next consecutive frame is again fitted to a Gaussian function. This procedure repeats until there is no single molecule identified within the ROI or if two and more single molecules appear in the same ROI simultaneously (algorithm stops if certain fitting boundaries are exceeded).

The ability to achieve high signal-to-noise ratios and to locate single fluorophores with subdiffraction precision with millisecond temporal resolution makes TIRF microscopy a powerful tool in single molecule diffusional studies. However, the question of how accurate molecular movement (the difference of two determined x,y-positions) is reliably detected has not been addressed in a satisfactory manner yet. Chapter 2 deals with this issue by analyzing apparent motions of simulated and imaged stationary DiI molecules. This information is then used in establishing statistical criteria for discerning molecular motion from stationary molecules. The established statistic is then used to investigate diffusional behavior of single DiI molecules on supported lipid bilayers deposited on glass and in probing sub-nanometer confinement events in polymer structure of poly(N-isopropylacrylamide) using Rhodamine 6G molecules as probe molecules.

#### 1.4 Manipulating Interfaces via Sol-Gel

Manipulating interfaces has recently regained burgeoning importance since the theoretical ground work for new optical materials was laid by Yablonovitch and John in 1987. In independent works they derived theoretical concepts to manipulate light in unprecedented ways by using three-dimensionally periodic dielectric materials.<sup>49,50</sup> This theoretical work laid the foundation of a novel, exciting and rapidly emerging research

field, termed photonic crystals.<sup>51-53</sup> The underlying principle in manipulating light in unprecedented ways lies in its interaction with periodic materials of constant dielectric periodicity on the order of the wavelength of light.<sup>54,55</sup> Such photonic crystals have been successfully fabricated in one, two and three dimensions using for example mask lithography,<sup>56</sup> layer-by-layer template fabrication using organic chemical vapor deposition,<sup>57</sup> holographic lithography,<sup>58</sup> deep x-ray lithography<sup>59</sup> and multibeam laser interference.<sup>60</sup>

While these fabrication methods are challenging and require mostly cost-intensive elaborate instrumentations an elegant alternative is fabricating the photonic crystals through self-assembly techniques.<sup>61-68</sup> Furthermore, by using self-assembly techniques, high quality nanostructures with subdiffraction feature sizes patterned over a wide range of length scales (from nano- to micrometer) are achieved—length scales usually not accessible using conventional lithography techniques.<sup>68-75</sup> A prominent chemical route in accessing and manipulating nanostructures is through templated<sup>76,77</sup> sol-gel approaches.<sup>76-84</sup> Sol-gel synthesis is a simple, cheap and versatile alternative synthesis method. The relatively mild synthesis conditions and the added flexibility allows for incorporating unprecedented three-dimensional and other hierarchical structures into the sol-gel network.<sup>85,86</sup> A remaining hurdle in the wide spread utilization of sol-gel derived materials is controlling structure uniformity and reproducibility.<sup>87</sup> One specific aspect of this challenge of interest in this dissertation is the crack-formation mechanism occurring during the dip-coating deposition process of sol-gel derived 1D photonic crystals and Fabry Perot microcavities, as discussed in the subsequent section.

### 1.5 Sol-Gel Chemistry and Sol-Gel Thin Film Deposition

Sol-gel chemistry encompasses all wet-chemical processes in which a sol (a colloidal suspension of solid particles) transforms into a gel-like network. The underlying chemical processes for many sol-gel reactions are based on hydrolysis of the precursor species and their condensation to form a polymeric gel-like network.<sup>88</sup> Popular precursors for sol-gel chemistry-based processes are based on compounds that readily react with water to form metal hydroxy species (M-OH, M being a metal atom) in the first step of the reaction pathway. Prime candidates of such precursor compounds are metal alkoxides (M-OR, R being an organic group; for example, methyl, ethyl, isopropyl etc.). These metal alkoxides readily react with water in a nucleophilic substitution reaction to form oxo and hydroxo bridges according to:

Hydrolysis



Alcoxolation



Oxolation



The rates and extents of these reactions depend strongly on the nature of the used metal alkoxides, the amount of water and on the pH of the precursor solution.<sup>88</sup> Ideally, all monomeric reactants are polymerized uniformly and controllably to form a M-O-M network; however in real systems the reactivity varies greatly and depends on the type of metal alkoxide precursor. For example, while most titanium alkoxide precursors react

very quickly (within seconds) at room temperature, the reaction of silicon alkoxide precursors take tens of minutes and requires acid or base catalysis, and, in some cases, gentle heating.

Importantly, it should be pointed out that precursor hydrolysis/condensation reactions are exothermic and can lead to extreme heating of the reaction mixture; in general, the higher the rate of the reaction, the more strongly exothermic it is! The hydrolysis and condensation steps of the reaction are then followed by an aging step of the sol-gel reaction mixture. During this process, the initially formed nanometer-sized colloidal entities further cross-link. The time of the aging process depends on the solution concentration, type of solvent, solution pH, temperature, and the desired processing method and can last from a few minutes to several days. Most sol-gel precursor solutions are then stable for at least a week to several weeks at room temperatures and their viscosity can be adjusted by diluting the stock solution.

The second step of the sol-gel process is the conversion of the precursor solution into a solid material of desired shape. Depending on the desired final morphology, many different processing methods have been developed. These methods include spin-,<sup>89</sup> dip-,<sup>90</sup> and spray-coating<sup>91</sup> to produce thin films and multilayer coatings,<sup>92</sup> soft lithography to create nano and micrometer-sized features and periodic structures,<sup>93</sup> drawing and spinning to convert the precursor solution into fibers and needles,<sup>94</sup> and casting to fabricate monoliths thick coatings.<sup>95</sup> The processing method of foremost importance for this dissertation is dip-coating for the fabrication of thin films.<sup>96,97</sup> While, at first glance, the thin-film dip-coating deposition process from a sol-gel precursor solution consists of a simple substrate dipping step followed by a withdrawing step, detailed studies of the



dip-coating process unravel complicated competitions of up to six forces.<sup>98,99</sup> Due to the importance of these competing processes for successful fabrication of high-quality thin films and multilayer structures, a brief discussion is presented in the following.

The main sources of competing forces and stresses within developing thin films during the dip-coating process are associated with the viscosity and the surface tension of the reservoir as well as the dragging gravitational forces during the withdrawing step.<sup>98,100</sup> Furthermore, densification processes within the liquid and gel-like network immediately after the withdrawal of the substrate out of the precursor solution add shrinkage-related stresses onto the deposited thin film.<sup>101</sup> The stages of the densification process vary within the withdrawal step as presented in Figure 1.3. During the aggregation stage dilute sol-gel polymeric species are densified within the thin-film layer due to solvent evaporation. Upon further densification the initially liquid layer transforms into a gel-like film in which local polymeric aggregates crosslink through condensation reactions. This condensing network is finally sufficiently stiff to withstand gravitational drain and stabilizes the thin-film morphology. A drying stage during which most of the remaining solvent leaves the cross-linked network concludes the densification process, resulting in a solid thin film.

Since stresses related to all these processing steps can significantly diminish the quality of thin films, counteracting stress formation is crucial in producing high-quality crack-free thin films. In general, whenever thin-film stresses exceed the thin-film strength, formation of cracks within the cross-linked network occurs.<sup>90,101-104</sup> In Chapter 4 of this dissertation, strategies to minimize stress formation (or counteract stress built-up) in forming thin films will be discussed. Furthermore, it will also be shown how

knowledge of the factors leading to stress formation can be used to optimize the thin-film deposition and processing step. The result is a process that produces sol-gel thin films and multi-layer structures of highest quality, rivaling those of much more expensive and complicated chemical and physical deposition techniques.

### 1.6 Dissertation Overview

The dissertation is divided in two parts. The first part, Chapters 2 and 3, focuses on single fluorophore trajectory-analysis theory and is utilized in single-molecule tracking studies using TIRF microscopy. The second part of this dissertation deals with the simple and rapid fabrication of sol-gel derived thin films and multilayer stacks on planar and curved substrates (Chapter 4), and magnetic functionalization studies of the sol-gel derived thin films and magneto-optical effect measurements on these films (Chapter 5). Brief overviews of the individual chapters follow.

A novel statistical method to discern subdiffraction molecular motion from stationary molecules is introduced in Chapter 2. The method is based on the analysis of apparent motions of simulated and imaged stationary single DiI molecules at varied signal-to-noise ratios (S/N). Fisher's F-test statistics are then used in establishing confidence boundaries for reliably detecting subdiffraction molecular motion. The same statistical criteria are then utilized in the investigation of the motion of DiI molecules in planar, supported 1,2-Dimyristoyl-sn-glycero-3-phosphocholine (DMPC) bilayers at different temperatures. Furthermore, advantages of computing S/Ns in evaluating the localization precision for each point of a single molecule trajectory and in detecting diffusional heterogeneities in automated tracking software are demonstrated.

In Chapter 3 the same analysis method is used to detect confined molecular motion from strong adsorption events of Rhodamine 6G molecules in temperature-responsive poly(N-isopropylacrylamide). In this work, which was carried out in collaboration with the Paul Bohn-research group at the University of Notre Dame, confined diffusion studies of Rhodamine 6G molecules were carried out to probe the temperature-dependent changes in volume confinement within poly(N-isopropylacrylamide) brushes using single molecule TIRF microscopy.

In Chapter 4, an inexpensive, simple and fast sol-gel fabrication method for the synthesis of high-quality, crack-free thin films and multilayer structures on planar and curved substrates is introduced. The study identifies crack-formation mechanisms and discusses strategies to circumvent them during the thin-film deposition process. A novel shock-cooling step is introduced into the deposition cycle. This step has proven crucial in depositing high-quality alternating silica/titania thin-film stacks while minimizing crack formation. These photonic bandgap structures possess excellent structural and optical properties with tunable bandgaps, sharp band edges, and narrow optical transmission modes.

Magnetic functionalization studies of sol-gel derived thin films using the recently discovered dilute magnetic semiconductor effect are described in Chapter 5. Magnetic studies on Co-ion doped titania thin films are presented and an attempt to measure their magneto-optical properties using a home-built Faraday rotation setup is discussed. Furthermore, alternative magnetic functionalization strategies for these sol-gel derived thin films are presented in this chapter.

### 1.7 References

- (1) O'Regan, B.; Gratzel, M. *Nature* **1991**, *353*, 737.
- (2) Michael, G. *Journal of Photochemistry and Photobiology A: Chemistry* **2004**, *164*, 3.
- (3) Grätzel, M. *Inorganic Chemistry* **2005**, *44*, 6841.
- (4) Yoo, J.-W.; Irvine, D. J.; Discher, D. E.; Mitragotri, S. *Nat Rev Drug Discov* **2011**, *10*, 521.
- (5) Samad, A.; Sultana, Y.; Aqil, M. *Curr. Drug Delivery* **2007**, *4*, 297.
- (6) Wang, G. *Drug Delivery, Principles and Applications*; John Wiley: Hoboken, 2005.
- (7) Deniz, A. A.; Mukhopadhyay, S.; Lemke, E. A. *Journal of The Royal Society Interface* **2008**, *5*, 15.
- (8) Lee, Y. J.; Park, S.-J.; Gesquiere, A. J.; Barbara, P. F. *Appl. Phys. Lett.* **2005**, *87*, 051906.
- (9) Fox, C. B.; Wayment, J. R.; Myers, G. A.; Endicott, S. K.; Harris, J. M. *Anal. Chem.* **2009**, *81*, 5130.
- (10) McCain, K. S.; Hanley, D. C.; Harris, J. M. *Anal. Chem.* **2003**, *75*, 4351.
- (11) Elliott, L. C. C.; Barhoum, M.; Harris, J. M.; Bohn, P. W. *Phys. Chem. Chem. Phys.* **2011**, *13*, 4326.
- (12) Jung, C.; Schwaderer, P.; Dethlefsen, M.; Kohn, R.; Michaelis, J.; Brauchle, C. *Nat Nano* **2011**, *6*, 87.
- (13) Kirstein, J.; Platschek, B.; Jung, C.; Brown, R.; Bein, T.; Brauchle, C. *Nat Mater* **2007**, *6*, 303.
- (14) Michaelis, J.; Brauchle, C. *Chem. Soc. Rev.* **2010**, *39*, 4731.
- (15) Klausner, R. D.; Wolf, D. E. *Biochemistry* **1980**, *19*, 6199.
- (16) Maier, O.; Oberle, V.; Hoekstra, D. *Chem. Phys. Lipids* **2002**, *116*, 3.
- (17) Nakashima, N.; Kunitake, T. *J. Am. Chem. Soc.* **1982**, *104*, 4261.
- (18) Wayment, J. R.; Harris, J. M. *Anal. Chem.* **2008**, *81*, 336.

- (19) Broder, G. R.; Ranasinghe, R. T.; Neylon, C.; Morgan, H.; Roach, P. L. *Anal. Chem.* **2011**, *83*, 2005.
- (20) Sako, Y.; Minoghchi, S.; Yanagida, T. *Nat. Cell Biol.* **2000**, *2*, 168.
- (21) Yildiz, A.; Forkey, J. N.; McKinney, S. A.; Ha, T.; Goldman, Y. E.; Selvin, P. R. *Science* **2003**, *300*, 2061.
- (22) Yildiz, A.; Tomishige, M.; Vale, R. D.; Selvin, P. R. *Science* **2004**, *303*, 676.
- (23) Gelles, J.; Schnapp, B. J.; Sheetz, M. P. *Nature* **1988**, *331*, 450.
- (24) Veigel, C.; Schmidt, C. F. *Nat Rev Mol Cell Biol* **2011**, *12*, 163.
- (25) Saxton, M. J.; Jacobson, K. *Annu. Rev. Biophys. Biomol. Struct.* **1997**, *26*, 373.
- (26) Kusumi, A.; Sako, Y.; Yamamoto, M. *Biophys. J.* **1993**, *65*, 2021.
- (27) Eggeling, C.; Ringemann, C.; Medda, R.; Schwarzmann, G.; Sandhoff, K.; Polyakova, S.; Belov, V. N.; Hein, B.; von Middendorff, C.; Schonle, A.; Hell, S. W. *Nature* **2009**, *457*, 1159.
- (28) Schmidt, T.; Schütz, G. J.; Baumgartner, W.; Gruber, H. J.; Schindler, H. *Proceedings of the National Academy of Sciences* **1996**, *93*, 2926.
- (29) Ide, T.; Yanagida, T. *Biochem. Biophys. Res. Commun.* **1999**, *265*, 595.
- (30) Cicuta, P.; Keller, S. L.; Veatch, S. L. *The Journal of Physical Chemistry B* **2007**, *111*, 3328.
- (31) Huang, B.; Wang, W.; Bates, M.; Zhuang, X. *Science* **2008**, *319*, 810.
- (32) Gustafsson, M. G. L. *Journal of Microscopy* **2000**, *198*, 82.
- (33) Klar, T. A.; Hell, S. W. *Opt. Lett.* **1999**, *24*, 954.
- (34) Huang, B.; Bates, M.; Zhuang, X. *Annu. Rev. Biochem.* **2009**, *78*, 993.
- (35) Wazawa, T.; Ueda, M.; Rietdorf, J., Ed.; Springer Berlin / Heidelberg: 2005; Vol. 95, p 1297.
- (36) Mattheyses, A. L.; Simon, S. M.; Rappoport, J. Z. *J. Cell Sci.* **2010**, *123*, 3621.
- (37) Axelrod, D. *Traffic* **2001**, *2*, 764.

- (38) Daniel, A. In *Methods in Cell Biology*; Taylor, D. L., Yu-Li, W., Eds.; Academic Press: 1989; Vol. Volume 30, p 245.
- (39) Hirschfeld, T. E. *Can. J. Spectrosc.* **1965**, *10*, 128.
- (40) Garland, P. B. *Q. Rev. Biophys.* **1996**, *29*, 91.
- (41) Axelrod, D.; Burghardt, T. P.; Thompson, N. L. *Annual Review of Biophysics and Bioengineering* **1984**, *13*, 247.
- (42) Taitt, C. R.; Anderson, G. P.; Ligler, F. S. *Biosensors and Bioelectronics* **2005**, *20*, 2470.
- (43) Wayment, J. R.; Harris, J. M. *Anal. Chem.* **2006**, *78*, 7841.
- (44) Douglass, A. D.; Vale, R. D. *Cell* **2005**, *121*, 937.
- (45) Elliott, L. C. C.; Barhoum, M.; Harris, J. M.; Bohn, P. W. *Langmuir* **2011**, *27*, 11037.
- (46) Heider, E. C.; Barhoum, M.; Peterson, E. M.; Schaefer, J.; Harris, J. M. *Appl. Spectrosc.* **2010**, *64*, 37.
- (47) Axelrod, D. *The Journal of Cell Biology* **1981**, *89*, 141.
- (48) Heider, E. C.; Barhoum, M.; Edwards, K.; Gericke, K.-H.; Harris, J. M. *Anal. Chem.* **2011**, *83*, 4909.
- (49) Yablonovitch, E. *Phys. Rev. Lett.* **1987**, *58*, 2059.
- (50) John, S. *Phys. Rev. Lett.* **1987**, *58*, 2486.
- (51) Joannopoulos, J. D.; Villeneuve, P. R.; Fan, S. *Solid State Commun.* **1997**, *102*, 165.
- (52) Ho, K. M.; Chan, C. T.; Soukoulis, C. M. *Phys. Rev. Lett.* **1990**, *65*, 3152.
- (53) Joannopoulos, J. D.; Johnson, S. G.; Winn, J. N.; Meade, R. D. *Photonic Crystals: Molding the Flow of Light (Second Edition)*; Princeton University Press, 2008.
- (54) Woldeyohannes, M.; John, S. *Journal of Optics B: Quantum and Semiclassical Optics* **2003**, *5*, R43.
- (55) Joannopoulos, J. D.; Villeneuve, P. R.; Fan, S. *Nature* **1997**, *386*, 143.

- (56) Shir, D.; Nelson, E. C.; Chen, Y. C.; Brzezinski, A.; Liao, H.; Braun, P. V.; Wiltzius, P.; Bogart, K. H. A.; Rogers, J. A. *Appl. Phys. Lett.* **2009**, *94*, 011101.
- (57) Subramania, G.; Li, Q.; Lee, Y.-J.; Figiel, J. J.; Wang, G. T.; Fischer, A. J. *Nano Lett.* **2011**, *11*, 4591.
- (58) Campbell, M.; Sharp, D. N.; Harrison, M. T.; Denning, R. G.; Turberfield, A. J. *Nature* **2000**, *404*, 53.
- (59) Feiertag, G.; Ehrfeld, W.; Freimuth, H.; Kolle, H.; Lehr, H.; Schmidt, M.; Sigalas, M. M.; Soukoulis, C. M.; Kiriakidis, G.; Pedersen, T.; Kuhl, J.; Koenig, W. *Appl. Phys. Lett.* **1997**, *71*, 1441.
- (60) Shoji, S.; Kawata, S. *Appl. Phys. Lett.* **2000**, *76*, 2668.
- (61) Xia, Y.; Gates, B.; Li, Z. Y. *Adv. Mater. (Weinheim, Ger.)* **2001**, *13*, 409.
- (62) Norris, D. J.; Arlinghaus, E. G.; Meng, L.; Heiny, R.; Scriven, L. E. *Adv. Mater. (Weinheim, Ger.)* **2004**, *16*, 1393.
- (63) Ozin, G. A.; Yang, S. M. *Adv. Funct. Mater.* **2001**, *11*, 95.
- (64) Hynninen, A.-P.; Thijssen, J. H. J.; Vermolen, E. C. M.; Dijkstra, M.; van Blaaderen, A. *Nat. Mater.* **2007**, *6*, 202.
- (65) Norris, D. J.; Vlasov, Y. A. *Adv. Mater. (Weinheim, Ger.)* **2001**, *13*, 371.
- (66) Whitesides, G. M.; Boncheva, M. *Proceedings of the National Academy of Sciences* **2002**, *99*, 4769.
- (67) Im, S. H.; Lim, Y. T.; Suh, D. J.; Park, O. O. *Adv. Mater. (Weinheim, Ger.)* **2002**, *14*, 1367.
- (68) Galusha, J. W.; Tsung, C.-K.; Stucky, G. D.; Bartl, M. H. *Chem. Mater.* **2008**, *20*, 4925.
- (69) Jenekhe, S. A.; Chen, X. L. *Science* **1999**, *283*, 372.
- (70) Holland, B. T.; Blanford, C. F.; Stein, A. *Science* **1998**, *281*, 538.
- (71) Wijnhoven, J. E. G. J.; Vos, W. L. *Science* **1998**, *281*, 802.
- (72) Davis, S. A.; Burkett, S. L.; Mendelson, N. H.; Mann, S. *Nature* **1997**, *385*, 420.
- (73) Yang, P.; Deng, T.; Zhao, D.; Feng, P.; Pine, D.; Chmelka, B. F.; Whitesides, G. M.; Stucky, G. D. *Science* **1998**, *282*, 2244.

- (74) McKenna, B. J.; Birkedal, H.; Bartl, M. H.; Deming, T. J.; Stucky, G. D. *Angewandte Chemie International Edition* **2004**, *43*, 5652.
- (75) Bartl, M. H.; Puls, S. P.; Tang, J.; Lichtenegger, H. C.; Stucky, G. D. *Angewandte Chemie International Edition* **2004**, *43*, 3037.
- (76) Yang, P.; Zhao, D.; Margolese, D. I.; Chmelka, B. F.; Stucky, G. D. *Chem. Mater.* **1999**, *11*, 2813.
- (77) Zhao, D.; Feng, J.; Huo, Q.; Melosh, N.; Fredrickson, G. H.; Chmelka, B. F.; Stucky, G. D. *Science* **1998**, *279*, 548.
- (78) Mann, S.; Burkett, S. L.; Davis, S. A.; Fowler, C. E.; Mendelson, N. H.; Sims, S. D.; Walsh, D.; Whilton, N. T. *Chem. Mater.* **1997**, *9*, 2300.
- (79) Wen, J.; Wilkes, G. L. *Chem. Mater.* **1996**, *8*, 1667.
- (80) Wright, J. D.; Sommerdijk, N. A. J. M. *Sol-Gel Materials: Chemistry and Applications*; CRC Press, 2000.
- (81) Lu, Y.; Ganguli, R.; Drewien, C. A.; Anderson, M. T.; Brinker, C. J.; Gong, W.; Guo, Y.; Soyez, H.; Dunn, B.; Huang, M. H.; Zink, J. I. *Nature* **1997**, *389*, 364.
- (82) Brinker, C. J.; Lu, Y.; Sellinger, A.; Fan, H. *Adv. Mater. (Weinheim, Ger.)* **1999**, *11*, 579.
- (83) Yang, P.; Zhao, D.; Margolese, D. I.; Chmelka, B. F.; Stucky, G. D. *Nature* **1998**, *396*, 152.
- (84) Stein, A.; Melde, B. J.; Schroden, R. C. *Adv. Mater. (Weinheim, Ger.)* **2000**, *12*, 1403.
- (85) Schubert, U.; Huesing, N.; Lorenz, A. *Chemistry of Materials* **1995**, *7*, 2010.
- (86) Chujo, Y. *Current Opinion in Solid State and Materials Science* **1996**, *1*, 806.
- (87) Corriu, R. J. P.; Leclercq, D. *Angewandte Chemie International Edition in English* **1996**, *35*, 1420.
- (88) Brinker, C. J.; Scherer, G. W. *Sol-gel science*, 1990.
- (89) Natsume, Y.; Sakata, H. *Thin Solid Films* **2000**, *372*, 30.
- (90) Barhoum, M.; Morrill, J. M.; Riassetto, D.; Bartl, M. H. *Chem. Mater.* **2011**.



- (91) Hofacker, S.; Mechtel, M.; Mager, M.; Kraus, H. *Progress in Organic Coatings* **2002**, *45*, 159.
- (92) Brinker, C. J.; Hurd, A. J.; Schunk, P. R.; Frye, G. C.; Ashley, C. S. *Journal of Non-Crystalline Solids* **1992**, *147-148*, 424.
- (93) Pang, M. L.; Lin, J.; Cheng, Z. Y.; Fu, J.; Xing, R. B.; Wang, S. B. *Materials Science and Engineering: B* **2003**, *100*, 124.
- (94) Caruso, R. A.; Schattka, J. H.; Greiner, A. *Advanced Materials* **2001**, *13*, 1577.
- (95) Yoshida, K.; Kamada, K.; Sato, K.; Hatada, R.; Baba, K.; Atsuta, M. *Journal of Biomedical Materials Research* **1999**, *48*, 778.
- (96) Rabaste, S.; Bellessa, J.; Brioude, A.; Bovier, C.; Plenet, J. C.; Brenier, R.; Marty, O.; Mugnier, J.; Dumas, J. *Thin Solid Films* **2002**, *416*, 242.
- (97) Almeida, R. M.; Rodrigues, A. S. *Journal of Non-Crystalline Solids* **2003**, *326-327*, 405.
- (98) Livage, J.; Henry, M.; Sanchez, C. *Prog. Solid State Chem.* **1988**, *18*, 259.
- (99) Scriven, L. E. In *Better Ceramics Through Chemistry III*; Brinker, C. J., Clark, D. E., Ulrich, D. R., Eds.; Mat.Res.Soc.: Pittsburgh, Pa, 1988, p 717.
- (100) Faustini, M.; Louis, B.; Albouy, P. A.; Kuemmel, M.; Grosso, D. *The Journal of Physical Chemistry C* **2010**, *114*, 7637.
- (101) Bockmeyer, M.; Löbmann, P. *Chemistry of Materials* **2006**, *18*, 4478.
- (102) Bockmeyer, M.; Löbmann, P. *Thin Solid Films* **2007**, *515*, 5212.
- (103) Brenier, R.; Gagnaire, A. *Thin Solid Films* **2001**, *392*, 142.
- (104) Kozuka, H.; Takenaka, S.; Tokita, H.; Hirano, T.; Higashi, Y.; Hamatani, T. *Journal of Sol-Gel Science and Technology* **2003**, *26*, 681.

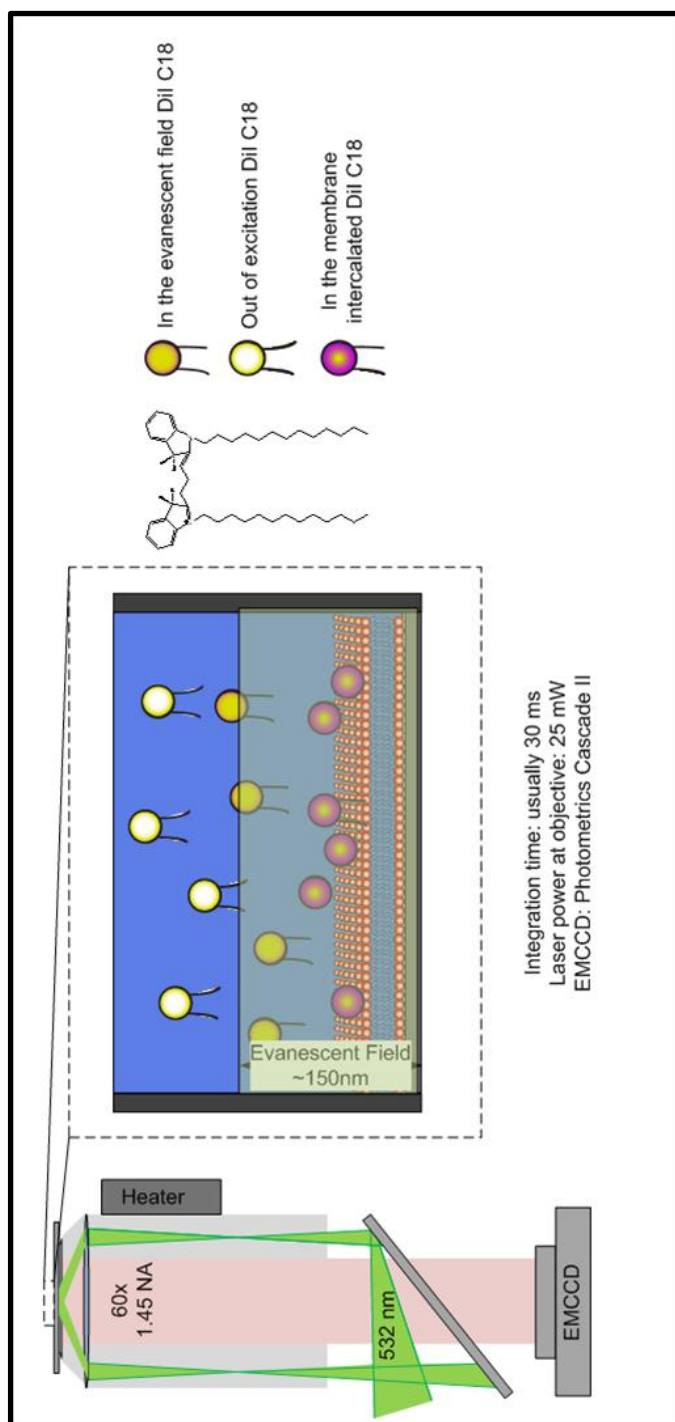


**Figure 1.1:** Schematic of a TIRF microscope. The evanescent wave penetration depth

for the used setup is around 150 nm. Single DiI molecules are excited within the

evanescent wave and show additional quantum yield increase when intercalated into the lipid bilayer.

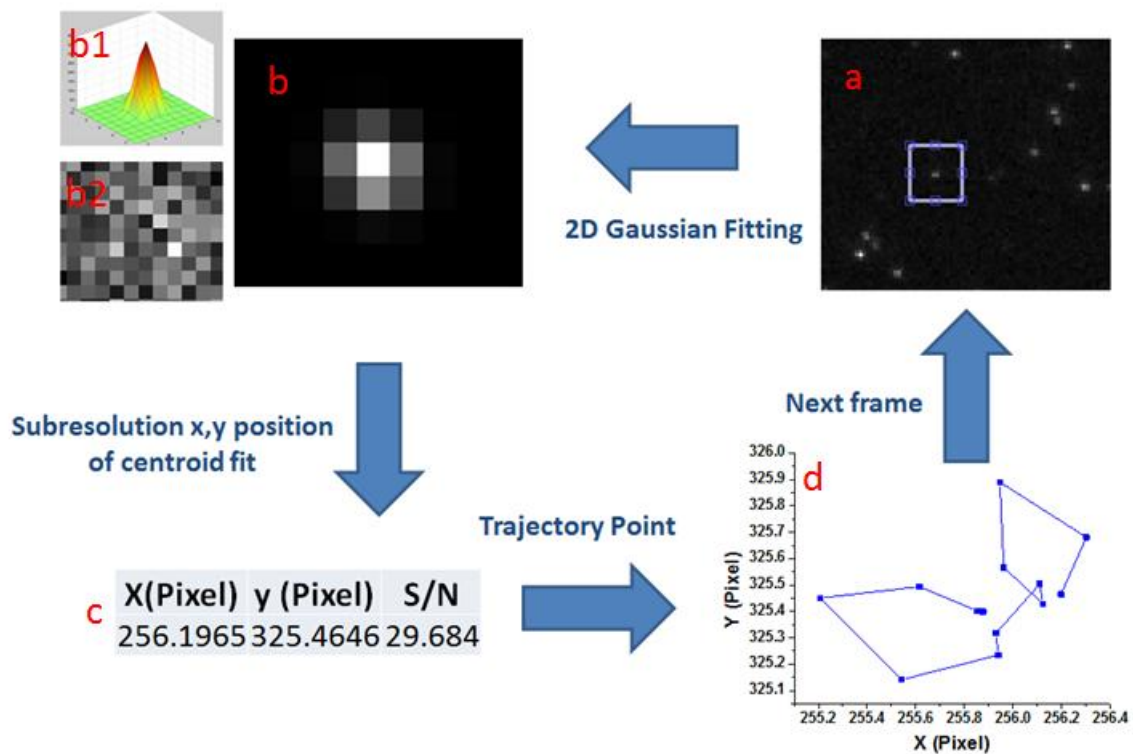


**Figure 1.2:** Single molecule tracking cycle: A single molecule within a region of interest (ROI) (a) is fitted to a 2D Gaussian function (b) (b1 and b2 represent the 3D plot of the Gaussian fit and the background of the fit). The centroid of the fit represents the subdiffraction position of the single molecule(c). The position is then recorded as a trajectory point (d).

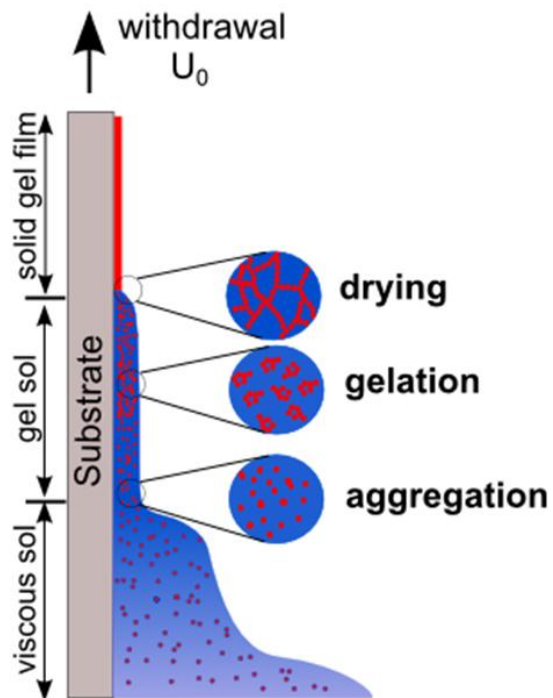
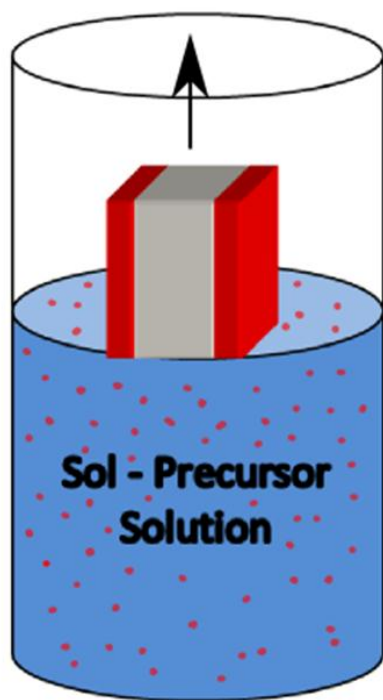


**Figure 1.3:** A schematic of the sol-gel dip-coating process highlighting the different stages in the formation of a solid gel network

## CHAPTER 2

# STATISTICAL CRITERIA FOR DETECTING MOLECULAR MOTION IN SINGLE MOLECULE DIFFUSIONAL TRAJECTORIES

### 2.1 Introduction

Localizing single fluorophores with subdiffraction resolution has been an important advance in visualizing biological structures,<sup>1-3</sup> exploring nanostructured channel systems<sup>4-6</sup> and investigating biomolecular motions.<sup>7-9</sup> The fundamental principle of achieving nanometer localization precision of diffraction limited single fluorophores spots in an image lies in reliably fitting their intensity profiles to a Gaussian point spread function (PSF).<sup>10,11</sup> Given a sufficiently high S/N ratio, the centroids of these two-dimensional Gaussian fits represent the subdiffraction coordinates of the position of the fluorophores.<sup>11-15</sup> The position uncertainty of localized fluorophores depends on the experimental S/N ratio, defined in this work as the ratio of peak intensity amplitude to standard-deviation of the calculated background of fitted individual fluorophore spot.<sup>16</sup>

The detection of molecular motion (the step size between two image frames) in a diffusional trajectory of a fluorophore involves knowledge about the position and its uncertainty at two different locations. The spatial resolution limit for discerning two

locations from one another depends on the local S/N, and the pixelation noise for both positions of the fluorophore representing a molecular step. Therefore, statistical criteria needed for determining the location of a molecule differ from those necessary for reliably detecting molecular motions, as demonstrated and discussed in the subsequent sections.

There is an active field of research in resolving the magnitude of discrete steps of molecular motors along linear proteins or nucleic acids with nanometer-scale precision.<sup>8,17-20</sup> The translocation mechanism of enzymes are investigated by reliably determining the discrete molecular step-sizes enzymes undergo in x-and y-direction. The challenge in resolving these discrete steps from Brownian noise is of fundamental importance in shedding light on the translocation mechanism of molecular motors. Therefore, statistical criteria for determining discrete step sizes of molecular motors in the frequency or in the time domain have been proposed and utilized, as reviewed by Neuman et al.<sup>21</sup>

The statistical criteria for discerning molecular motion from stationary molecules, whose motions are neither discrete nor directed in space, have not yet been established for single molecule tracking experiments. The ability to resolve molecular motion with high precision combined with the knowledge about the spatial resolution limit for detecting molecular motion would be a valuable asset in the interpretation of single molecule diffusional processes. Furthermore, evaluating the local S/N while tracking single molecules allows one to determine the local spatial resolution limits at each point of a trajectory. This stands in contrast to the more common practice in which a global or average S/N is utilized to estimate the spatial resolution limit of an entire single molecule tracking experiment.

The goal of this study is to establish statistical criteria for discerning actual subdiffraction molecular motion from the apparent motion of stationary single molecules that arises from the limited S/N of fluorescence images. We approach this goal by first modeling the apparent motion of stationary molecules and its dependence on S/N. Statistical criteria are then established to reliably detect subdiffraction molecular motion in tracking experiments. The simulated results are then tested against experimental data from images of DiI molecules adsorbed to glass. The same statistical criteria are then utilized in the investigation of the motion of DiI molecules in planar, supported 1,2-dimyristoyl-sn-glycero-3-phosphocholine (DMPC) bilayers at different temperatures.

## 2.2 Materials and Methods

### 2.2.1 Materials

1,2-Dimyristoyl-sn-glycero-3-phosphocholine (DMPC) was purchased in powder form from Avanti Polar Lipids (Alabaster, AL). The fluorescent probe DiI (DiIC18 (3)) was purchased from Invitrogen (Carlsbad, CA) and high purity chloroform was purchased from EMD Chemicals (Gibbstown, NJ).

### 2.2.2 Deposition of supported lipid bilayers onto glass

Supported lipid bilayers were deposited onto a glass coverslip using the Langmuir-Schaefer method as described in detail elsewhere.<sup>22,23</sup> Briefly, a cleaned glass coverslip was first immersed into the water subphase of a Langmuir-Schaefer trough (KSV Minitrough, KSV Instruments, LTD.). A 50 $\mu$ L volume of a DMPC solution (~1mg/mL DMPC in chloroform) was then drop-cast onto the water-air interface. The

chloroform was allowed to evaporate for ~10min after which two Teflon barriers compressed the lipid layer until a surface pressure of 32 mN/m was reached. The surface pressure, measured by a Wilhelmy plate, was kept constant during the entire deposition process. A lipid monolayer was deposited by vertically withdrawing (withdrawal rate of 5mm/min) the water-immersed glass coverslip through the water/lipid interphase. In a second step, the horizontally oriented glass coverslip was pushed (~40mm/min) through the water/lipid subphase, completing the bilayer deposition. The quality of the lipid bilayer was evaluated by the transfer ratio, which ranged between 0.8 and 1.2. Transfer ratios close to one indicate that the area of the lipid bilayer is equivalent to the substrate area.<sup>24</sup> The deposited bilayer was kept immersed and mounted into an aluminum well cell.

### 2.2.3 Fluorescence microscopy and data acquisition

The TIRF microscope system and the data acquisition parameters used in this study are described in detail elsewhere.<sup>25</sup> To summarize, a 25mW, 532nm circularly polarized laser beam is focused into the back focal plane of a TIRF objective. The laser beam was then laterally translated to the edge of the TIRF objective until total internal reflection at the glass-coverslip/ water interface was observed. The fluorescence emission of excited single fluorophores was then collected through the same objective and imaged onto the detector, a CascadeII 512 EMCCD camera (Photometrics). The camera was controlled using Metamorph Imaging software (Universal Imaging). Image stacks of 1000 frames were recorded with an integration time of 30ms per frame.



#### 2.2.4 Temperature control and mounting the deposited lipid bilayer into a well cell

The temperature in the well cell was regulated through a temperature-controlled microscope stage, described in detail elsewhere.<sup>26</sup> Slight modifications to this setup involved replacing the copper sample cell with an aluminum well cell. This allowed mounting the glass coverslip into the well cell without the use of epoxy. Additionally, a thermocouple was directly immersed into the water reservoir of the well cell to allow for an accurate temperature reading at the vicinity of the glass-coverslip. The aluminum well cell was placed onto a Peltier stage (Technical Video, Ltd.) surrounded by a copper block to allow for homogenous heat transfer to the sample cell. The temperature was controlled using a DC power supply and was varied in approximately 1°C/min steps.

Precaution regarding beam alignment and focus drift had to be taken into account when changing the temperature during TIRF experiments on lipid bilayers. Raising or lowering the temperature can cause the objective oil to expand or contract resulting in a focus drift and a decrease in image quality. Slight beam realignment and refocusing is therefore necessary to counteract these effects between changes in sample temperature.

#### 2.2.5 Apparent-motion plots

Setting up an apparent-motion plot involves first imaging stationary DiI molecules on glass using the same imaging settings as for the subsequent tracking experiments. DiI molecules were adsorbed to a glass coverslip via dip coating from a dilute solution (25pM) of DiI fluorophores in methanol. After solvent evaporation, images of immobile DiI molecules were acquired using the TIRF microscope system.<sup>27</sup>

Intensity profiles of individual DiI fluorophores were then identified and fitted to 2D Gaussian functions using in-house written Matlab (Mathworks) program as described in detail elsewhere.<sup>28</sup> The quantities of amplitude, width, and background determined from the fitted Gaussian functions were then used as parameters in simulating stationary single molecules at varying S/N. Simulated movies of 100 frames with 10 single molecules randomly positioned on a 256x256 grid were modeled using the same amplitude to background ratio representing one specific S/N. Varying the S/N ratio in the simulation was accomplished by varying the signal amplitude of the Gaussian functions while keeping the Poisson-distributed background noise at a constant variance.

An in-house written single molecule tracking program Matlab (Mathworks) was then used in tracking the apparent motion of simulated stationary molecules. This involved identifying single molecules on simulated images and fitting their intensity profiles to 2D Gaussian functions. The centroid position of the Gaussian fits determined the x,y-coordinates of the fitted molecules. A 15x15 pixel region of interest (ROI) window was then centered on the x,y-coordinates of the fitted molecule. If a molecule in the subsequent frame was identified within the newly positioned ROI, then the fitting procedure was repeated and the x,y-position of the fluorophores along its trajectory was determined. This cycle was repeated until there were no more single molecules found within the specified ROI. The recovered x,y positions of the individual fitted spots were then used in calculating a mean-square displacement of the apparent steps as a function of S/N.

### 2.2.6 Calculating a local S/N during single molecule tracking experiments

For evaluating molecular motion in single molecule movies, the local S/N for each step in a single molecule trajectory was determined by computing the ratio of the fitted intensity amplitude to the standard deviation of the locally fitted background. It is worth noting that computing a local S/N does not require additional extensive computational resources since both quantities are readily available as parameters from the 2D Gaussian fits.

## 2.3 Results and Discussion

### 2.3.1 Characterizing the apparent motion of stationary single molecules

Traditionally, the spatial resolution limit of single molecule tracking experiments is specified as the standard deviation of the difference in position centroid determined by imaging stationary fluorophores.<sup>8,12,25</sup> Using this parameter as a boundary for detecting subdiffraction molecular motions in single molecule trajectories has several limitations. As demonstrated by Monte Carlo simulation presented in Figure 2.1, neither the standard deviation  $(V(x))^{1/2}$  of the centroid-position difference  $(x_{r+1}-x_r)$  in x or y (red line)<sup>17</sup>

$$\frac{1}{n-1} \sum_{r=1}^n (x_{r+1} - x_r) = \langle V(x) \rangle^{1/2} \quad [2.1]$$

nor the standard deviation of the apparent radial step sizes  $V(r)^{1/2}$  (green line)

$$\langle V(r) \rangle^{1/2} = \sqrt{\langle V(x) + V(y) \rangle} \quad [2.2]$$

of imaged stationary fluorophores for a given S/N represent a valid upper boundary for the apparent step sizes obtained from the same data set. Rather these parameters capture the average behavior of the apparent step sizes for a given S/N. The ability to detect actual subdiffraction molecular motion of a fluorophore requires a statistical comparison of the apparent step size for two measured positions versus the expected range of radial motion of stationary molecules.

A second issue involved in the detection of subdiffraction molecular motion is that the location uncertainty in single molecules depends on the S/N ratio of the fluorophore at its measured position. Determining a global, average S/N does not account for variations in the spatial resolution limit arising from variation in the local S/Ns during the single molecule experiment. Sources for S/N variations include excitation power-fluctuations and inhomogeneous field illumination in a fluorescence image. Single molecule photo-physical phenomena including blinking, photo-bleaching or a change in quantum-yield with local environment are intrinsic sources of S/N variations. Additionally diffusional heterogeneities, where faster diffusion events spread out the intensity distribution of a molecule, are generally associated with a change in the local S/N. Hence determining a global or average S/N does not adequately describe the localization precision or the detection sensitivity for molecular motion of single molecule experiments subject to S/N variations, as exemplified by the imaged stationary DiI molecules in Figure 2.2. Computing a local S/N ratio allows for evaluating the

localization precision for each point of a single molecule trajectory, thus improving the reliability of detecting subdiffraction molecular motion of a fluorophore.

### 2.3.2 Statistical criteria for distinguishing molecular motion

#### from stationary molecules

The ability to reliably discern actual subdiffraction molecular motion from the apparent motion of stationary molecules first requires analysis of the apparent mean square displacement from a population of stationary molecules and a determination of the dependence of the mean square displacement on the S/N ratio. The mean square displacement in a random walk model equals the variance of a Gaussian probability function.<sup>29</sup> If the apparent motion of stationary molecules fits a radial Gaussian probability function, then a Fisher's F-test can be used to compare two samples of the variance without prior knowledge of their means.<sup>30</sup> To test whether the measured apparent mean square displacement of stationary molecules is drawn from a radial Gaussian distribution, histograms of the frequency of apparent step sizes of simulated and imaged stationary DiI molecules were compared to a radial Gaussian distribution,  $P(r)$ , of a random walk model,<sup>31-33</sup> where the variance,  $V(r)$  is the mean square displacement,  $\langle r^2 \rangle$ .<sup>34</sup>

$$P(r) = 2\pi r * \left[ \frac{1}{\pi \langle r^2 \rangle} \right] e^{-\frac{r^2}{\langle r^2 \rangle}} \quad [2.3]$$

Histogram plots of the apparent step sizes from simulated and imaged stationary DiI molecules indeed follow a Gaussian distribution, as shown by the goodness of the fit to the model; see Figure 2.3.

Discerning molecular motion from stationary molecules using F-test statistics involves the computation of F-values according to the equation:

$$F = \frac{r^2_{\text{test point}}}{\langle r^2 \rangle_{\text{apparent}}} \quad [2.4]$$

where  $r^2$  of a tested point in the trajectory is a sample of the variance with one-degree of freedom, and  $\langle r^2 \rangle_{\text{apparent}}$  is the variance of apparent steps of stationary molecules at an equivalent S/N ratio. If the computed F-value lies within a critical value then the variances are indistinguishable within a confidence boundary,  $\alpha$ , which represents the probability of a single sample of  $r^2$  exceeding the critical value. Measuring a value of  $r^2$  that exceeds the critical value boundary implies the detection of molecular motion with a confidence of  $(1 - \alpha)$ . This concept is demonstrated for simulated stationary DiI molecules at varying S/N ratios in Figure 2.4A. The figure consists of the apparent root-mean square displacement of simulated stationary DiI molecules (black line) and a 99% confidence boundary,  $(1 - \alpha) = 0.99$ , for detecting molecular motion (red line) for varying S/N. For example, if at a local S/N of 20 a step size below 0.2 pixels were measured, then the null hypothesis is not refuted, and molecular motion cannot be detected with confidence. If, on the other hand, a step size greater than 0.2 pixels is measured for a local S/N of 20, then molecular motion is detected with 99% confidence. The magnitude of a significant step depends on the local S/N ratio and decreases with increasing local

S/N values. At higher S/N, the localization accuracy increases, resulting in a greater sensitivity for the detection of subdiffraction molecular motion. The predictions from simulations are compared with experimental measurements of apparent motion of DiI molecules adsorbed to glass as shown in Figure 2.4B. All the apparent motions consistently lie within the upper boundary for not detecting molecular steps for a given local S/N ratio range of 6 to nearly 20.

### 2.3.3 Investigating DiI diffusional trajectories on supported DMPC bilayers

A molecule trajectory of DiI diffusing on a DMPC bilayer at room temperature demonstrates the ability to distinguish molecular motion from stationary molecules, as shown in Figure 2.5. The results of the analysis are plotted in a x,y-trajectory where the radii of circles around the points represent the local boundary for detecting molecular motion with 99% confidence. The sizes of the radii vary through the trajectory according to the local S/N, which is represented in the color-coding of the circles. A measured step size exceeding the circle implies the detection of molecular motion (blue segments in the trajectory) with 99% confidence; otherwise the apparent motion of the fluorophore does not exceed a statistically significant magnitude (green segments). A higher S/N ratio produces a smaller critical radius resulting in a greater sensitivity for detecting molecular motion. The corresponding apparent motion plot in Figure 2.5B reveals a diffusive DiI molecule with few short sticking events. Another interesting finding is that stationary events within the trajectory correlate with a high local S/N (see positions which are color-

coded with blue circles in Figure 2.5A). The implications of this result in the interpretation of the DiI trajectory are discussed below.

Representative DiI trajectories on a DMPC bilayer were acquired at three different temperatures, which are below ( $8^{\circ}\text{C}$ ), above ( $37^{\circ}$ ) and at ( $\sim 24^{\circ}$ ) the gel-to-fluid phase transition temperature ( $T_M$ ) of the DMPC bilayer; see Figure 2.6. Increasing the temperature results in greater mobility of the DiI molecules, which is apparent by the smaller fraction of stationary events (green squares) compared to detected molecular motions (blue squares). This trend correlates with formation of the fluid phase of DMPC at its  $T_M$  as revealed in temperature dependent atomic force microscopy (AFM) studies of DMPC lipid bilayers<sup>35</sup> and lateral diffusion studies of DiI molecules in DMPC bilayers measured by FRAP (fluorescence recovery after photobleaching),<sup>24,36,37</sup> which found comparable diffusion coefficients as the present results.

The DiI trajectory acquired at the temperature below the  $T_M$  of the DMPC bilayer ( $8^{\circ}\text{C}$ ) shows no significant mobility (the recovered position differences are mostly (95%) below the 99% confidence boundary). Furthermore, the computed local S/Ns are significantly shifted to higher values compared to those of imaged stationary DiI molecules on glass (Figure 2.4) or moving DiI molecules in the higher temperature trajectories. A significant increase in the quantum yield of cyanine dyes has been observed when they bind to bilayer membranes, as reported by Nakashima et al.<sup>38</sup> The study concluded that the increased quantum yield of cyanine dyes in lipid bilayers is due to the more rigid, hydrophobic environment of the membrane. A molecular dynamics study of DiI molecules in gel phase 1,2-dipalmitoyl-sn-glycero-3-phosphocholine (DPPC) bilayer at room temperature concludes that the DiI headgroup is located in close



proximity to the lipid head group with its positive head group stabilizing the orientation of the DiI molecule resulting in its quantum yield increase.<sup>39,40</sup> A similar explanation was given in interpreting the lateral diffusion coefficient of DiI on DMPC bilayer below its  $T_M$  from FRAP experiments.<sup>36</sup>

The diffusive behavior of the DiI probe on DMPC bilayer at room temperature consists of sections with limited mobility including short (less than 60ms) sticking events interrupted by high mobility apparent in the larger step sizes represented in the scatter plot. Furthermore, the distribution of local S/N shifts towards lower values compared to the low temperature results. The diffusive behavior of the DiI probe reflects a phase mixture within the DMPC bilayer at its  $T_M$ , with coexisting fluid and gel phases as confirmed by AFM studies.<sup>35</sup> The AFM study concludes that the fluid phase portion of the DMPC bilayer increases with increasing temperature until the gel-phase portion vanishes; as is reflected in the diffusive behavior of DiI at 37°C. Above the phase transition temperature, DiI exhibits free diffusional behavior with minor sticking events which are accompanied with low local S/N. We attribute these short lived sticking events to a surface absorption/desorption mechanism observed and described in supported lipid bilayers by Dertinger et al.<sup>41</sup> A scatter plot further indicates the occurrence of high local S/N accompanied in conjunction with hopping events (> 1pixel) and resolvable short step events. To elucidate the underlying diffusional process a detailed analysis of the trajectory in a magnified region is given in Figure 2.7. The analysis shows no stationary events (except for short lived confinement). It further reveals a pattern of confined diffusion accompanied with a drastic increase in local S/N ratios and hops accompanied with lower local S/Ns. Original snap shots of the molecule representing the S/N variation

at the different stages of this pattern are presented in the figure. This diffusion pattern suggests the existence of nanometer size gel phase domains within the fluid phase even at 37°C. It is worth noting that molecular motions with step sizes of 22 nm were reliably resolved due to the increased local S/Ns.

Caution needs to be exercised in determining and interpreting a diffusion coefficient if the recorded trajectory exhibits low S/Ns as demonstrated for the DiI trajectory acquired below the  $T_M$  of DMPC. Although all steps were classified as stationary in this trajectory, the apparent means square displacement,  $\langle r^2 \rangle$ , corresponds to an apparent diffusion coefficient  $D_{app} = 1.25 \times 10^{-9} \text{ cm}^2/\text{sec}$ . If in another example a trajectory with step sizes  $r=0.6$  pixel ( $\sim 160$  nm for this experimental setup) at a global S/N of 7 were recorded, then a diffusion coefficient  $D_{app} = 2 \times 10^{-9} \text{ cm}^2/\text{sec}$  would have been obtained, although no molecular motion is reliably detected. A similar finding of apparent motion in single molecule tracking experiments due to experimental noise has been identified and discussed by Martin et al.<sup>42</sup>

#### 2.3.4 Utilizing the local S/N parameter in automated single molecule tracking experiments

Automated detection of diffusional heterogeneities over a short trajectory distance utilizing tracking software remains a cumbersome task.<sup>25,43</sup> The incorporation of local S/N analysis in addition to the recovered x,y-positions helps in identifying diffusional heterogeneities which are often accompanied with a change in quantum yield and local S/N ratio. This idea is demonstrated in Figure 2.8 in which a DiI molecule diffusing in DMPC at 37°C was tracked utilizing the local S/N analysis. The yellow highlighted

positions of the trajectory table indicate 3 differing S/Ns. An increase in S/N ratio likely indicates a stronger association of the fluorophores with the lipid environment, while a decrease is probably due to a blinking event or a decrease in intensity due to motion of the molecule during the observation time. This additional information is easily obtained during the analysis of a trajectory and greatly improves the interpretation of the x,y-position of a diffusing single molecule.

## 2.4 Conclusion

We presented an analysis method based on F-test statistics for discriminating actual subdiffraction molecular motion in single molecule tracking experiments from the apparent motion of stationary molecules that arises from a limited S/N ratio of the data. This statistical method is based on the concept of measuring squared displacement of a single molecule step and comparing this result to the apparent mean square displacement of stationary molecules at the same S/N ratio. A measured displacement above the critical value of the F-test confirms detection of molecular motion at a specified confidence level. This method was used in investigating the diffusional behavior of DiI fluorophores on a planar DMPC bilayer at three different temperatures (below, above and at the DMPC bilayer phase transition temperature). The results show an evolution in the diffusional behavior from purely stationary to mostly diffusive with increasing temperature. A correlation between an increase in local S/N and immobilization of DiI in DMPC bilayer was discovered, indicating a penetration of the DiI molecule into the gel-phase of the DMPC bilayer, as suggested by molecular simulation studies.<sup>39</sup>

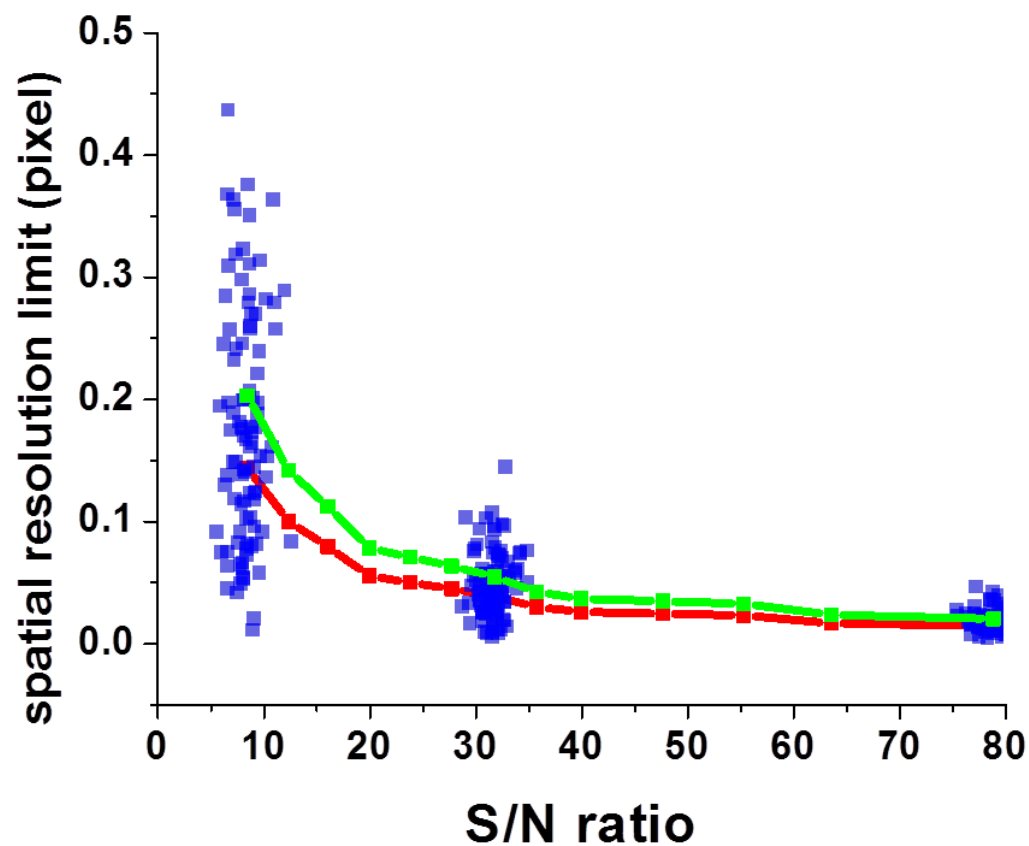
The results suggest the value of incorporating a local S/N analysis in automated tracking software for characterizing diffusional heterogeneities, which are often accompanied by changes in local S/N. The statistical method for discerning molecular motion from stationary molecules and the concept of computing local S/N should be useful in tracking and interpreting single molecule diffusional trajectories.

### 2.5 References

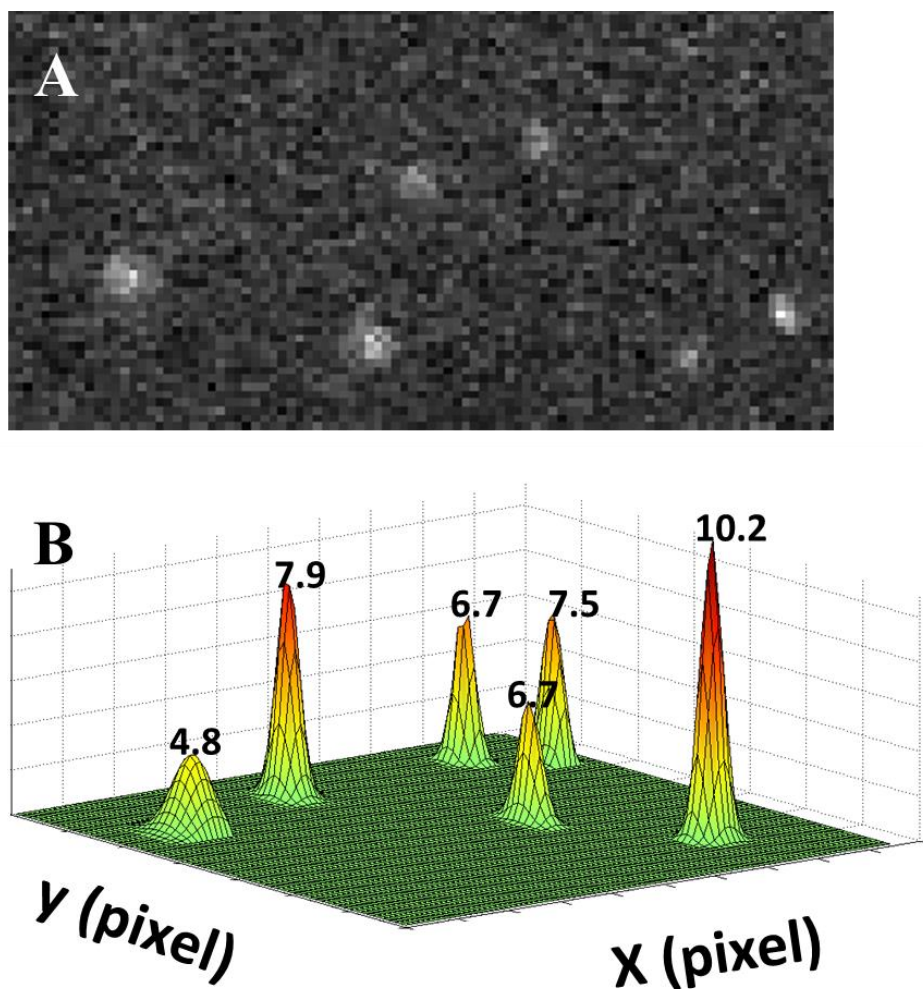
- (1) Huang, B.; Bates, M.; Zhuang, X. *Annu. Rev. Biochem* **2009**, *78*, 993.
- (2) Leung, B. O.; Chou, K. C. *Appl. Spectrosc.* **2011**, *65*, 967.
- (3) Galbraith, C. G.; Galbraith, J. A. *J. Cell Sci.* **2011**, *124*, 1607.
- (4) Kirstein, J.; Platschek, B.; Jung, C.; Brown, R.; Bein, T.; Brauchle, C. *Nat Mater* **2007**, *6*, 303.
- (5) Jung, C.; Schwaderer, P.; Dethlefsen, M.; Kohn, R.; Michaelis, J.; Brauchle, C. *Nat Nano* **2011**, *6*, 87.
- (6) Michaelis, J.; Brauchle, C. *Chem. Soc. Rev.* **2010**, *39*, 4731.
- (7) Joo, C.; Balci, H.; Ishitsuka, Y.; Buranachai, C.; Ha, T. *Annu. Rev. Biochem* **2008**, *77*, 51.
- (8) Yildiz, A.; Forkey, J. N.; McKinney, S. A.; Ha, T.; Goldman, Y. E.; Selvin, P. R. *Science* **2003**, *300*, 2061.
- (9) Greenleaf, W. J.; Woodside, M. T.; Block, S. M. *Annu. Rev. Biophys. Biomol. Struct.* **2007**, *36*, 171.
- (10) Bobroff, N. *Rev. Sci. Instrum.* **1986**, *57*, 1152.
- (11) Moerner, W. *Rev. Sci. Instrum.* **2003**, *74*, 3597.
- (12) Thompson, R. E.; Larson, D. R.; Webb, W. W. *Biophys. J.* **2002**, *82*, 2775.
- (13) Schütz, G. J.; Schindler, H.; Schmidt, T. *Biophys. J.* **1997**, *73*, 1073.
- (14) Schmidt, T.; Schütz, G. J.; Baumgartner, W.; Gruber, H. J.; Schindler, H.

- PNAS* **1996**, 93, 2926.
- (15) Patterson, G.; Davidson, M.; Manley, S.; Lippincott-Schwartz, J. *Annu. Rev. Phys. Chem.* **2010**, 61, 345.
- (16) Cheezum, M. K.; Walker, W. F.; Guilford, W. H. *Biophys. J.* **2001**, 81, 2378.
- (17) Gelles, J.; Schnapp, B. J.; Sheetz, M. P. *Nature* **1988**, 331, 450.
- (18) Yildiz, A.; Tomishige, M.; Vale, R. D.; Selvin, P. R. *Science* **2004**, 303, 676.
- (19) Svoboda, K.; Schmidt, C. F.; Schnapp, B. J.; Block, S. M. *Nature* **1993**, 365, 721.
- (20) Lohman, T. M.; Tomko, E. J.; Wu, C. G. *Nat Rev Mol Cell Biol* **2008**, 9, 391.
- (21) Neuman, K. C.; Saleh, O. A.; Lionnet, T.; Lia, G.; Allemand, J.-F.; Bensimon, D.; Croquette, V. *J. Phys.: Condens. Matter* **2005**, 17, S3811.
- (22) Tamm, L. K.; McConnell, H. M. *Biophys. J.* **1985**, 47, 105.
- (23) Fox, C. B.; Wayment, J. R.; Myers, G. A.; Endicott, S. K.; Harris, J. M. *Anal. Chem.* **2009**, 81, 5130.
- (24) Scomparin, C.; Lecuyer, S.; Ferreira, M.; Charitat, T.; Tinland, B. *Eur. Phys. J.E* **2009**, 28, 211.
- (25) Elliott, L. C. C.; Barhoum, M.; Harris, J. M.; Bohn, P. W. *PCCP* **2011**, 13, 4326.
- (26) Fox, C. B.; Myers, G. A.; Harris, J. M. *Appl. Spectrosc.* **2007**, 61, 465.
- (27) Peterson, E. M.; Harris, J. M. *Anal. Chem.* **2009**, 82, 189.
- (28) Heider, E. C.; Barhoum, M.; Edwards, K.; Gericke, K.-H.; Harris, J. M. *Anal. Chem.* **2011**, 83, 4909.
- (29) Berg, H. C. *Random Walks in Biology*; Princeton University Press, 1993.
- (30) Barlow, R. J. *A Guide to the Use of Statistical Methods in the Physical Sciences*; Wiley: Chichester, 1989.
- (31) Saxton, M. J. *Biophys. J.* **1993**, 64, 1766.

- (32) Sonnleitner, A.; Schütz, G. J.; Schmidt, T. *Biophys. J.* **1999**, *77*, 2638.
- (33) Saxton, M. J.; Jacobson, K. *Annu. Rev. Biophys. Biomol. Struct.* **1997**, *26*, 373.
- (34) McCain, K. S.; Hanley, D. C.; Harris, J. M. *Anal. Chem.* **2003**, *75*, 4351.
- (35) Xie, A. F.; Yamada, R.; Gewirth, A. A.; Granick, S. *Phys. Rev. Lett.* **2002**, *89*, 246103.
- (36) Derzko, Z.; Jacobson, K. *Biochemistry* **1980**, *19*, 6050.
- (37) Wu, E.; Jacobson, K.; Papahadjopoulos, D. *Biochemistry* **1977**, *16*, 3936.
- (38) Nakashima, N.; Kunitake, T. *J. Am. Chem. Soc.* **1982**, *104*, 4261.
- (39) Gullapalli, R. R.; Demirel, M. C.; Butler, P. J. *PCCP* **2008**, *10*, 3548.
- (40) Muddana, H. S.; Gullapalli, R. R.; Manias, E.; Butler, P. J. *PCCP* **2011**, *13*, 1368.
- (41) Dertinger, T.; von der Hocht, I.; Benda, A.; Hof, M.; Enderlein, J. *Langmuir* **2006**, *22*, 9339.
- (42) Martin, D. S.; Forstner, M. B.; Käs, J. A. *Biophys. J.* **2002**, *83*, 2109.
- (43) Smith, Matthew B.; Karatekin, E.; Gohlke, A.; Mizuno, H.; Watanabe, N.; Vavylonis, D. *Biophys. J.* **2011**, *101*, 1794.

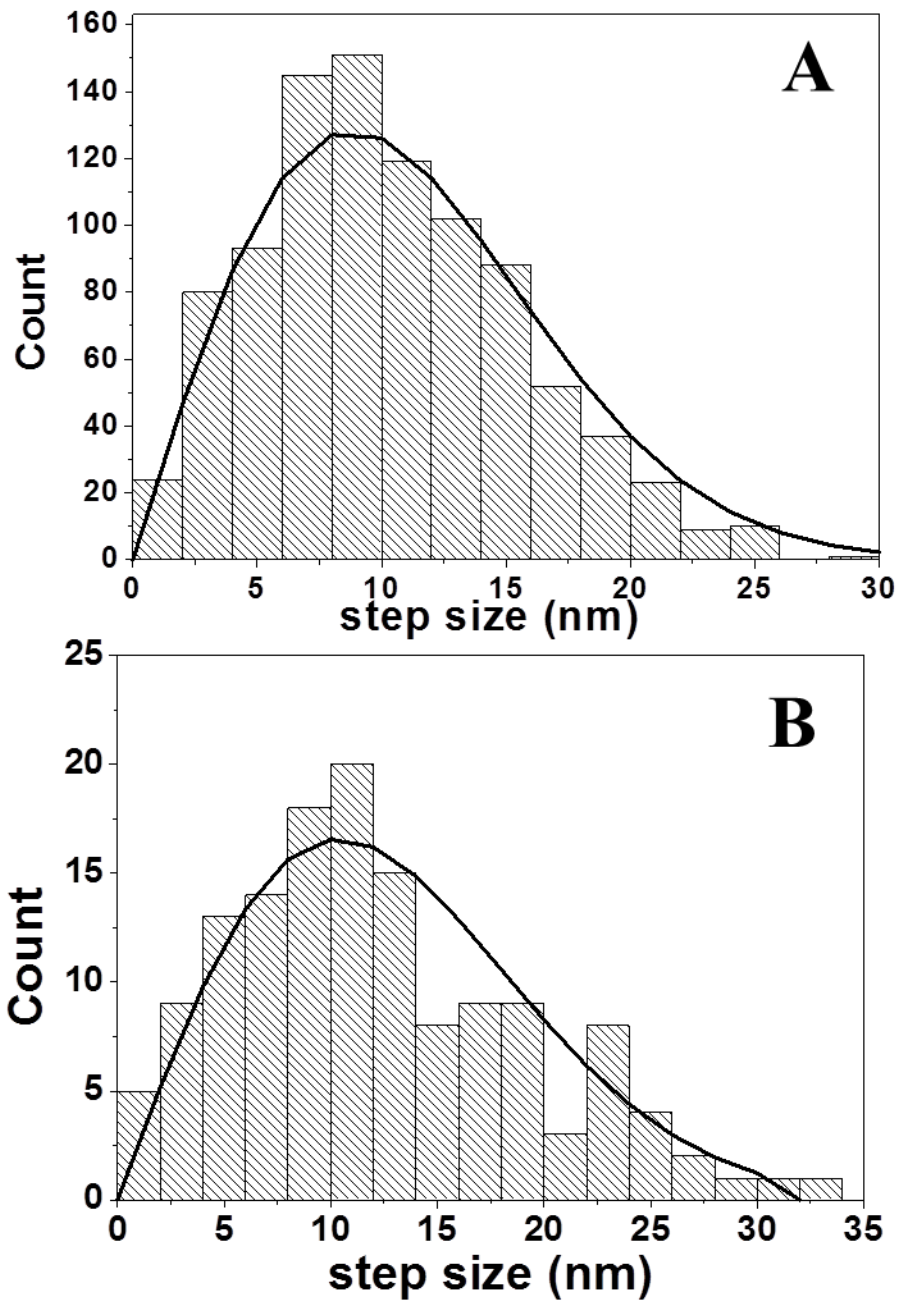


**Figure 2.1:** Plot of the mean standard deviation in position-difference (red curve) and the standard deviation in apparent step sizes (green curve) of simulated stationary single molecules at varying S/N. Scatter plots of the apparent step sizes are generated from the same data set (blue squares).

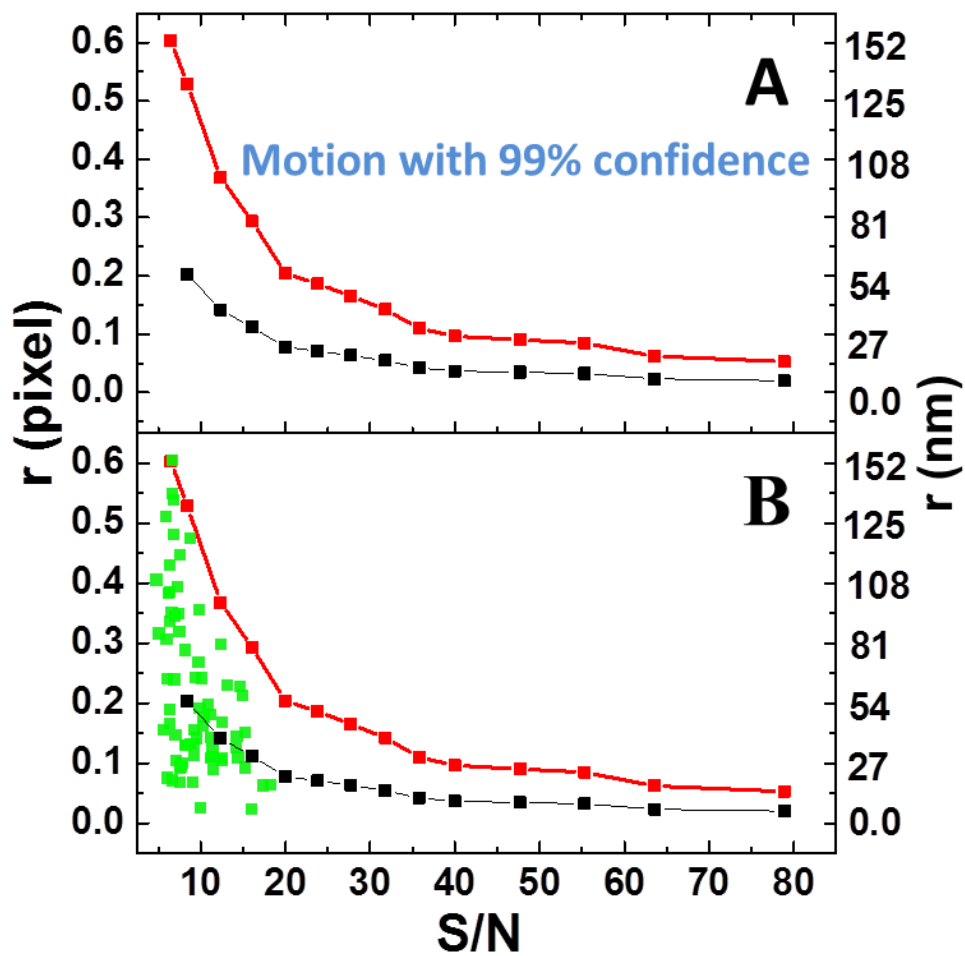


**Figure 2.2:** Raw data image (A) and 3D contour plot (B) of stationary DiI molecules fitted to 2D Gaussian functions and their corresponding local S/Ns. The local S/N was determined by computing the ratio of the fitted Gaussian amplitude to the standard deviation of the background.

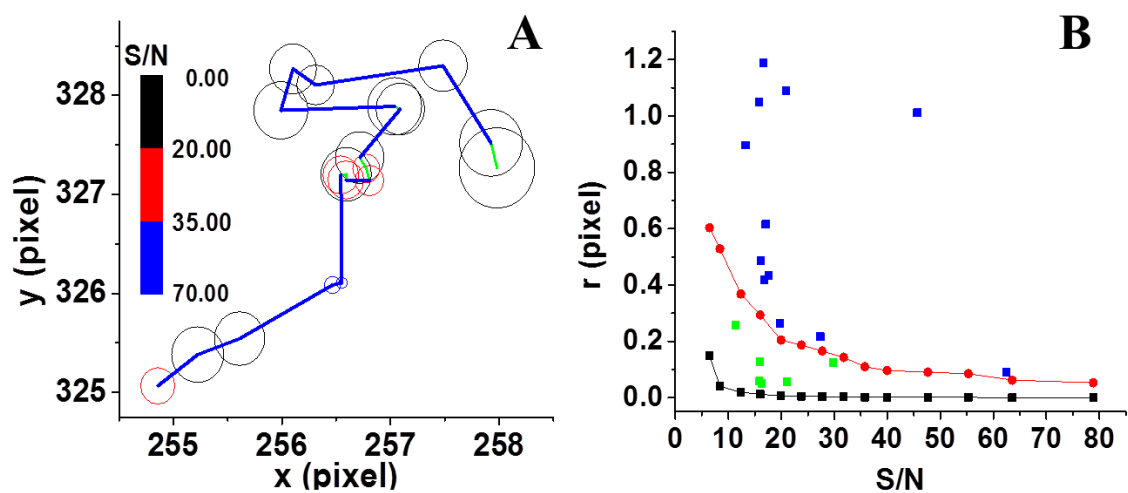




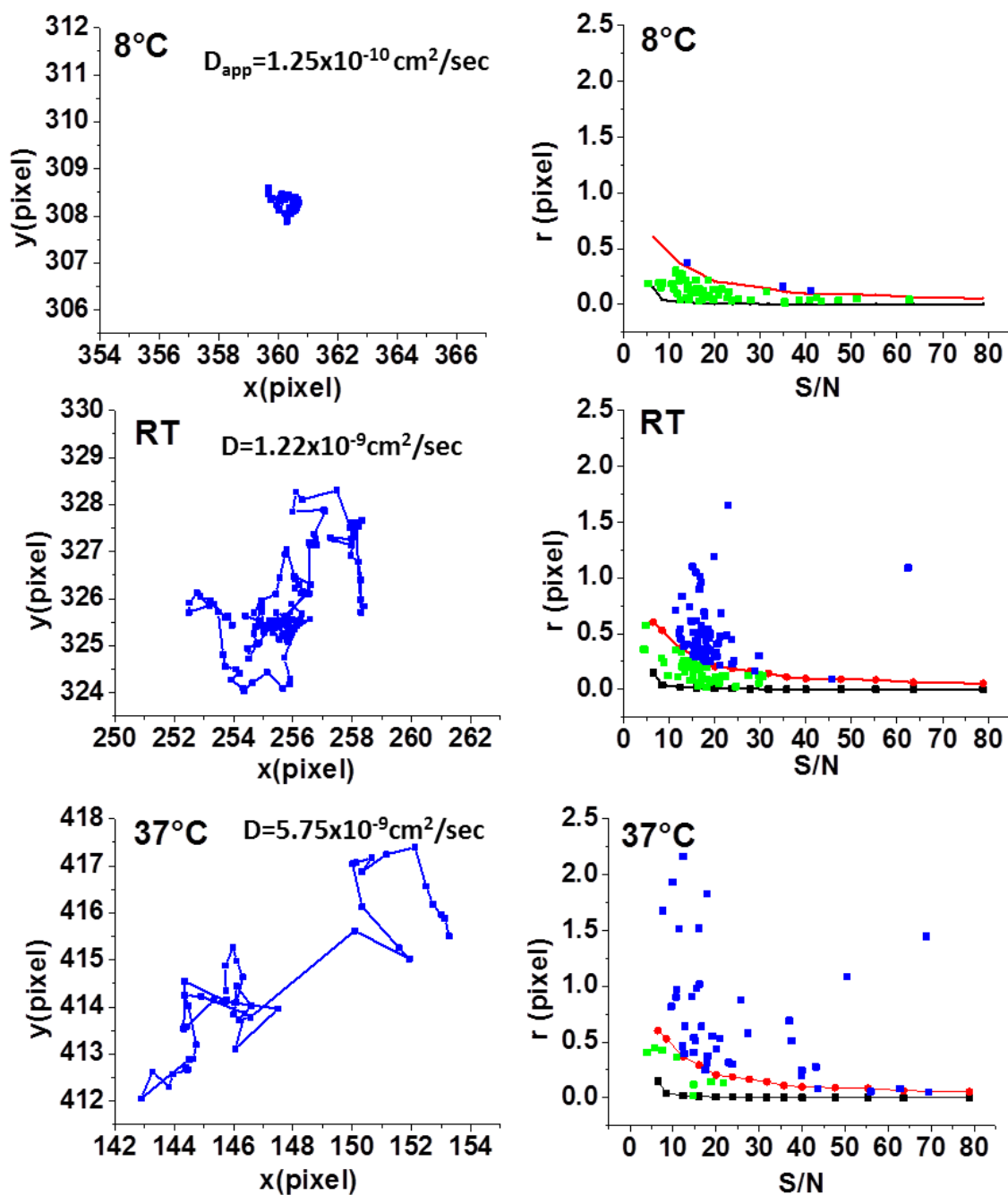
**Figure 2.3:** Histogram plots of the apparent step sizes of (A) simulated and (B) experimentally measured stationary DiI molecules. Fits are to equation 3.



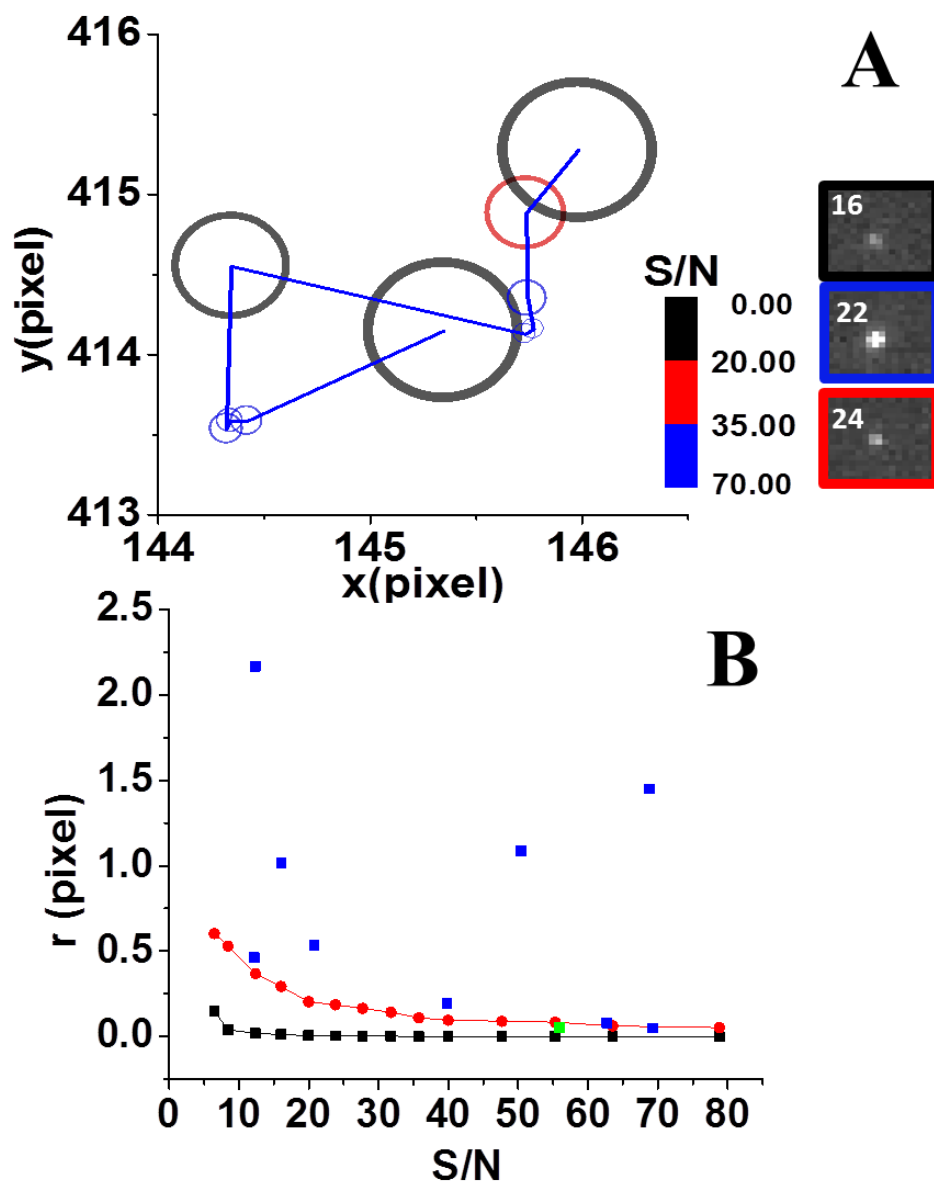
**Figure 2.4:** Apparent motion plot generated from simulated stationary DiI molecules and a 99% F-test confidence boundary (red line) for no detection of molecular motion (A). Additional scatter plot of the apparent motions of imaged adsorbed DiI molecules (B).



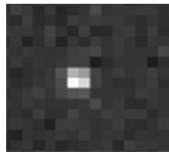
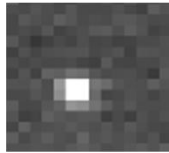
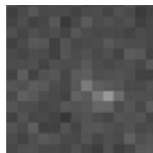
**Figure 2.5:** Trajectory plot of a single DiI fluorophore diffusing on DMPC at room temperature (A). Circle radii represent the boundary for no detection of molecular motion (green segments). Circle color represents the magnitude of the local S/N. (B) Apparent motion error-plot for the corresponding trajectory in (A). Green squares represent the apparent steps and the blue squares the detected steps in the trajectory.



**Figure 2.6:** Plots of representative DiI trajectories on a DMPC bilayer at varying temperatures and their corresponding apparent motion error plots. The calculated diffusion coefficient at 8°C represents an apparent diffusion coefficient.



**Figure 2.7:** Zoom-in of the DiI trajectory on DMPC at 37°C from Figure 2.6 including three original images with varying local S/N (A). Local S/N ratios are coded by the frame color of the images. The number in the images represent the trajectory position the image was taken. (B) Corresponding apparent motion plot of trajectory in (A).

X(PIXEL)	Y(PIXEL)	S/N	step(PIXEL)	
144.90406	414.23078	19.1387	0.55441	→ 
146.37825	413.86173	15.9085	1.51969	
146.06129	413.10779	9.58021	0.81785	
145.34719	414.14642	12.3209	2.16701	
144.41925	413.58279	50.4012	1.0857	
144.33945	413.58359	62.7427	0.0798	→ 
144.32333	413.53284	55.9239	0.05325	
144.34607	414.55018	16.0669	1.0176	
145.73205	414.12636	68.7601	1.44933	
145.77156	414.15644	69.3049	0.04965	
145.74445	414.34853	39.7966	0.19399	
145.73775	414.8819	20.7907	0.53341	
145.98247	415.27389	12.1871	0.46211	
146.10215	414.97937	17.9484	0.3179	
146.317	414.63705	14.7462	0.40416	
146.10253	414.09866	27.3018	0.57954	
146.17583	413.73342	15.1308	0.51279	
146.57663	413.7846	3.95187	0.40405	→ 

**Figure 2.8:** Automated tracking data from DiI diffusing on DMPC at 37°C.

Trajectory table includes the computational results of the local S/N of the trajectory.

Three original images represent varying diffusional or photo-physical behavior detected by significant variation in the computed local S/N of the automated tracking software.

## CHAPTER 3

### SINGLE MOLECULE TRACKING STUDIES OF LOWER CRITICAL SOLUTION TEMPERATURE TRANSITION BEHAVIOR IN POLY (N-ISOPROPYLACRYLAMIDE)

Adapted with permission from: Lindsay C.C. Elliott\*, Moussa Barhoum\*, Joel M. Harris, and Paul W. Bohn, *Single Molecule Tracking Studies of Lower Critical Solution Temperature Transition Behavior in Poly(N-isopropylacrylamide)*, *Langmuir*, **2011**,27,(17), pp11037-11043, American Chemical Society. \*contributed equally to this work

#### 3.1 Introduction

Stimulus-responsive materials (SRMs) have attracted enormous attention due to their ability to react to external stimuli by increasing or decreasing the free volume between individual polymer chains, resulting in the transport of water into or out of the material, thus producing changes in size or shape of polymer brushes consisting of these materials. Physical and chemical properties such as free volume, thickness, hydrophilicity, and charge state can all be controlled by modulating polymer density, degree of cross-linking, and chemical environment.<sup>1-4</sup> A variety of external stimuli, e.g., electric field, ionic strength and pH of the surrounding solution, analyte concentration,

and light exposure, have been exploited to initiate shape/size/property transitions in different SRMs.<sup>5-7</sup>

One model SRM, poly(N-isopropylacrylamide), pNIPAAm, is a temperature responsive polymer that exhibits a lower critical solution temperature (LCST), at which a transition occurs - from an expanded hydrophilic form ( $T < T_{LCST}$ ) to a collapsed, hydrophobic morphology ( $T > T_{LCST}$ ).<sup>8,9</sup> The LCST phenomenon in pNIPAAm is of great interest technologically due to its proximity to human body temperature. Thus, applications in controlled drug delivery have been widely studied, and although the phenomenology is controllable, the underlying physical and chemical behavior is found to be quite complex. Thus, the temporal and spatial heterogeneities exhibited in the temperature responsive polymer are particularly relevant to the loading and unloading of drug delivery devices. In addition, the ability to realize size and shape control on the nanometer length scale holds considerable promise for applications in tissue engineering, drug delivery systems, biosensors and actuators, and synthetic extracellular matrices.<sup>10</sup> However, at present, nanoscale SRM structures must be designed and tested empirically, since the behavior of SRMs is not understood well enough to support rational design with such fine control. Detailed, molecular-level information is needed, which could be used to develop predictive models for stimulus-initiated molecular reorganization.

In order to examine the temperature-dependent behavior of SRMs on a single molecule level, the motions of fluorescent probes, Rhodamine6G (R6G), within surface-bound thin-films of pNIPAAm prepared by atom transfer radical polymerization (ATRP), are studied using single molecule tracking (SMT). SMT has become a viable research tool within the last two decades<sup>11-17</sup> after technological advances in collection device



efficiency and in fluorophore quantum yield and lifetime. In SMT, the paths of intrinsic, inserted, or tagged probe molecules are tracked in order to gain information about position and mobility.<sup>18</sup> This technique has the advantage of interrogating the population of fluorophores on an individual basis, thus collecting and preserving spatial and temporal heterogeneities. SMT has been applied to various complex systems, such as hierarchical mobility in polymer networks,<sup>19</sup> molecular transport in thin silica sol-gel films,<sup>20</sup> membrane dynamics,<sup>21</sup> hydrophobic interactions of amphiphilic molecules at hydrophobic/water interfaces,<sup>22</sup> and pore dynamics within polyacrylamide gels.<sup>23</sup> In addition, initial fluorescence correlation spectroscopy experiments have recently been carried out to measure the diffusion of probe fluorophores in pNIPAAm.<sup>24</sup> Of particular interest in our laboratories is the use of SMT to understand the molecular-scale behavior of SRMs for use in actively controlled micro total analysis systems ( $\mu$ TAS).<sup>25</sup> Thus, SMT is a very attractive approach for real time investigation of spatial and temporal heterogeneities in the structure of soft materials undergoing molecular reorganization at or near the LCST. In addition to the specific temperature-responsive behavior of pNIPAAm studied here, the methodology can be extended to investigate the underlying basis for a wide range of soft material dynamic properties.

## 3.2 Experimental Section

### 3.2.1 Reagents and materials

Unless otherwise noted reagents and solvents were obtained from Sigma Aldrich., Rhodamine 6G (99%, Acros), 11-trichlorosilyundecyl-2'-bromo-2-isobutyrate (silane

initiator) (95+%, ATRP Solutions), hexanes (ACS reagent, 99.9%, Fisher), dichloromethane (DCM, Chromasol Plus), ethanol (EtOH, denatured for HPLC, Acros), isopropanol (IPA, ACS reagent, >99.5%), cuprous bromide (CuBr, 99.999%), ethanol (EtOH, 99%, Fisher), and dimethyl formamide (DMF, ACS reagent, >99.8%) were used as received. N-isopropylacrylamide (NIPAAm, 97%) was purified by running a 1:1 hexanes/DCM saturated solution through a 2.5 cm basic alumina column, removing the solvent by reduced pressure evaporation, recrystallizing the remaining solid in hot hexanes at < 50°C, rinsing with minimal ice cold hexanes, and removing the solvent by reduced pressure evaporation. Methanol (MeOH, ACS reagent, 99.9%, Fisher), pentamethyldiethylene-triamine (PMDETA, 99%) and deionized (DI,  $\rho = 18 \text{ M}\Omega \text{ cm}$ , Millipore Corp.) water were degassed by bubbling argon for 5-10 minutes and immediately transferred into the glovebox.

### 3.2.2 Sample preparation

Synthetic methods are described in detail elsewhere;<sup>26</sup> a brief description is as follows. Samples of surface bound pNIPAAm brushes of 70 nm unhydrated thickness were prepared by: (1) cleaning the substrate (silicon or glass) with piranha solution; (2) forming a monolayer of silane initiator, 11-trichlorosilyundecyl-2'-bromo-2-isobutyrate, on a substrate for ATRP was accomplished by liquid deposition; and (3) growing polymer using an ATRP grafting-from approach starting with the initiator monolayer in the presence of N-isopropylacrylamide, CuBr and pentamethyldiethylenetriamine (PMDETA) in 30 mL of 1:1 v:v MeOH/water in an oxygen-free atmosphere. Immediately after growth polymer thickness was characterized with profilometry (Sloan

Dektak3 ST) and/or ellipsometry (Gaertner Variable Angle Stokes Ellipsometer L116S). Single fluorescent R6G molecules, used as the fluorescent probe, were partitioned into pNIPAAm film target media by immersion of the film in DI H<sub>2</sub>O followed by addition of 1 nM R6G in methanol until a final concentration of 3.3 pM was reached. After partitioning, the film was imaged immediately.

### 3.2.3 Temperature-controlled ellipsometry

A custom built cell with polystyrene windows at 70° angles (normal to the incident and reflected laser light) was used to collect ellipsometry data. The aluminum floor of the cell was glued with silver epoxy to an aluminum disc that was fitted with a temperature collar (Bioptechs) with 0.1°C resolution capable of producing temperatures in the range  $\sim 19^{\circ}\text{C} < T < 43^{\circ}\text{C}$  depending on ambient room temperature. The polymer on silicon sample was placed inside the cell and immersed in DI water. Ellipsometry data were collected at temperatures  $19^{\circ}\text{C} < T < 32^{\circ}\text{C}$  at  $\sim 1^{\circ}\text{C}$  intervals at  $\lambda = 632.8$  nm, with refractive index and thickness of the polymer layer simultaneously determined. Solution temperatures were measured using two separate thermistors in close proximity to the sample. The refractive index and thickness of the polymer layer were determined from  $\Psi$  and  $\Delta$  using the Gaertner GEMP software following standard single wavelength ellipsometry calculations.<sup>27,28</sup>

### 3.2.4 Single molecule fluorescence microscopy

Instrumentation and data acquisition parameters are described in detail elsewhere;<sup>26</sup> a brief description follows. The microscope is an objective-based total

internal reflection fluorescence (TIRF) microscope, exhibiting a 100-200 nm depth of excitation and an effective pixel size of 267 nm x 267 nm with 60X magnification. Each frame was acquired with a 30 ms exposure, using frame transfer to eliminate delay time between frames. The acquisition protocol produced videos consisting of 1000 frames, which were obtained at 23°C and at 32°C in DI water. The temperature was controlled through a Peltier-controlled stage, described in detail elsewhere.<sup>29</sup> Briefly, a Peltier heating/cooling device with a custom built aluminum sample holder and a copper block where used to control and stabilize the temperature inside the sample holder. Temperature was monitored using a thermocouple immersed in the solution of the sample holder. Single molecule tracking was carried out in a modified Matlab program developed<sup>30,31</sup> specifically for SMT.<sup>18,32</sup> Briefly, tracking consists of the linked tasks of identification, localization and trajectory reconstruction. Identification and localization were realized by fitting the spatial intensity profile of each suspect molecule to a 2-D Gaussian,

$$I(x, y) = \exp \left[ -\frac{(x-x_0)^2}{2\sigma_x^2} - \frac{(y-y_0)^2}{2\sigma_y^2} \right] \quad [3.1]$$

from which the centroid  $(x_0, y_0)$  and the peak standard deviations  $(\sigma_x, \sigma_y)$  were obtained using a weighted linear least squares fit. The ratio of the peak height,  $I_0$ , to the standard deviation of the noise in the area adjacent to the peak was used to calculate the S/N and to determine if the peak qualified as a candidate single molecule. Localization was achieved by identifying the center of the 2D Gaussian, i.e.,  $(x_0, y_0)$ . If the S/N ratio is

sufficient, then the centroid can always be localized to better precision than the diffraction limit.<sup>31,33</sup> After every feature was identified in each frame, the frames were stacked in a movie and trajectories were linked together throughout the course of the movie.

### 3.2.5 Spatial resolution analysis

The limit of resolving motion in the images was first tested by simulating stationary fluorescent spots under varying S/N ratios and then applying the same tracking algorithms to the analysis of these simulated data. The S/N ratio for a given image was varied by first generating a Poisson distributed background at a mean intensity equivalent to that observed in the data, and then adding fluorescent spots modeled with a Gaussian function having a width given by the measured point-spread function (PSF) with Poisson distributed intensity noise. The apparent center locations  $(x_0, y_0)$  of these immobilized spots were then determined by the same tracking and localization algorithm as described above. A plot of the root-mean-square variation (standard deviation) of these  $x_0, y_0$  positions at different S/N ratios estimates the limit at which mobile and immobile fluorescent spots may be distinguished, which depends on the S/N ratio of the data. In order to test the predictions of this simulation, time-resolved images of immobilized R6G molecules deposited on a glass surface by dip coating from dilute ethanol solution<sup>34,35</sup> were acquired on the same microscope under the same conditions of molecular tracking experiments (with 30 ms exposures in frame transfer mode). The measured S/N ratio of these stationary single-molecule spots was 15, and the root-mean-square uncertainty in their positions was 16 nm. In order to generate higher S/N data to compare with the

simulation results (and the higher S/N fluorescence from R6G diffusing in pNIPAAm), corresponding pixel intensities from multiple sequential frames from the same stack were added to generate a smaller series of frames. These co-added images had correspondingly greater molecular peak intensity and lower relative noise to provide higher S/N experimental data compare with the simulation results and the apparent motions of R6G in pNIPAAm.

### 3.2.6 Single molecule data analysis software and analysis

Confinement level functions in Matlab were modified to accept trajectory data from an existing tracking program and experimental protocol; this modified function is available online<sup>26</sup> and the rest of the program is available from the original authors.<sup>36</sup> Radius of gyration code was written in Matlab and is available online.<sup>26</sup> Gaussian and Lorentzian fits of the probability density functions for parameters from  $R_g$  evolution and confinement level calculations were carried out. The choice of model and number of peaks for each fit was determined by the best match to data in order to characterize peak position and width. No physical model is inferred from these fits.

## 3.3 Results and Discussion

### 3.3.1 Ellipsometry of hydrated pNIPAAm

Figure 3.1 shows the temperature response of a hydrated pNIPAAm brush on a silicon wafer, which exhibited 80 nm dry thickness. The ellipsometry results illustrate that the brush is thickest at 21°C and simultaneously reduces its thickness and increases its refractive index continuously until 32°C, with a ~20% decrease in free volume based

on water content change. The gradual thickness transition observed here is typical for high density pNIPAAm brushes<sup>37</sup> as reported in the literature from surface plasmon resonance,<sup>38</sup> water contact angle,<sup>39,40</sup> quartz crystal microbalance,<sup>41</sup> neutron reflectometry,<sup>42</sup> sum frequency generation,<sup>43</sup> surface forces apparatus,<sup>44</sup> atomic force microscopy,<sup>44</sup> proton NMR,<sup>45</sup> neutron reflectometry,<sup>4,46</sup> cyclic voltammetry,<sup>47</sup> and ellipsometry.<sup>48</sup> These measurements were used to determine data collection temperatures, 23°C and 32°C, for the SMT experiments, at which maximal differences in transport behavior might be expected.

### 3.3.2 Single molecule tracking

Four separate movies of R6G probes in the same pNIPAAm sample (70 nm unhydrated thickness, extrapolated to hydrated thicknesses from Fig. 3.1; 115 nm expanded at 23°C and 100 nm collapsed at 32°C) and the same field of view were analyzed, two each at 23°C and 32°C to assess the reproducibility of data collection. Trajectories are commonly limited in length by photobleaching and other processes that convert probes to long-lived dark states.<sup>35,49,50</sup> Because short trajectories are less useful for identifying differences between levels of confinement within a single track, only trajectories longer than 50 steps were used for further analysis, which resulted in 340 trajectories (29159 total steps) and 236 trajectories (18923 total steps) from the two movies at 23°C, and 1150 trajectories (99085 total steps), and 1238 trajectories (104565 total steps) from the movies at 32°C. The trajectories for R6G probes from SMT datasets at 23°C and 32°C are shown in Figure. 3.2 and 3.3, respectively. It is immediately evident that the partitioning coefficient of R6G into pNIPAAm is larger at 32°C than at

23°C, resulting in many more trajectories at the higher temperature. However, the initial concentration is sufficiently small, even at 32°C, that it did not affect tracking results, meaning that there was negligible occurrence of probe-probe interactions, which could begin to occur when two probes occupy adjacent pixels in the same frame. However, even if probe molecules appear in adjacent pixels, they are hundreds of nanometers from each other within the x-y plane of the brush and can be many tens of nanometers from each other in the perpendicular z direction due to the film thickness. Therefore, remembering that the plots in Figs.3.2 and 3.3 are compilations through all 1000 frames of a movie, using adjacent molecule-molecule appearances as a conservative criterion would still result in overestimating probe-probe events and these events were exceedingly rare. The probability that two molecules are occupying the same pixel range is readily calculated with the Poisson distribution,

$$P(n) = \frac{\lambda^n e^{-\lambda}}{n!} \quad [3.2]$$

where  $\lambda$  is the probability of finding one molecule in a picture element and  $n$  is the number of events in a picture element, which can be determined from experimental parameters. The size of a frame (262144 pixels), size of a single molecule point spread function (9 pixels) and number of features per frame (~300) result in a 1% chance of observing a molecule in one 9 pixel range,  $\lambda$ . The Poisson distribution thus predicts there is less than 0.003% probability of observing two molecules in the same 9 pixel range.



Position and mobility of the probes are the main focus of the present study. Therefore trajectories were used initially to quantify the movement of probe molecules such as space explored and time spent in localized areas. In addition, the metrics can be used to categorize probes into one of three classes as having: (a) small constant mobility (confined), (b) relatively large mobility (unconfined), and (c) those exhibiting one or more transitions between low and high mobility states (intermittent confinement). These analysis methods are carried out with the aim of exploring free volume changes in the polymer films through the changes in probe mobility.

It is critical in this analysis to discriminate between low-mobility, confined diffusion of molecules within small domains in the polymer film, on the one hand, and strong interactions with fixed adsorption sites in the polymer that lead to molecules that are not moving on the time-scale of the observations, on the other. The question to be addressed is whether the measured motion of these low-mobility molecules exceeds the apparent motion of a dye molecule that is adsorbed to a surface and not moving. If the root-mean-square displacement of a R6G molecule during a confinement event clearly exceeds the apparent root-mean-square displacement of immobilized R6G molecules adsorbed to a surface, then the molecule is indeed diffusing within an entangled polymer domain. To test this question, both simulated and experimentally measured apparent root-mean-square displacements of stationary R6G molecules were compared at different S/N ratios, with excellent agreement between the experimental and simulated results; see Fig. 3.4. With higher S/N ratio, the resolution limits of discriminating moving versus immobile molecules improves, where experimental results find apparent root-mean-square displacements for adsorbed R6G at a glass-air interface of 31 nm, 19 nm and 8 nm

for S/N ratios of 13, 22, and 45, respectively. The root-mean-square displacement of confined R6G molecules in pNIPAAm above the transition temperature is 50 nm for a S/N ratio of 20 and below the transition temperature is 75 nm for a S/N ratio of 15; see Fig. 3.4. The difference in S/N at 23°C and 32°C may be explained by a combination of increased excitation intensity, as the brush collapse at higher temperatures brings the imbedded fluorophores closer to the substrate by ~20 nm, which is significant in an exponentially decaying TIRF field, and the brush collapse at higher temperatures leading to a more hydrophobic environment that increases the emission quantum yield of the R6G. At S/N 20, the resolution limit (root-mean-square apparent displacement of stationary molecules) is determined from simulation to be 20 nm. Therefore, the motion of confined molecules can be clearly distinguished from the apparent motion of stationary molecules, indicating that formation of polymer entanglement domains is responsible for the confined regions of the trajectories, rather than adsorption to molecular-scale sites in the film.

The diffusion coefficient,  $D$ , obtained from the slope of mean squared displacement,  $\langle x^2 \rangle$ , versus time delay,  $\tau$ , is a commonly used metric when quantifying motion<sup>11,34</sup> and useful as an initial analysis of the magnitude of mobility in these experiments. In addition, the shape of the  $\langle x^2 \rangle$  vs.  $\tau$  trace is an indication of the type of diffusion in the system-confined (sublinear), Brownian (linear), or diffusion with flow (superlinear). However, individual probe variation and randomly intermittent behavior is lost in the averaging of the squared displacement. Thus, it is important to distinguish  $D$  values calculated for individual probes and those for ensemble averages over many probe

molecules, and  $D$  values calculated for categorized segments. The ensemble-averaged diffusion coefficient ( $D_{\text{ens}}$ ) calculated for the molecules studied in these experiments lies in the range  $0.18 \mu\text{m}^2 \text{s}^{-1} < D_{\text{ens}} < 0.36 \mu\text{m}^2 \text{s}^{-1}$  independent of temperature. Since this cursory inspection of population-averaged diffusion coefficients produces the same  $D_{\text{ens}}$  at  $23^\circ\text{C}$  and  $32^\circ\text{C}$  trajectories, despite the known LCST phase transition in the SRM, clearly a more thorough analysis is warranted.

Analysis of the temperature specific behavior of R6G probes was carried out using a suite of robust statistical tools available for comparison of SMT data.<sup>26</sup> Among the available tools, confinement level analysis<sup>36,51</sup> and radius of gyration evolution<sup>26</sup> were found to be useful in distinguishing between pNIPAAm states and physical properties above and below the LCST. Confinement level calculations are carried out on a molecule-by-molecule basis in order to determine ‘confined’ and ‘free’ segments, i.e., portions or whole trajectories that exhibit higher and lower relative confinement relative to a well-defined threshold. Several metrics are obtained from these results, including the fraction of confined steps within the trajectory,  $\alpha$ , the duration of confined and free portions of the trajectory, and the radii of free and confined zones. Once evaluated from SMT movies, these quantities can be compiled for all trajectories into histograms that convey the distribution of behaviors observed across the entire sample. The radius of gyration,  $R_g$ , of a trajectory describes the amount of space that the molecule explores during its movement, calculated as the root mean square distance from the trajectory’s center of mass,

$$R_g = \sqrt{R_1^2 + R_2^2} \quad [3.3]$$

where  $R_1$  and  $R_2$  are the major and minor eigenvalues, respectively, of the radius of gyration tensor,  $T$ . The tensor  $T$  is calculated from the  $x$  and  $y$  positions of the particle throughout its trajectory,

$$\hat{T} = \begin{bmatrix} \frac{1}{N} \sum_{j=1}^N (x_j - \langle x \rangle)^2 & \frac{1}{N} \sum_{j=1}^N (x_j - \langle x \rangle)(y_j - \langle y \rangle) \\ \frac{1}{N} \sum_{j=1}^N (x_j - \langle x \rangle)(y_j - \langle y \rangle) & \frac{1}{N} \sum_{j=1}^N (y_j - \langle y \rangle)^2 \end{bmatrix} \quad [3.4]$$

Thus, radius of gyration evolution quantifies the amount of space that a molecule explores over the course of the experiment. This value evolves over time for each molecule as motion is tracked and can be plotted vs. time in order to observe the progression.  $R_g$  evolution is especially useful in allowing the statistical outliers, for example molecules that exhibit multiple confined-to-mobile or mobile-to-confined transitions, to be identified in the presence of the ensemble-average behavior. In addition, all the values of  $R_g$  or the final  $R_g$  for each molecule can be plotted in a histogram to parse out measurable differences.

### 3.3.3 Confinement level calculations<sup>36,51</sup>

Free and confined portions of each trajectory were compiled separately, from which individual probe molecule diffusion coefficients were determined from the mean squared displacement. Averaging over all segments placed in each category from all four movies yields  $D_{confined} = 0.007 \pm 0.004 \mu\text{m}^2 \text{s}^{-1}$  and  $D_{free} = 1.27 \pm 0.24 \mu\text{m}^2 \text{s}^{-1}$  (the two 23°C movies averaged  $D_{confined} = 0.010 \pm 0.005 \mu\text{m}^2 \text{s}^{-1}$  and  $D_{free} = 1.13 \pm 0.20 \mu\text{m}^2 \text{s}^{-1}$  while the two 32°C movies average  $D_{confined} = 0.004 \pm 0.002 \mu\text{m}^2 \text{s}^{-1}$  and  $D_{free} = 1.42 \pm 0.22 \mu\text{m}^2 \text{s}^{-1}$ , i.e., the confined and free diffusion coefficients are statistically the same at

the two temperatures). The ‘confined’ diffusion segment can be considered immobile within the limits of the instrument, given the tracking limit average 40 nm displacements from immobilized R6G on glass, which yields a minimum diffusion coefficient of  $0.013 \mu\text{m}^2 \text{s}^{-1}$  with 30 ms exposures. As with the ensemble averaged  $D$ , these values are helpful as a guide to the magnitude of the mobility corresponding to qualitatively distinct trajectory segments. In addition, they clearly define how much separation exists between the indicators for confined and free behavior observed overall in these samples. The next step beyond statistical description of confined and mobile segments examines the confinement level calculations of  $\alpha$  which show a consistent difference between temperatures above and below the LCST, as shown in Fig. 3.5. Consistent differences between high and low temperature fraction of confinement can be clearly observed in both the peak positions and widths of the  $\alpha$  distributions. Both of the high temperature experiments evince a large fraction of confined steps, while the  $23^\circ\text{C}$  data exhibit smaller peak  $\alpha$  values. More strikingly, the low temperature distributions have a much longer tail at smaller  $\alpha$  values, indicating a larger number of trajectories that exhibit a smaller fraction of confined steps. The usual increase in diffusion coefficient with temperature predicted by the Stokes-Einstein equation, corresponding to an increase in MSD under free diffusion conditions, stands in contrast to the larger degree of confinement at higher temperature seen in these data. This obvious, reproducible indication of the higher level of confinement at  $32^\circ\text{C}$  correlates well with the collapsed state of pNIPAAm, in spite of the increased thermal energy available to the probes.

Two additional metrics that can be extracted from confinement level analysis provide interesting insights into the differences between states of pNIPAAm above and

below the LCST. Fig. 3.6(a) shows the duration of confined events, compiled as histograms of the confined portions of all trajectories. The 32°C traces (red) clearly show a long duration tail, giving a distribution that can be fit by a double Lorentzian function, while the 23°C traces (blue) show a single peak that fits a single Lorentzian. Furthermore, the fit parameters confirm that the higher temperature distributions exhibit a second population of confined probe molecules that are immobile for  $\sim 4$  times as long as the main part of the population. Additional insight into this phenomenon can be gleaned from the Lorentzian fits for the distributions of confined zone radii displayed in Fig. 3.6(b), which also exhibit systematic differences between  $T > T_{LCST}$  and  $T < T_{LCST}$ . At 23°C the radii of confined zones in the two experiments peak are 54 nm with FWHM 70 nm and 43 nm with FWHM 31 nm, while at 32°C the distributions are sharper and smaller at 32 nm with FWHM 20 nm and 31 nm with FWHM 20 nm, a 34% average decrease at higher temperature. The low temperature data show a larger variation in width than the high temperature data, but the difference in behavior is clear.

When considered together, the confinement level analysis shows that in the 32°C state R6G probes in pNIPAAm: (i) exhibit a higher fraction of confined steps, (ii) are confined for longer periods of time, and (iii) are confined to smaller areas than in the 23°C state. In addition, the fact that two Lorentzian peaks best fit the duration of confined event histograms at 32°C suggests that there may be more than one distinct confinement mechanism in pNIPAAm above the LCST.

### 3.3.4 Radius of gyration evolution

Radius of gyration evolution for two experiments, one at 23°C and the other at 32°C, are shown in Figs. 3.7(a) and 3.7(b), respectively. Only trajectories longer than 150 steps were included in these two plots in order that individual traces could be visually resolved. Differences between low and high temperature probe movement are readily apparent. Relatively immobile molecules, showing little increase in  $R_g$  over the course of the trajectory, and intermittent confinement behavior, as evidenced by consecutive increases and plateaus/decreases in  $R_g$ , are observable in both plots. However, the magnitude is clearly different above and below  $T_{LCST}$ . The difference in probe mobility between low and high temperature can be seen in the histogram of final  $R_g$  values for each molecule (trajectories longer than 50 steps) shown in Fig. 3.8. Clearly, a larger fraction of the trajectories end with higher final  $R_g$  values at 23°C than at 32°C, even though the most probable  $R_g$  values are near 50 nm, indicating confinement, at both temperatures. In addition, there is a small increase in the peak final  $R_g$  values going through  $T_{LCST}$ . Although the 23°C data show more heterogeneity in peak position and width, on average these values are larger for the low temperature pNIPAAm films (70 nm with FWHM 71 nm and 48 nm with FWHM 29 nm) than for those studied at high temperature (46 nm with FWHM 29 nm and 46 nm with FWHM 17 nm).

These results agree with those obtained from confinement level analysis, thereby augmenting the evidence for enhanced confinement in pNIPAAm at  $T > T_{LCST}$ . At 23°C the average radius of confinement of trajectory segments is 49 nm and the average final  $R_g$  is 59 nm, an increase of 20%. At 32°C the corresponding values are 32 nm and 46

nm, an increase of 44%. Therefore, single R6G molecule probes in PNIPAAm at 32°C explore less space and have larger jumps between confined zones than at 23°C.

While the comparison of rms displacements in Fig. 3.4 rules out the strong adsorption of probes to fixed sites within the polymer region, the polymer chains can be expected to display thermal motion of their own. Therefore, one possible explanation for the observed intermittent diffusion is the strong adsorption of probes to polymer chains and subsequent polymer motion. To test this possibility, the displacement of probes during identified ‘confined’ periods can be analyzed in light of the amount of space available to the polymer chains in the brush phase. Using the data from R6G in pNIPAAm at 23°C, the average ‘confined’ single step displacement is  $60 \pm 44$  nm for 30 ms exposure times. Based on the estimated molecular weight of pNIPAAm chains (~90 kg/mol) and the ratio of swelled thickness to collapsed thickness from hydrated ellipsometry (~1.2), the results from Yim et al.<sup>4</sup> can be used to estimate the surface density as ~0.1 chains/nm<sup>2</sup> (or 10 nm<sup>2</sup>/chain), which is within expected values for surface initiated polymer brushes described by Kim et al.<sup>52</sup> Therefore, given a maximum chain displacement of less than 10 nm and observed R6G single step displacement of 60 nm during confined periods, strong adsorption to a single polymer chain cannot explain the intermittent diffusion, especially with polymer chains that are ~140 nm long. A more likely mechanism for the observed intermittent diffusion of probe molecules within hydrated pNIPAAm is a tortuous path through the interstitial water with collisions and various interactions with polymer chains. This follows results of DSL and QENS measurements on aqueous pNIPAAm solutions by Osaka<sup>53</sup> in which interstitial hydrogen-bonded water was found to diffuse 100X faster than the polymer chains. Experiments are



underway to determine more specific physical and chemical contributions to probe confinement at  $T < T_{LCST}$  and  $T > T_{LCST}$  with series of similarly-sized dyes that shift in hydrophobic character.

### 3.4 Conclusion

A new method utilizing single molecule tracking to explore materials exhibiting temporally and spatially heterogeneous behavior has been applied to pNIPAAm, an archetypal SRM, at temperatures below and above its LCST, where it has been shown to exist in swelled and collapsed states, respectively. Several major conclusions can be drawn from a careful analysis utilizing confinement level and radius of gyration evolution to quantify the motion of R6G single molecule probes. First, probe behavior in the pNIPAAm films is best characterized by the degree of confinement that correlates with whether the film exhibits a swelled ( $T < T_{LCST}$ ) or collapsed ( $T > T_{LCST}$ ) morphology of the polymer and that behavior can be used to understand the different states of the brush. In addition, a combination of confinement level metrics, duration of confined events, and radius of confined zones - and radius of gyration evolution results can be used to illuminate the differing transport properties of hydrated pNIPAAm in swelled and collapsed states. Of particular note here is the consistent interpretation of probe motion in the collapsed state above the LCST as being confined to smaller areas, showing a higher fraction of confined segments and having a greater propensity to exhibit larger jumps between confined zones. Finally, this analysis of the non-Brownian (sub-diffusive) motion of single probe molecules serves to highlight the benefits of tracking individual molecular probes as an approach to understanding the complex dynamics of

network-based SRMs. We believe that this technique will find application to a wide range of soft materials in which nanometer-scale state changes are crucial to function, such as artificially engineered tissue, 3-D cell supports, extracellular matrix mimetics, and controlled drug delivery systems.

### 3.5 References

- (1) Urban, M. W. *Polym. Rev.* **2006**, *46*, 329.
- (2) Ahn, S. K.; Kasi, R. M.; Kim, S. C.; Sharma, N.; Zhou, Y. X. *Soft Matter* **2008**, *4*, 1151.
- (3) Stuart, M. A. C.; Huck, W. T. S.; Genzer, J.; Muller, M.; Ober, C.; Stamm, M.; Sukhorukov, G. B.; Szleifer, I.; Tsukruk, V. V.; Urban, M.; Winnik, F.; Zauscher, S.; Luzinov, I.; Minko, S. *Nat. Mater.* **2003**, *9*, 101.
- (4) Yim, H.; Kent, M. S.; Mendez, S.; Lopez, G. P.; Satija, S.; Seo, Y. *Macromolecules* **2006**, *39*, 3420.
- (5) Gil, E. S.; Hudson, S. A. *Prog. Polym. Sci.* **2004**, *29*, 1173.
- (6) *Field Responsive Polymers. Electroresponsive, Photoresponsive, and Responsive Polymers in Chemistry and Biology. ACS Symposium Series 726* Khan, I. M.; Harrison, J. S., Eds.; American Chemical Society: Washington, DC, 2000; Vol. 122.
- (7) Gehrke, S. H. *Adv. Polym. Sci.* **1993**, *110*, 81.
- (8) Pelton, R. H.; Chibante, P. *Colloids and Surfaces* **1986**, *20*, 247.
- (9) Kaholek, M.; Lee, W. K.; Ahn, S. J.; Ma, H. W.; Caster, K. C.; LaMattina, B.; Zauscher, S. *Chem. Mater.* **2004**, *16*, 3688.
- (10) Chaterji, S.; Kwon, I. K.; Park, K. *Prog. Polym. Sci.* **2007**, *32*, 1083.
- (11) Kusumi, A.; Sako, Y.; Yamamoto, M. *Biophys. J.* **1993**, *65*, 2021.
- (12) Ishihara, A.; Jacobson, K. *Biophys. J.* **1993**, *65*, 1754.
- (13) Ghosh, R. N.; Webb, W. W. *Biophys. J.* **1994**, *66*, 1301.

- (14) Kubitscheck, U.; Wedekind, P.; Peters, R. *Biophys. J.* **1994**, *67*, 948.
- (15) Saxton, M. J. *Biophys. J.* **1995**, *69*, 389.
- (16) Cherry, R. J.; Wilson, K. M.; Triantafilou, K.; O'Toole, P.; Morrison, I. E. G.; Smith, P. R.; Fernandez, N. *J. Cell Biol.* **1998**, *140*, 71.
- (17) Simson, R.; Sheets, E. D.; Jacobson, K. *Biophys. J.* **1995**, *69*, 989.
- (18) Crocker, J. C.; Grier, D. G. *J. Colloid Interface Sci.* **1996**, *179*, 298.
- (19) Ito, S.; Kusumi, T.; Takeiac, S.; Miyasaka, H. *Chem. Commun.* **2009**, *41*, 6165.
- (20) McCain, K. S.; Hanley, D. C.; Harris, J. M. *Anal. Chem.* **2003**, *75*, 4351.
- (21) Saxton, M. J.; Jacobson, K. *Annu. Rev. Biophys. Biomol. Struct.* **1997**, *26*, 373.
- (22) Honciuc, A.; Schwartz, D. K. *J. Am. Chem. Soc.* **2009**, *131*, 5973.
- (23) Dickson, R. M.; Norris, D. J.; Tzeng, Y. L.; Moerner, W. E. *Science* **1996**, *274*, 966.
- (24) Wang, S. Q.; Zhu, Y. X. *Soft Matter*, *6*, 4661.
- (25) Lokuge, I.; Wang, X.; Bohn, P. W. *Langmuir* **2007**, *23*, 305.
- (26) Elliott, L. C. C.; Barhoum, M.; Harris, J. M.; Bohn, P. W. *PCCP* **2011**, *13*, 4326.
- (27) Tompkins, H. G. *A User's Guide to Ellipsometry*; Academic Press, Inc.: San Diego, CA,, 1993.
- (28) Tompkins, H. G. *Handbook of Ellipsometry*; William Andrew Publishing: Norwich, NY, 2005.
- (29) Fox, C. B.; Myers, G. A.; Harris, J. M. *Appl. Spectrosc.* **2007**, *61*, 465.
- (30) Anthony, S.; Zhang, L.; Granick, S. *Langmuir* **2006**, *22*, 5266.
- (31) Anthony, S. M.; Granick, S. *Langmuir* **2009**, *25*, 8152.
- (32) Weeks, E. R.; Crocker, J. C.; Levitt, A. C.; Schofield, A.; Weitz, D. A. *Science* **2000**, *287*, 627.

- (33) Qu, X.; Wu, D.; Mets, L.; Scherer, N. F. *PNAS* **2004**, *101*, 11298.
- (34) Ritchie, K.; Shan, X. Y.; Kondo, J.; Iwasawa, K.; Fujiwara, T.; Kusumi, A. *Biophys. J.* **2005**, *88*, 2266.
- (35) van Dijk, M. A.; Kapitein, L. C.; van Mameren, J.; Schmidt, C. F.; Peterman, E. J. G. *J. Phys. Chem. B* **2004**, *108*, 6479.
- (36) Serge, A.; Bertaux, N.; Rigneault, H.; Marguet, D. *Nat. Methods* **2008**, *5*, 687.
- (37) Barbey, R.; Lavanant, L.; Paripovic, D.; Schuwer, N.; Sugnaux, C.; Tugulu, S.; Klok, H. A. *Chem. Rev.* **2009**, *109*, 5437.
- (38) Balamurugan, S.; Mendez, S.; Balamurugan, S. S.; O'Brien, M. J.; Lopez, G. P. *Langmuir* **2003**, *19*, 2545.
- (39) He, Q.; Kuller, A.; Grunze, M.; Li, J. B. *Langmuir* **2007**, *23*, 3981.
- (40) Sun, T. L.; Wang, G. J.; Feng, L.; Liu, B. Q.; Ma, Y. M.; Jiang, L.; Zhu, D. B. *Angew. Chem.-Int. Edit.* **2004**, *43*, 357.
- (41) Annaka, M.; Yahiro, C.; Nagase, K.; Kikuchi, A.; Okano, T. *Polymer* **2007**, *48*, 5713.
- (42) Ishida, N.; Biggs, S. *Macromolecules* **2010**, *43*, 7269.
- (43) Kurz, V.; Grunze, M.; Koelsch, P. *Chemphyschem* **2010**, *11*, 1425.
- (44) Malham, I. B.; Bureau, L. *Langmuir* **2009**, *26*, 4762.
- (45) Wei, Q. S.; Ji, J.; Shen, J. C. *Macromol. Rapid Commun.* **2008**, *29*, 645.
- (46) Vidyasagar, A.; Majewski, J.; Toomey, R. *Macromolecules* **2008**, *41*, 919.
- (47) Yin, Z. Z.; Zhang, J. J.; Jiang, L. P.; Zhu, J. J. *J. Phys. Chem. C* **2009**, *113*, 16104.
- (48) Tu, H.; Heitzman, C. E.; Braun, P. V. *Langmuir* **2004**, *20*, 8313.
- (49) Deschenes, L. A.; Bout, D. A. V. *Chem. Phys. Lett.* **2002**, *365*, 387.
- (50) Schuster, J.; Brabandt, J.; von Borczyskowski, C. *J. Lumin.* **2007**, *127*, 224.

- (51) de Keijzer, S.; Serge, A.; van Hemert, F.; Lommerse, P. H. M.; Lamers, G. E. M.; Spaik, H. P.; Schmidt, T.; Snaar-Jagalska, B. E. *J. Cell Sci.* **2008**, *121*, 1750.
- (52) Kim, J. B.; Bruening, M. L.; Baker, G. L. *J. Am. Chem. Soc.* **2000**, *122*, 7616.
- (53) Osaka, N.; Shibayama, M.; Kikuchi, T.; Yamamuro, O. *J. Phys. Chem. B* **2009**, *113*, 12870.

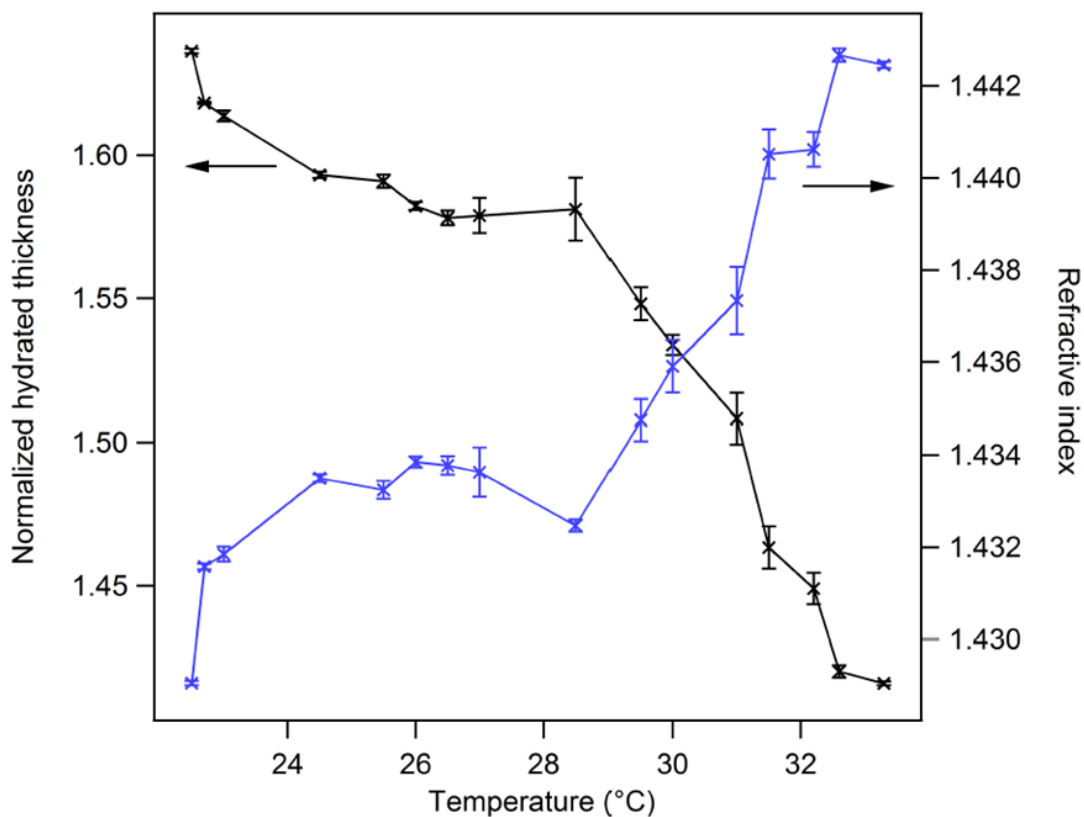


**Figure 3.1.** Ellipsometric measurements of thickness normalized to dry thickness (black) and refractive index (blue) as a function of temperature for hydrated pNIPAAm synthesized on Si. Films displayed 45 nm dry thickness. All films exhibited a ~165% increase from dry to expanded and an 85% decrease from expanded to collapsed hydrated states, which corresponds to single spot measurements on a 80 nm dry sample (not reported). At each temperature, measurements were averaged over at least 10 spots with the standard deviations reported as error bars.

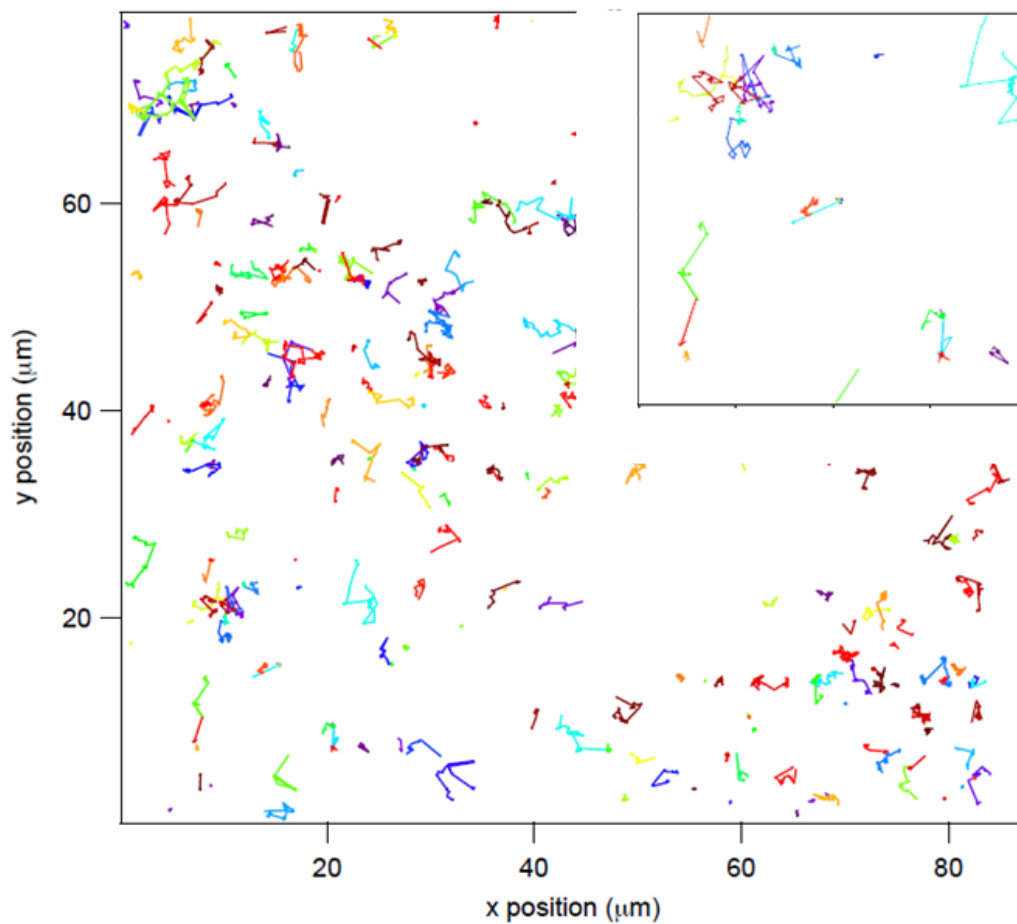


**Figure 3.2** Reconstructed SMT trajectories longer than 50 frames for R6G in pNIPAAm on glass at 23°C (polymer brush in expanded state); (*Inset*) 20  $\mu\text{m}$  x 20  $\mu\text{m}$  expanded view. Different colors represent different trajectories, which may appear to overlap but in fact occur at different times.

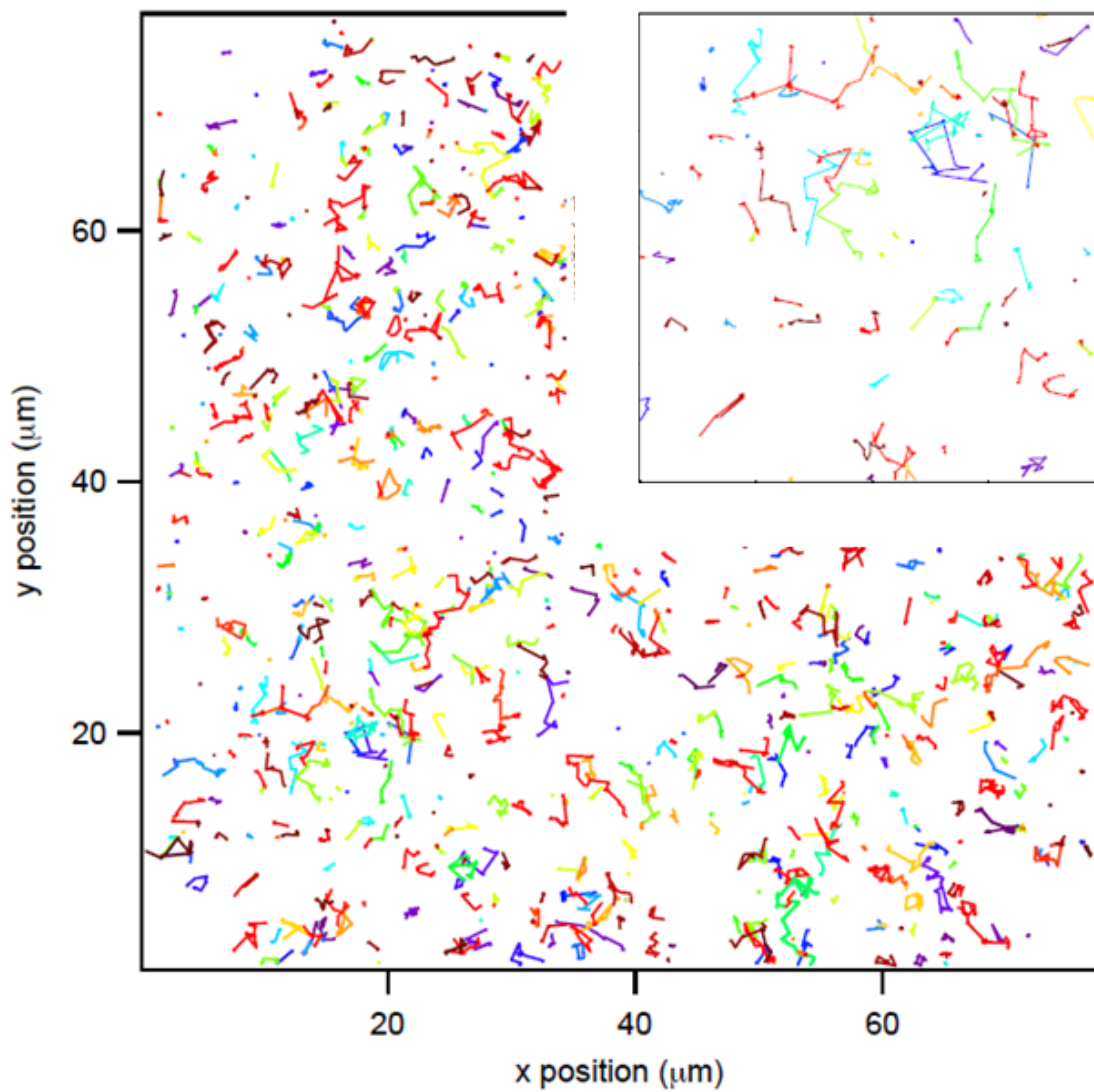


**Figure 3.3** Reconstructed SMT trajectories longer than 50 frames for R6G in pNIPAAm on glass at 32°C (polymer brush in collapsed state); (*Inset*) 20  $\mu\text{m}$  x 20  $\mu\text{m}$  expanded view. Different colors represent different trajectories, which may appear to overlap but in fact occur at different times.



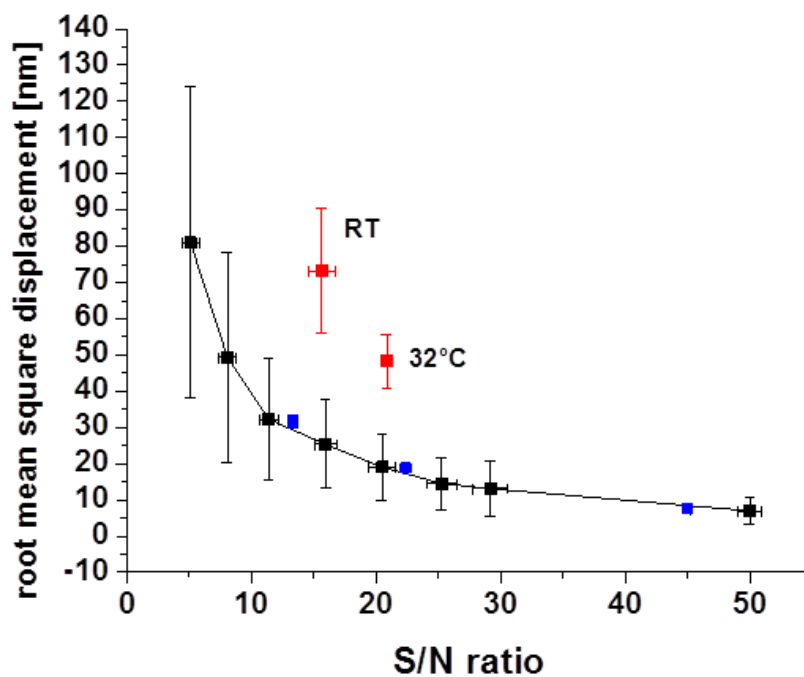


**Figure 3.4.** Root mean square displacement (for 30 ms exposure) for R6G molecules adsorbed to a surface site as a function of the S/N ratio of the single molecule fluorescent image for both simulated (black) and experimental (blue) data. Red squares correspond to the experimentally determined rms displacement and S/N for confined R6G molecules in pNIPAAm both below and above the LCST, as noted. Error bars shown for rms and S/N for all points are the standard error of the mean.

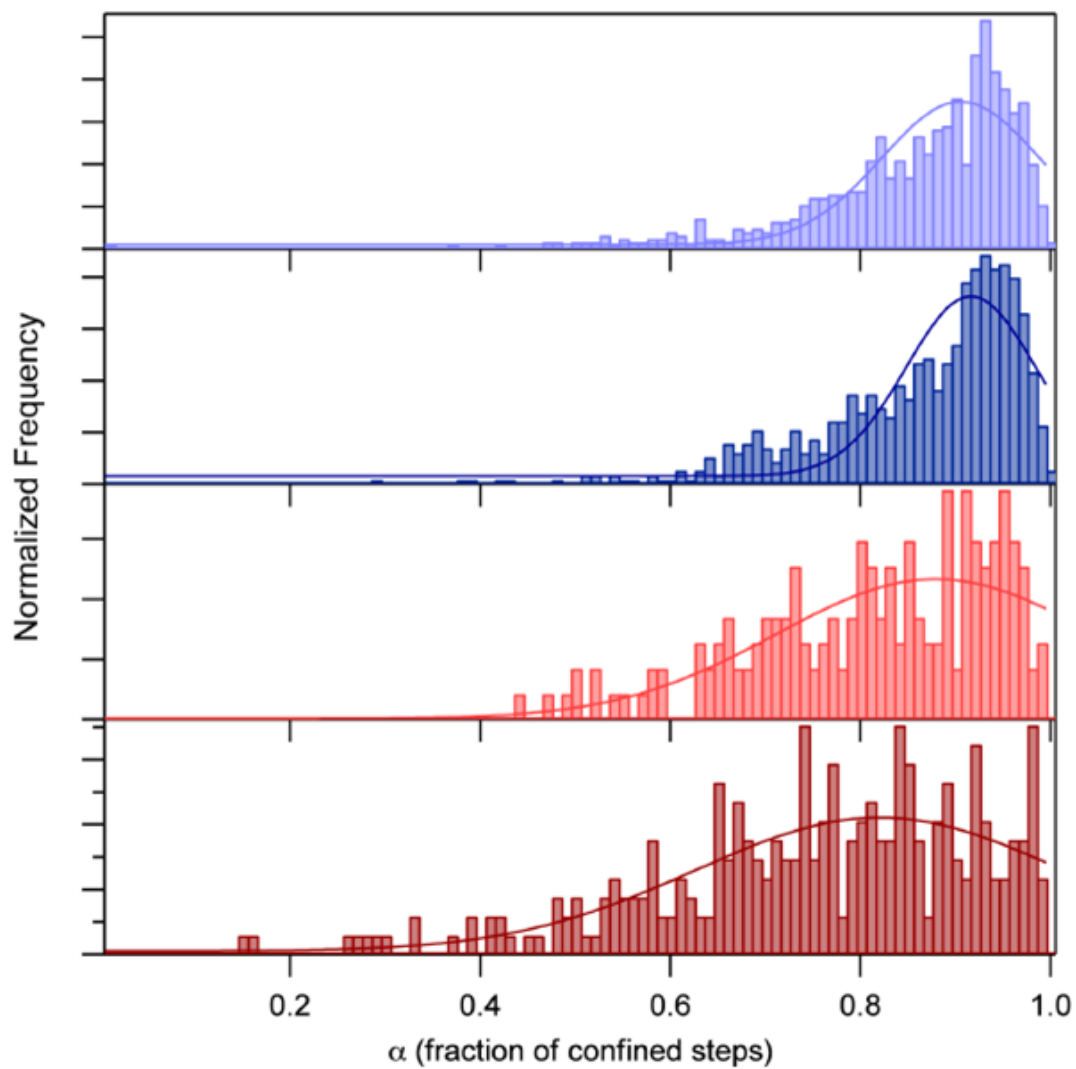


**Figure 3.5** Confinement level analysis results for two separate samples of R6G probes in the same pNIPAAm sample on glass at 23°C (dark red, light red) and 32°C (dark blue, light blue).

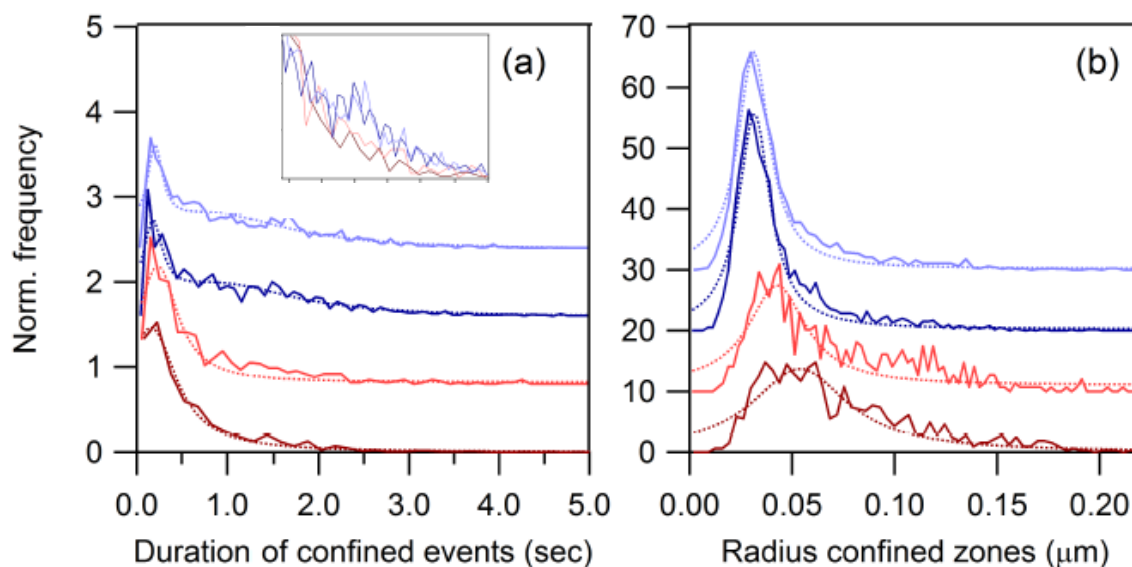


**Figure 3.6.** Confinement level analysis for R6G in pNIPAAm at 23°C (dark red, light red) and 32°C (dark blue, light blue), two trials each. Traces are offset for clarity and the inset emphasizes the difference between the tail at 23°C and 32°C. (a) Normalized histograms of the duration of confined events, with fits (dashed lines) for single (23°C) and double (32°C) Lorentzian functions. (b) Distribution of the radius of confined zones.

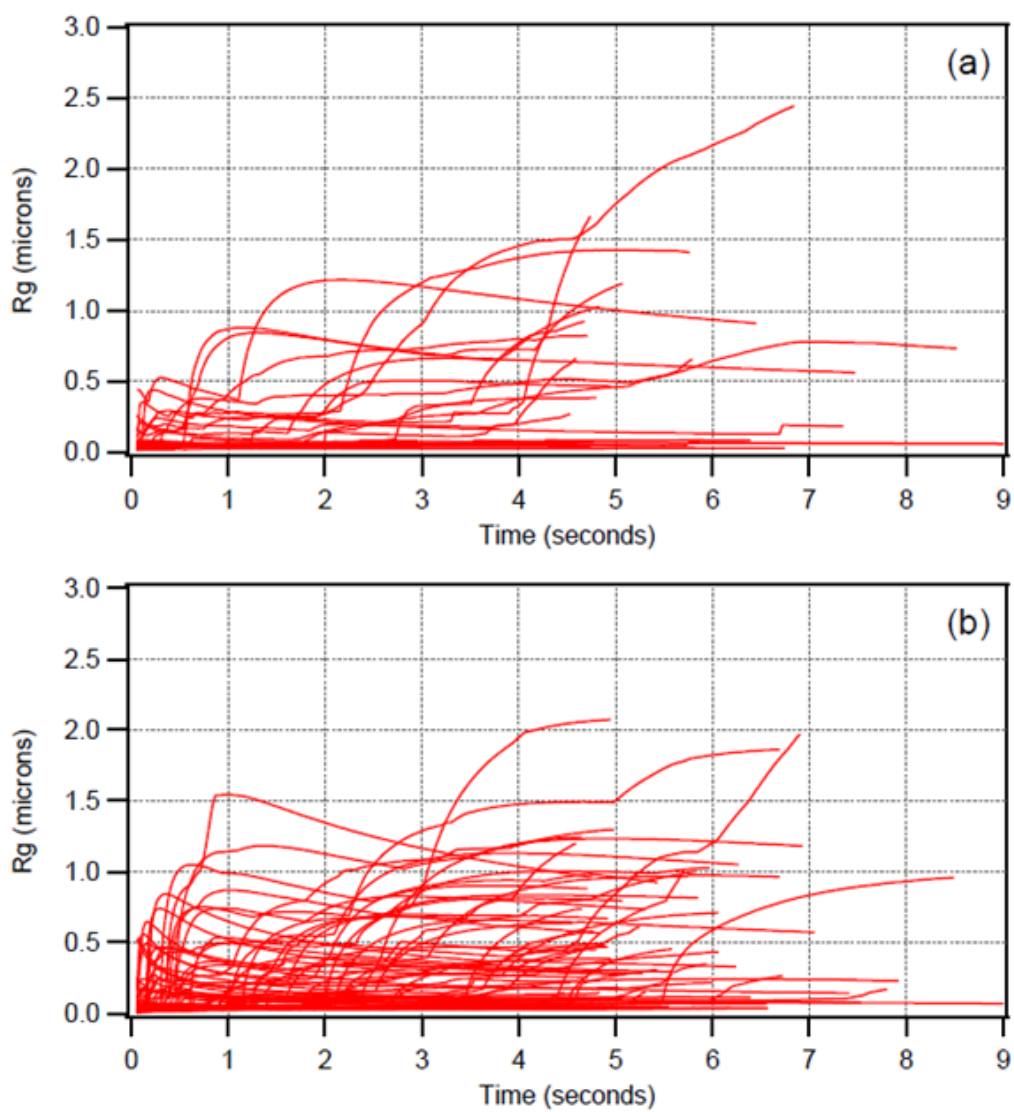


**Figure 3.7** Radius of gyration evolution for trajectories at 23°C (a) and 32°C (b) of R6G in pNIPAAm on glass. Only trajectories longer than 150 steps are included.

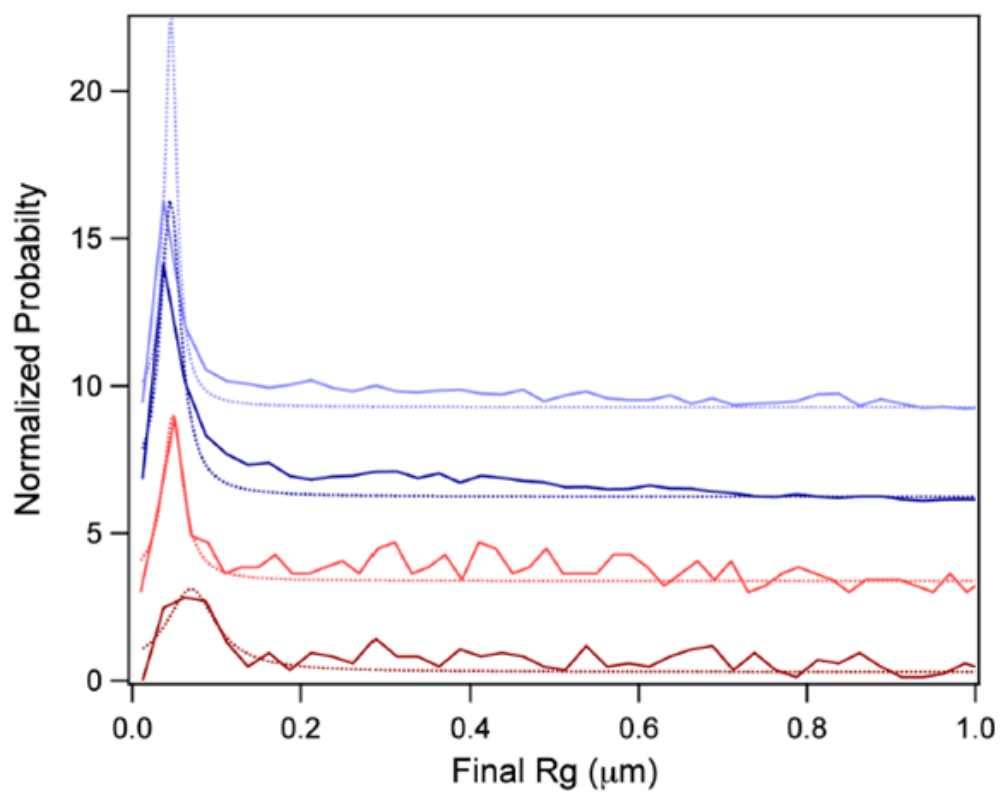


**Figure 3.8.** Histograms of the final  $R_g$  value for each molecule in SMT movies 23°C (dark and light red) and 32°C (dark and light blue).

## CHAPTER 4

### RAPID SOL-GEL FABRICATION OF HIGH-QUALITY THIN-FILM STACKS ON PLANAR AND CURVED SUBSTRATES

Adapted with permission from: Moussa Barhoum, Jacob Morrill, David Riassetto, and Michael H. Bartl, *Rapid Sol-Gel Fabrication of High-Quality Thin-Film Stacks on Planar and Curved Substrates*, Chem.Mater., **2011**, 23(23), pp5177-5184, American Chemical Society

#### 4.1 Introduction

Sol-gel chemistry has emerged as an attractive—simple, rapid and inexpensive—alternative synthesis route to physical and chemical deposition methods.<sup>1-6</sup> The relatively mild synthesis conditions and flexibility of sol-gel chemistry have opened the door to a large variety of compounds that can be processed into thin films, fibers, and monoliths. In addition, when combined with molecular and/or colloidal assembly methods, it is possible to create composites with internal three-dimensional meso-to-macroscale periodic features and other hierarchical structures.<sup>4-12</sup> This large diversity of accessible compositions, morphologies and internal structures makes sol-gel chemistry-derived materials attractive candidates for numerous applications ranging from catalysis, separation and sorption to uses in electronics and photonics.<sup>4-6,13-18</sup>

A remaining challenge for widespread commercial applications is to produce sol-gel-derived materials with structural uniformity over large sample areas ( $> \text{cm}^2$ ) and controlled batch-to-batch reproducibility. This is particularly true for thin-film based materials and applications. Here, the level of uniformity and control over thin-film parameters has been set very high by physical and chemical deposition methods, such as atomic layer deposition,<sup>19,20</sup> chemical vapor deposition,<sup>21,22</sup> molecular beam epitaxy,<sup>23</sup> and various sputtering techniques.<sup>24-26</sup> Therefore, for sol-gel processing to be considered a viable fabrication alternative for commercial applications, similar standards have to be achieved. The two foremost challenges in sol-gel fabrication of thin films are the avoidance of crack formation and the achievement of a uniform and reproducible film thickness over large areas. Both of these problems are directly related to solvent evaporation during deposition of thin films (dip or spin coating, casting) and their densification in subsequent heat treatments (calcination, annealing).<sup>5,27,28</sup> Conducting the thin film deposition process under controlled environmental conditions (for example, a dedicated clean room with controlled humidity, temperature, substrate pretreatment, absence of dust particles in air) can help to significantly increase the film quality. However, despite these advances, sol-gel derived thin films are still prone to irregularities in film thickness (edge effects), and shrinkage and crack-formation during heat treatment.

Among the large family of interesting thin film compounds the wide bandgap semiconductor titania has recently gained tremendous attention due to its outstanding chemical and physical properties. While high chemical stability and catalytic activity make titania a prime candidate for photoanodes in solar cells<sup>29</sup> and water-splitting,<sup>30,31</sup> its high refractive index combined with optical transparency in the visible range of the

electromagnetic spectrum are ideal for producing reflective coatings<sup>32</sup> and other optical components.<sup>33</sup> Furthermore, by depositing titania thin films alternately in stack-form with a lower refractive index compound such as silica, interesting one-dimensional (1D) photonic bandgap materials can be fabricated, including reflectors, filters, and microcavities.<sup>34-36</sup> Such layering of thin films of different compounds with different thermal expansion coefficients, however, poses a big challenge for sol-gel fabrication. During film processing and thermal treatments, different shrinkage properties within alternating layers and at interfaces induces stresses and can lead to severe crack formation, delamination, and variation in the film thicknesses.

A strategy for minimizing crack formation in titania/silica thin-film stacks is the firing process.<sup>28,37</sup> This is an additional short heat-treatment step at high temperatures (900-1000 °C). The purpose of this firing process is to take advantage of the opposing thin film stresses for silica and titania at 900 °C. While, studies by Rabaste et al.<sup>37</sup> and Kozuka et al.<sup>28</sup> revealed an induced tensile stress for both silica and titania thin films up to 800 °C, increasing the temperature to 900 °C resulted in a compressive stress for silica. It is argued that these opposing stresses result in an overall relaxed multistack and reduces the formation of cracks. Contrasting this high-temperature approach, Keszler et al. reported a low-temperature (5 °C) solution-processing method followed by an annealing step at modest temperatures (300°C).<sup>38</sup> This method allows for the deposition of dense titania thin films. However, in this method the deposition thickness is limited to ~18 nm for each deposition cycle. To create alternating stack structures with each layer having a thickness of several tens to hundreds of nanometer thickness (as required for application as photonic band gap materials operating in the visible or near infrared



range), this method would require deposition of multiple consecutive films of the same compound.

In this paper, we describe an alternative sol-gel approach for the rapid fabrication of high quality silica and titania thin films and alternating silica/titania stack structures. Our method allows deposition of these thin film and multilayer structures on planar and curved structures without loss of film quality. Regardless of stack structure, layer numbers and type of substrate, the materials fabricated by our method have predictable uniform thickness and are crack-free over large areas. The versatility of our sol-gel method is demonstrated by engineering different 1D photonic bandgap materials on planar and curved substrates, including high quality Bragg reflectors and filters, Fabry-Perot microcavities, and asymmetric stacks. We show that the photonic properties of these structures can be readily tuned by controlling the thickness and sequence of the deposited films as well as by tailoring the refractive indices of individual layers through the introduction of nanoporosity. We will discuss the essential steps of our sol-gel deposition and processing method and introduce several new process parameters found to be critical for successfully producing crack-free multilayer structures with uniform thickness. These parameters include controlled solvent evaporation during and after the film deposition and a shock-cooling step immediately following the thermal annealing process at 350-500 °C. The fabrication steps and the final samples were characterized by scanning electron microscopy (SEM), transmission electron microscopy (TEM), variable-angle ellipsometry measurements, X-ray diffraction (XRD), and optical reflection spectroscopy. The measured optical reflection spectra are further compared to simulated spectra using the transfer-matrix method.<sup>39</sup>

## 4.2 Experimental Section

### 4.2.1 Preparation of precursor solutions

The titania precursor solution was prepared by mixing 60 mL titanium(IV)isopropoxide (98%, Acros) and 65 mL ethanol under vigorous stirring for 30 minutes (exothermic reaction). A solution of 124 mL ethanol, 0.6 mL hydrochloric acid (12 M) and 1.15 mL of 18 $\Omega$  deionized water (DI water) was then added to the titania solution and stirred for an additional 30 minutes. This titania precursor solution (titania stock solution) with a molar ratio of 1:16.15:0.42:0.097 titanium(IV)isopropoxide:EtOH:H<sub>2</sub>O:HCl was aged for at least 48 hours at room temperature before further use. The silica precursor solution was prepared by adding 105 mL tetraethylorthosilicate (Aldrich) to a mixture of 12.3 mL DI water, 76 mL ethanol and 6.3 mL HCl (0.01 M) and mixing for 30 minutes at room temperature. This silica precursor solution (silica stock solution) with a molar ratio of 1:2.77:1.92:0.004 tetraethylorthosilicate:EtOH:H<sub>2</sub>O:HCl was aged for at least 48 hours at 60 °C before further use. Both the titania and the silica precursor solutions are stable for at least one week when stored in the dark.

### 4.2.2 Deposition of thin-film single and multilayer structures

Figure 4.1 illustrates the four-step thin-film deposition cycle. Thin films were deposited by dip-coating precursor solutions onto cleaned substrates. Cleaning was done by rinsing with isopropanol and drying in a stream of nitrogen. Substrates were immersed into the sol (titania or silica precursor solution) and vertically withdrawn at a constant speed of 12.5 cm/minute (step 1). The dip-coating process was immediately followed by heating the deposited film in a flowing stream of hot air (100-200 °C; produced by a heat

gun) for rapid evaporation of volatile solvents (step 2). The dried films were further heat-treated (calcined) for 1 minute at 350-500 °C in a muffle furnace (step 3). The final step of the thin-film deposition cycle was a shock-cooling procedure (step 4). This was accomplished by taking the sample out of the hot furnace and either placing it onto a Pyrex glass substrate at room temperature or dipping it into a water/isopropanol mixture. The selection of the cooling method depends on the geometry of the substrate and the heat transfer ratio between the substrate and the heat sink. While the former method was sufficient to promote rapid cooling for thin films deposited onto thin silicon wafer substrates, the latter method was necessary for curved substrates and substrates made of thick silicon wafers and quartz or glass slides. Titania or silica single-compound multilayers and alternating titania/silica multilayer stacks were prepared by repeating this cycle using the appropriate sols at each cycle. A final heat-treatment of the multilayer structures at 400-500 °C for 1 hour concluded the deposition process.

#### 4.2.3 Fabrication of Bragg stacks and Fabry-Perot microcavities

Bragg stacks (reflectors, filters) were fabricated by deposition of at least 6 alternating silica/titania double-layers (12 layers in total). The thickness of each layer was controlled by either diluting the precursor solutions with additional ethanol or by varying the dip-coating speed, allowing for tuning the optical band gap in the visible range as discussed further in the Results and Discussion section. For example, to fabricate a silica layer with a thickness of  $88 \pm 2$  nm the original silica stock solution was diluted down to 25 volume percent of its original volume. The fabrication of  $80 \pm 2$  nm titania layer requires a 20 volume percent dilution of the stock solution with ethanol. This relationship

of film thickness and degree of dilution of the precursor solutions is also depicted in Figure 4.4. Fabry-Perot optical microcavities were fabricated by breaking the symmetry of a Bragg stack, i.e., introduction of a defect layer. This was accomplished by subsequently depositing two layers of the same compound. The wavelength position and quality of the microcavity mode was tuned by adjusting the thickness and dielectric properties of the defect layer with respect to the multilayer stack.

#### 4.2.4 Refractive index tuning

The effective film refractive index was tuned by introducing a certain degree of nanoporosity into a deposited dielectric layer. This was achieved by dissolving various amounts of the block copolymer surfactant Pluronic P123 in the sol prior to dip-coating.<sup>6,40</sup> For example, to lower the refractive index of a titania layer, between 0.1 and 0.5 g of P123 were dissolved in the titania precursor solution (described above). To compensate for changes of the solution viscosity due to the addition of surfactants, the dip-coating speed was adjusted to keep the thickness of the deposited layers constant. Heat-treatment of the samples caused the pyrolytic removal of the surfactant molecules and formation of a disordered nanoporous framework. This framework was then infiltrated during the succeeding deposition cycle by the alternating precursor solution (e.g., silica), resulting in a lowered effective refractive index from pure titania to that of a titania/silica composite.

#### 4.2.5 Characterization studies

The film crystallinity was determined by a Bruker D8 Advanced X-Ray Diffractometer (Cu-K $\alpha$  radiation). The refractive index and thickness of thin films were measured with a Woolam Variable Angle Spectroscopic Ellipsometer. SEM studies were conducted on a FEI NovaNano (FEG-SEM630) microscope and a FEI NovaNano (FEI DB237) focused ion beam microscope. TEM imaging was done on a FEI Tecnai F30 microscope at 300 kV acceleration voltage. Sample preparation for TEM measurements involved scratching off the deposited thin film from the Si-wafer substrate with a sharp razor blade. The sample was then suspended in ethanol and dispersed onto a copper TEM sample holder. Sample preparation for SEM measurements involved splitting the thin film substrate perpendicular to the deposited thin film stack and mounting the exposed cross section of the sample on a vertical SEM specimen stub. If necessary the mounted specimen was coated with a thin layer of gold to minimize charging effects during SEM studies.

#### 4.2.6 Optical reflection microscopy and spectroscopy

Optical reflection spectra were measured with a modified optical microscope (Nikon ME600). The output of a broadband white light source was focused onto the sample surface by a 20x objective (0.45 NA). The reflected light was collected by the same objective and either imaged by a CCD camera or fiber-coupled into an Ocean Optics USB-4000 UV-VIS spectrometer. A broadband mirror ( $R > 0.96$ ) was used as reference.

#### 4.2.7 Simulation of optical reflection spectra

Optical reflection spectra were simulated by the transfer-matrix method using OpenFilters.<sup>41</sup> OpenFilters is an open-source software with a built-in graphical interface and is available at no charge under the GNU General Public License.

### 4.3 Results and Discussion

#### 4.3.1 Single and multilayer sol-gel dip-coating process

The dominating challenge in fabricating high-quality thin film single and multilayer structures is the suppression of crack formation. Crack formation is the result of stresses occurring during and after the deposition process that exceed the thin film strength.<sup>1,42,43</sup> For inorganic thin films derived by sol-gel chemistry cracks can form at multiple processing stages. We designed a sol-gel dip-coating method optimized to address these challenges at the three most important processing stages: the initial film drying, the preannealing step, and the annealing (heat treatment) process. The major steps of our process for fabricating highly reproducible, large-area, crack-free single and multilayer structures of silica and titania, as well as stacks of alternating layers of these two compounds, are schematically shown in Figure 4.1.

During the drainage process which starts immediately after the film withdrawal in the dip-coating process, inhomogeneous solvent evaporation within the film creates a pressure gradient.<sup>27,44</sup> The gradient causes a differential shrinkage of the thin-film network, whereby the exterior of the network shrinks faster than the interior. This leads to the built-up of tensile stresses that can fracture the thin-film upon ongoing solvent evaporation.<sup>1</sup> We found this problem can be overcome by designing the dip-coating

process such that the freshly deposited film is withdrawn into an environment of high solution-vapor pressure. This is achieved simply by using a tall vial that was only half-filled with the deposition solution (Figure 4.1a). The deposited film is subsequently subjected to a drying step in a flowing hot-air stream generated by a heat gun (Figure 4.1b), resulting in a rapid and homogeneous solvent evaporation. We found the combination of these two steps counteracts the differential shrinkage within the deposited layer and results in formation of crack-free films (Figures 4.2a, b). In addition, the heat-gun treatment greatly reduced the occurrence of edge effects. Edge effects in deposited thin films are a known phenomenon especially associated with dip-coating processes, and are caused by substrate vibrations and inhomogeneous solvent evaporation in the center and at the edges of deposited films during the withdrawal process.<sup>45</sup>

Heat-treatment of the deposited films is the final stage of the fabrication process. During heat-treatment residual solvent and other organic components of the precursor solution are pyrolytically removed and the loosely formed oxide network is further densified. In the case of titania films, heat-treatment also leads to partial crystallization of the initially amorphous network. However, these reactions during heat-treatment also lead to further film shrinkage, accompanied by an increase in tensile stresses, potentially causing crack formation. On the other hand, it is known that rapid heating rates increase the viscoelasticity of the initially forming amorphous oxide network.<sup>28,42,43</sup> This network relaxation counteracts the tensile stress formation and suppresses crack formation. We found placing the deposited and hot-air treated films into a preheated oven at 350-500 °C for 1 minute gave the best results (Figure 4.1c).

Similar to the heating process the cool-down stage must be optimized to create high quality films. While this stage of the heat-treatment is often neglected, we found it to be of particular importance for fabricating crack-free thin-film stacks composed of alternating layers of silica and titania. Several factors are responsible for the formation of cracks during the cool-down process. One source is the difference in expansion coefficients between the alternating deposited layers as well as between the substrate and the deposited film. Another source of cracking is reorganization of the thin film metal oxide network. This reorganization is caused by phase transitions of the amorphous or amorphous/polycrystalline network upon cooling, leading to built-up of stresses that can fracture the film network.<sup>28</sup> We studied the cool-down process in detail and found that—similar to the heating stage—rapid cooling rates are beneficial in the prevention of crack formation (Figures 4.2c, d). While perhaps counterintuitive, we found the best results were obtained by shock-cooling the film samples to room temperature immediately following the 1-minute heating period. Shock-cooling was achieved by placing the hot samples onto a Pyrex glass substrate at room temperature or immersing them into a water/isopropanol mixture (Figure 4.1d). While the exact mechanism is still under investigation, we propose rapid cooling minimizes the occurrence of interfacial stresses (due the difference in thermal expansion coefficients of alternating layers). In addition, temperature quenching freezes high-temperature amorphous/polycrystalline phases,<sup>46</sup> maintaining high viscoelasticity of the oxide network at room temperature.



### 4.3.2 Deposition of Bragg stacks on various substrates

To demonstrate the effectiveness of our sol-gel process in fabricating high-quality multilayer structures we fabricated a Bragg stack of seven alternating silica/titania layers (14 layers in total). The Bragg stack was fabricated on a silicon wafer (100) substrate using the thin film deposition cycle described above (Figure 4.3a). The deposition parameters were tuned to yield layer thicknesses of  $88\pm 2$  nm (silica) and  $75\pm 2$  nm (titania) after calcination at 500 °C. At this temperature the titania network predominantly forms an anatase polycrystalline phase,<sup>47,48</sup> as was confirmed by XRD measurements. The structural features of the Bragg stack were examined by optical and electron microscopy. Optical imaging revealed a smooth surface and absence of even micro-cracks, and cross-sectional SEM imaging verified the high degree of thickness uniformity throughout the multilayer stack (Figure 4.3b). It should be emphasized that this deposition process is capable of producing uniform multilayer stacks over large areas. For example, Figure 4.10 shows a Bragg stack of six alternating silica/titania layers (12 layers in total) deposited over an area of 20 cm<sup>2</sup>.

The excellent structural uniformity is also reflected in the optical properties of the Bragg stacks, acting as 1D photonic band gap materials. As expected for a high-quality 1D photonic band gap structure, our 14-layer sample displayed an optical reflection peak with a broad wavelength range of 100 percent reflectivity (Figures 4.3c). In general, we found six to seven alternating double-layers are necessary to achieve a band gap with 100 percent reflectivity in the visible range of the electromagnetic spectrum. For the 88/75 nm silica/titania Bragg stack we measured a broad reflection band centered at a wavelength position of 575 nm and a width of  $6200\text{ cm}^{-1}$  (around 200 nm) at normal incidence. The

reproducibility of our deposition process was confirmed by fabricating three samples at different times but under the same experimental conditions (i.e., precursor solution composition, dip-coating parameters, drying and heat treatments). The optical reflection properties of the three samples are given in Figure 4.11 and show near-identical optical features in terms of reflection band position, width and shape (including side bands). Importantly, the measured reflection data are in excellent agreement with the calculated reflection spectrum (dotted line in Figure 4.3c). For the calculation we used the film thickness (SEM imaging), the number of layers, and the refractive index of each layer (determined by ellipsometry) as input parameters.

It should be emphasized that our sol-gel deposition method can be applied to a number of different substrates. For example, to produce optical filters we used quartz or borosilicate glass substrates (Figure 4.4a). Optical characterization reveals almost identical reflection features, confirming the high optical quality of the samples regardless of the substrate (Figure 4.4c). Note that borosilicate substrates, for example, would be incompatible with often-used high-temperature (900-1000 °C) firing methods. The versatility of our sol-gel method is further demonstrated by depositing the same Bragg stacks onto curved quartz and glass substrates. As shown in Figures 4.4b and 4.4d, also samples deposited onto curved substrates show excellent optical properties and are interesting candidates for parabolic high-power laser mirrors and solar radiation collectors. For all samples, the calculated reflection spectra are also included (dotted lines), demonstrating again the good optical performance of the Bragg stacks regardless of the substrates used.

### 4.3.3 Tuning the position and width of the photonic band gap

Since Bragg stacks behave as 1D photonic bandgap materials, the width and the position of the optical reflection band (bandgap) can be tuned by adjusting the refractive index difference and the thickness, respectively, of the alternating layers.<sup>49,50</sup> The ability to tune the band gap position is demonstrated in Figure 4.5. Varying the lattice constant (one silica/titania double-layer) from  $148\pm 2$  nm to  $168\pm 2$  nm (in 5 nm steps) shifts the reflection band throughout the entire visible range. The lattice constant variation was achieved by adjusting the titania layer thickness for each sample while keeping the silica layer thickness constant at  $88\pm 2$  nm. Experimentally, this was done simply by diluting the titania precursor solution with additional ethanol while keeping the silica precursor concentration and the dip-coating parameters constant. The degree of dissolution was adjusted in response to ellipsometry measurements and SEM cross-sectional imaging (see also Figure 4.9). Additionally, simulations were used to verify the experimentally obtained reflection band positions and other optical features. Again, as shown by the dotted spectra in Figure 4.5, excellent agreement was achieved.

The width of the photonic bandgap can be tuned by modifying the difference in the refractive indices of the alternating layer; in general, the smaller the difference the narrower the gap. While the refractive indices of titania and silica obtained by our sol-gel method are fixed ( $2.34\pm 0.02$  for titania and  $1.48\pm 0.02$  for silica), we found that tuning the difference is possible by fabricating composite layers. For example, diluting the titania layers with a given amount of silica lowers the effective refractive index from 2.34 to a value given by the silica volume fraction (dilution factor). Building a Bragg stack with

silica-diluted titania layers while leaving the silica layers unchanged thus reduces the refractive index difference and should narrow the bandgap.

Diluting the titania layers was achieved by first adding a block copolymer surfactant (Pluronic P123) to the titania precursor solution.<sup>6,40</sup> After film dip-coating the organic surfactant is thermally removed during the heat-treatment, leaving behind a disordered nanoporous titania framework. A TEM image of a titania film deposited from a precursor solution containing 0.5 g P123 is shown in Figure 4.6a and reveals the nanoscale porosity. During the following dip-coating step of a layer of silica the porous titania framework also is infiltrated with the silica precursor solution. Since the degree of silica-dilution is given by the degree of porosity of the titania layer, it can readily be tuned by the amount of P123 mixed into the titania precursor solution. For example, addition of 0.3 g and 0.5 g of P123 resulted in silica-titania composite layers with refractive indices of  $2.1\pm 0.1$  and  $1.8\pm 0.1$ , respectively. These values were obtained by fitting the measured optical reflectance data to simulated spectra of Bragg stacks with known lattice constants and layer thicknesses (measured by SEM imaging). Figure 4.6b illustrates the tunability of the reflection bandwidth (photonic bandgap) for three Bragg stacks with decreasing refractive index differences between the alternating layers.

#### 4.3.4 Design of optical microcavities and asymmetric stacks

The simplicity and flexibility of our sol-gel dip-coating route readily allows the creation of multilayer structures with built-in asymmetry. For example, Figure 4.7a shows a cross-section SEM image of a multilayer stack with a central defect layer breaking the symmetry of the periodic stack. The overall structure consists of a central

silica layer with a thickness of  $176\pm 2$  nm sandwiched between two Bragg stacks each composed of four silica/titania double layers with a lattice constant of  $158\pm 2$  nm and individual layer thicknesses of  $88\pm 2$  nm (silica) and  $70\pm 2$  nm (titania). The 176 nm silica layer was fabricated simply by dip-coating two successive 88 nm silica layers. The optical reflection spectrum of the final structure is given in Figure 4.7b and displays the typical characteristic of a Fabry-Perot microcavity, namely, a narrow high-transmittance region (localized optical mode) within the optical reflection band (photonic band gap). The transmission peak maximum (70 percent transmittance) is located at a wavelength position of 568 nm and has a full-width-half-maximum value,  $\Delta\lambda$ , of 5 nm for normal incidence of unpolarized light. This yields a quality factor,  $Q = \Delta\lambda/\lambda$ , of 112 for the microcavity. Similar to tuning the optical properties of Bragg stacks, the wavelength position of the localized cavity mode can be tuned by modifying the structural features (lattice constant and layer thicknesses) of the Fabry-Perot microcavity design.

Another possibility of producing interesting optical features is to gradually induce asymmetry into a multilayer stack. An example is shown in Figure 4.8a. In this 25-layer structure of alternating silica and titania films the silica layer thickness was held constant at  $44\pm 2$  nm, while the thickness of the titania layers is successively increased from  $68\pm 2$  nm (left edge) to  $88\pm 2$  nm (center) in 5 nm steps, and then successively decreased again to  $68\pm 2$  nm (right edge). The resulting optical reflection spectrum (Figure 4.8b) shows interesting features with the appearance of four narrow transmission modes between 400 and 550 nm, which are in excellent agreement with the calculated spectra. This agreement between experiment and theory for such an elaborate asymmetric multilayer stack not only shows the precise control over single-layer thickness deposition, but also

confirms the reproducibility of our simple sol-gel deposition approach over tens of consecutive layers. The presence of these narrow optical modes in our microcavity structures and asymmetric Bragg stacks should make these samples interesting candidates for light amplification applications and we are currently investigating possibilities to incorporate light sources into our samples.

#### 4.4 Conclusion

We have developed a sol-gel chemistry-based dip-coating method with all the desirable attributes of solution processing—simple, fast, inexpensive and versatile—and yet produces high-quality thin-film single and multilayer structures, rivaling those fabricated by expensive physical and chemical deposition methods. We discussed causes of typical limitations of sol-gel thin-film processing such as crack formation and occurrence of structural inhomogeneities in multilayer stacks, and introduced strategies to overcome these limitations. We demonstrated that controlled and homogeneous solvent evaporation of the as-deposited films as well as rapid heating and cooling rates are keys in preventing crack formation. The latter proved particularly important for the fabrication of crack-free silica/titania multilayer stacks with precise and reproducible thicknesses of up to 25 alternating layers. Moreover, we showed that such multilayer stacks can be deposited on a variety of substrates over large areas with planar and even curved geometries without loss of structural features.

We used our sol-gel dip-coating process to fabricate high-quality optical components, including Bragg-type reflectors and filters, Fabry-Perot microcavities, and asymmetric stacks. These photonic bandgap-based structures displayed tunable optical

properties with wide reflection bands and well-defined localized cavity modes. The wavelength position of the photonic bandgap and the cavity mode can readily be tuned throughout the entire visible range by controlling the layer thickness during the dip-coating process. Tuning the width of the optical reflection band was demonstrated by fabricating titania-silica nanostructured composite layers with different titania-to-silica ratios. Experimentally obtained reflection spectra were also compared to results from simulations using the transfer-matrix method. Very good agreement was found between the measured and calculated results, confirming again the high precision and reproducibility of the fabrication process. To conclude, the versatility of sol-gel chemistry combined with our inexpensive and rapid thin-film processing route (a 20-layer silica/titania stack can be fabricated in less than two hours) makes our method an attractive alternative to conventional physical/chemical deposition and sputtering techniques. The fabricated multilayer photonic bandgap structures possess excellent structural and optical properties and should be interesting candidates for use in optical and electronic applications.

#### 4.5 References

1. Brinker, C. J.; Scherer, G. W. *Sol-Gel Science*; Academic Press: San Diego, CA, 1990.
2. Livage, J.; Henry, M.; Sanchez, C. *Prog. Solid State Chem.* **1988**, *18*, 259.
3. Dimitriev, Y.; Ivanova, Y.; Iordanova, R. *Journal of UCTM* **2008**, *43*, 181.
4. Innocenzi, P.; Zub, Y. L.; Kessler, V. G., Eds. *Sol-Gel Methods for Materials Processing*; Springer: Dordrecht, 2008.
5. Sanchez, C.; Boissière, C.; Grosso, D.; Laberty, C.; Nicole, L. *Chem. Mater.* **2008**, *20*, 682.

6. Bartl, M. H.; Boettcher, S. W.; Frindell, K. L.; Stucky, G. D. *Acc. Chem. Res.* **2005**, *38*, 263.
7. Schubert, U.; Huesing, N.; Lorenz, A. *Chem. Mater.* **1995**, *7*, 2010.
8. Chujo, Y. *Curr. Opin. Solid State Mater. Sci* **1996**, *1*, 806.
9. Yang, P.; Deng, T.; Zhao, D.; Feng, P.; Pine, D.; Chmelka, B. F.; Whitesides, G. M.; Stucky, G. D. *Science* **1998**, *282*, 2244.
10. Angelomé, P. C.; Fuertes, M. C.; Soler-Illia, G. J. A. A. *Adv. Mater.* **2006**, *18*, 2397.
11. Stucky, G. D.; Bartl, M. H. In *Thin Film Metal-Oxides: Fundamentals and Applications in Electronics and Energy*; Ramanathan, S., Ed.; Springer: New York: 2010, p 255.
12. Yao, H.-B.; Fang, H.-Y.; Wang, X.-H.; Yu, S.-H. *Chem. Soc. Rev.* **2011**, *40*, 3764.
13. Kobler, J.; Lotsch, B. V.; Ozin, G. A.; Bein, T. *ACS Nano* **2009**, *3*, 1669.
14. Hidalgo, N.; Calvo, M. E.; Colodrero, S.; Miguez, H. *IEEE Sensors J.* **2010**, *10*, 1206.
15. Scott, B. J.; Wirnsberger, G.; Stucky, G. D. *Chem. Mater.* **2001**, *13*, 3140.
16. Maex, K.; Baklanov, M.; Shamiryan, D.; Iacopi, F.; Brongersma, S.; Yanovitskaya, Z. *J. Appl. Phys.* **2003**, *93*, 8793.
17. Volksen, W.; Miller, R. D.; Dubois, G. *Chem. Rev.* **2009**, *110*, 56.
18. Subban, C. V.; Zhou, Q.; Hu, A.; Moylan, T. E.; Wagner, F. T.; DiSalvo, F. J. *J. Am. Chem. Soc.* **2010**, *132*, 17531.
19. Knez, M.; Nielsch, K.; Niinistö, L. *Adv. Mater.* **2007**, *19*, 3425.
20. Pore, V.; Ritala, M.; Leskelä, M.; Areva, S.; Järn, M.; Järnström, J. *J. Mater. Chem.* **2007**, *17*, 1361.
21. Ashfold, M. N. R.; May, P. W.; Rego, C. A.; Everitt, N. M. *Chem. Soc. Rev.* **1994**, *23*, 21.
22. Bhakta, R.; Thomas, M.; Hippler, F.; Bettinger, H. F.; Müller, J.; Ehrhart, P.; Devi, A. *J. Mater. Chem.* **2004**, *14*, 3231.



23. Kunkel, R.; Poelsema, B.; Verheij, L. K.; Comsa, G. *Phys. Rev. Lett.* **1990**, *65*, 733.
24. Safi, I. *Surface and Coatings Technology* **2000**, *127*, 203.
25. Kelly, P. J.; Arnell, R. D. *Vacuum* **2000**, *56*, 159.
26. Wang, C. W.; Chen, S. F.; Chen, G. T. *J. Appl. Phys.* **2002**, *91*, 9198.
27. Faustini, M.; Louis, B.; Albouy, P. A.; Kuemmel, M.; Grosso, D. *J. Phys. Chem. C* **2010**, *114*, 7637.
28. Kozuka, H.; Takenaka, S.; Tokita, H.; Hirano, T.; Higashi, Y.; Hamatani, T. *J. Sol-Gel Sci. Technol.* **2003**, *26*, 681.
29. O'Regan, B.; Grätzel, M. *Nature* **1991**, *353*, 737.
30. Ni, M.; Leung, M. K. H.; Leung, D. Y. C.; Sumathy, K. *Renewable Sustainable Energy Rev.* **2007**, *11*, 401.
31. Khan, S. U. M.; Al-Shahry, M.; Ingler, W. B. *Science* **2002**, *297*, 2243.
32. Yoldas, B. E.; O'Keeffe, T. W. *Appl. Opt.* **1979**, *18*, 3133.
33. Hinczewski, D. S.; Hinczewski, M.; Tepehan, F. Z.; Tepehan, G. G. *Sol. Energy Mater. Sol. Cells* **2005**, *87*, 181.
34. Li, Y.; et al. *J. Physics D: Appl. Phys.* **2009**, *42*, 205104.
35. Bellessa, J.; Rabaste, S.; Plenet, J. C.; Dumas, J.; Mugnier, J.; Marty, O. *Appl. Phys. Lett.* **2001**, *79*, 2142.
36. Jasieniak, J.; Sada, C.; Chiasera, A.; Ferrari, M.; Martucci, A.; Mulvaney, P. *Adv. Funct. Mater.* **2008**, *18*, 3772.
37. Rabaste, S.; Bellessa, J.; Brioude, A.; Bovier, C.; Plenet, J. C.; Brenier, R.; Marty, O.; Mugnier, J.; Dumas, J. *Thin Solid Films* **2002**, *416*, 242.
38. Jiang, K.; Zakutayev, A.; Stowers, J.; Anderson, M. D.; Tate, J.; McIntyre, D. H.; Johnson, D. C.; Keszler, D. A. *Solid State Sci.* **2009**, *11*, 1692.
39. Saleh, E. A. B.; Malvin, T. C. *Fundamentals of Photonics*; John Wiley & Sons Inc., 1991.
40. Bartl, M. H.; Puls, S. P.; Tang, J.; Lichtenegger, H. C.; Stucky, G. D. *Angew. Chem. Int. Ed.* **2004**, *43*, 3037.

41. Larouche, S.; Martinu, L. *Appl. Opt.* **2008**, *47*, C219.
42. Bockmeyer, M.; Löbmann, P. *Chem. Mater.* **2006**, *18*, 4478.
43. Bockmeyer, M.; Löbmann, P. *Thin Solid Films* **2007**, *515*, 5212.
44. Scriven, L. E. In *Better Ceramics Through Chemistry III*; Brinker, C. J., Clark, D. E., Ulrich, D. R., Eds.; Mat. Res. Soc.: Pittsburgh, PA, 1988, p 717.
45. Schüler, A.; Dutta, D.; de Chambrier, E.; Roecker, C.; De Temmerman, G.; Oelhafen, P.; Scartezzini, J.-L. *Sol. Energy Materials Sol. Cells* **2006**, *90*, 2894.
46. MacLeod, A. H. *Thin-Film Optical Filters*; Institute of Physics Publishing: Bristol, 2001.
47. Kuznetsova, I. N.; Blaskov, V.; Znaidi, L. *Mater. Sci. Eng. B* **2007**, *137*, 31.
48. Rath, H.; Dash, P.; Som, T.; Satyam, P. V.; Singh, U. P.; Kulriya, P. K.; Kanjilal, D.; Avasthi, D. K.; Mishra, N. C. *J. Appl. Phys.* **2009**, *105*, 074311.
49. Fink, Y.; Winn, J. N.; Fan, S.; Chen, C.; Michel, J.; Joannopoulos, J. D.; Thomas, E. L. *Science* **1998**, *282*, 1679.
50. Lee, H.-Y.; Yao, T. *J. Appl. Phys.* **2003**, *93*, 819.

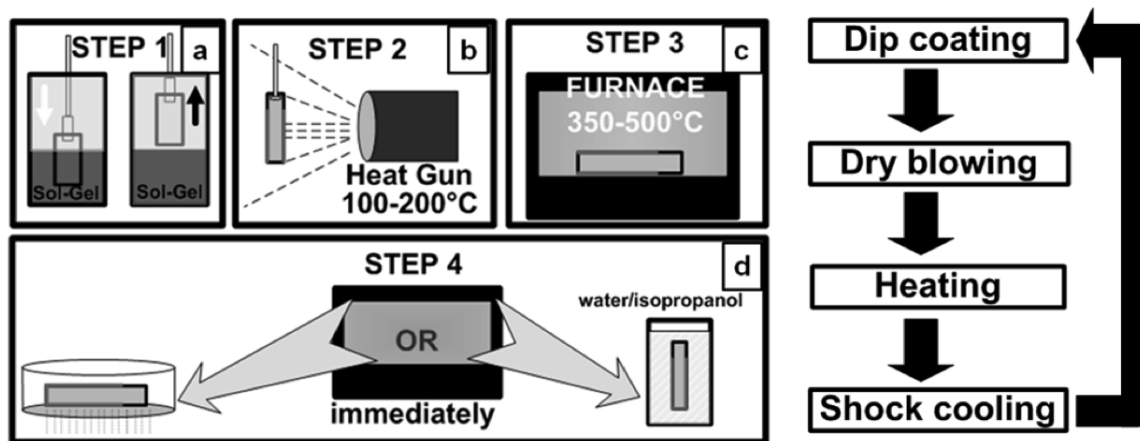


**Figure 4.1:** Thin-film deposition cycle for the fabrication of sol-gel thin-film layers.

- a) step 1: dip-coating; b) step 2: dry-blowing; c) step 3: heat-treatment (annealing);  
 d) step 4: shock-cooling. (Right). Flow chart depicting the main steps of the deposition cycle.

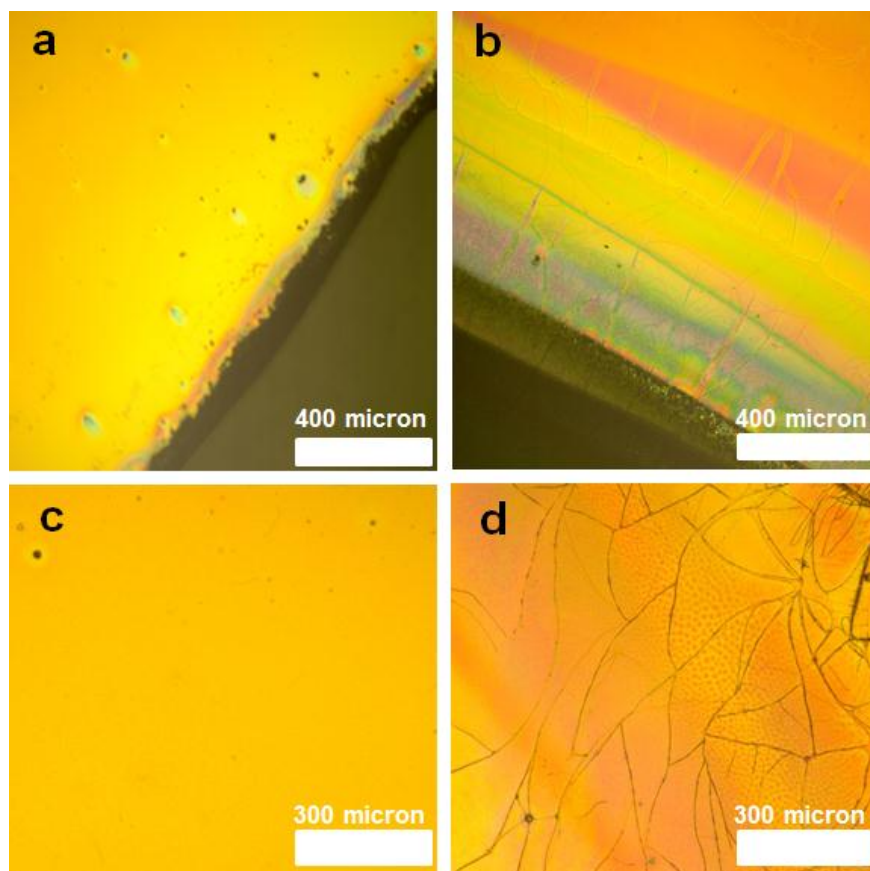


**Figure 4.2:** Optical micrographs of 12 alternating silica/titania thin-film layers deposited onto a silicon (100) wafer. Top: Samples fabricated including (a) and omitting (b) the dry-blowing step in the deposition cycle (Figure 4.1). Bottom: Samples fabricated including (c) and omitting (d) the shock-cooling step in the deposition cycle (Figure 4.1)

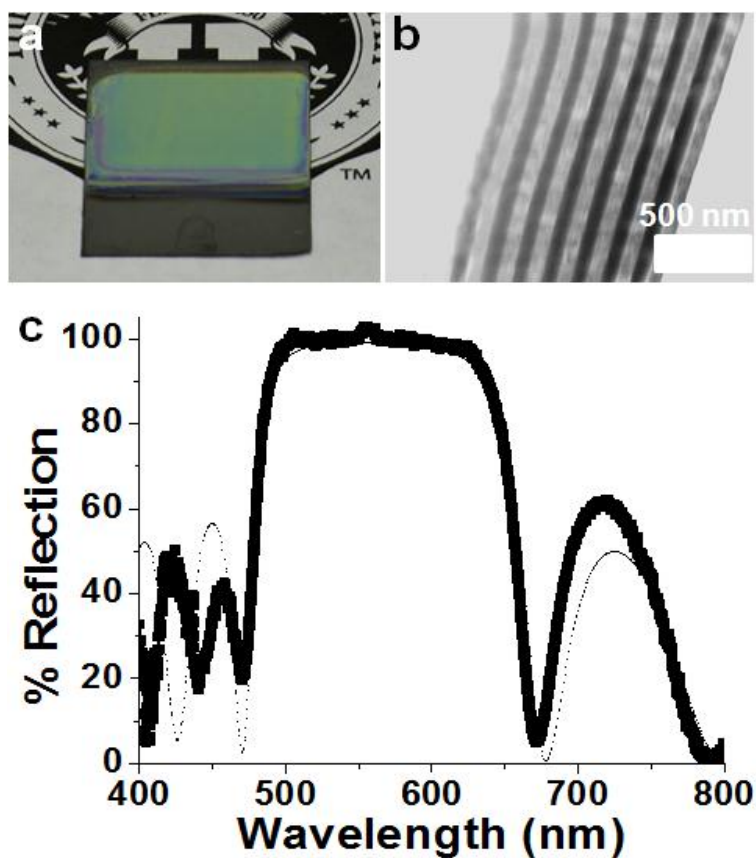


**Figure 4.3:** Photograph and cross-sectional SEM image of a thin-film Bragg stack consisting of 14 alternating layers of silica ( $88\pm 2$  nm; dark layers) and titania ( $75\pm 2$  nm; bright layers) deposited onto a silicon (100) wafer (a, b). Corresponding optical reflection spectrum (solid line) and simulated spectrum (c) (dotted line).

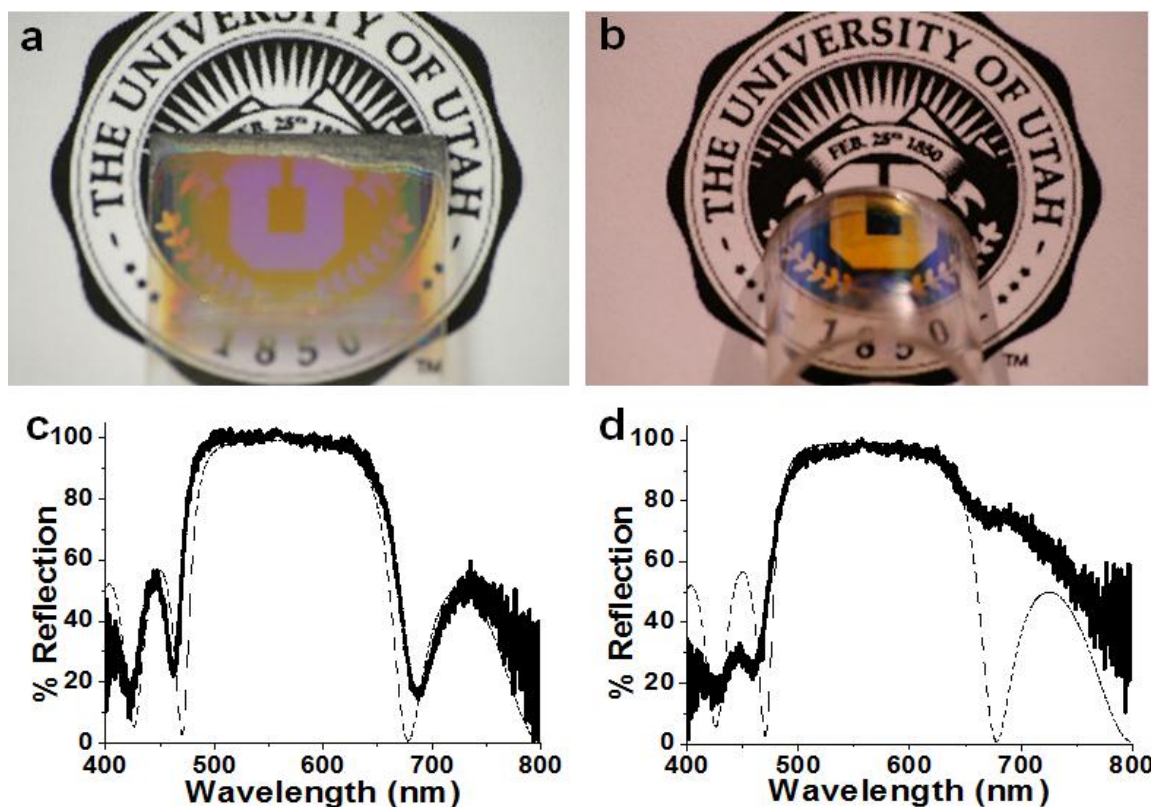


**Figure 4.4:** Photographs of thin-film Bragg stacks consisting of 12 alternating layers of silica ( $88\pm 2$  nm; dark layers) and titania ( $75\pm 2$  nm; bright layers) deposited onto (a) a planar borosilicate glass substrate and (b) a curved quartz-glass substrate. c, d) Corresponding optical reflection spectra (solid lines) of the stacks on (c) a planar borosilicate glass substrate and (d) a curved quartz-glass substrate. Simulated spectra are given as dotted lines.

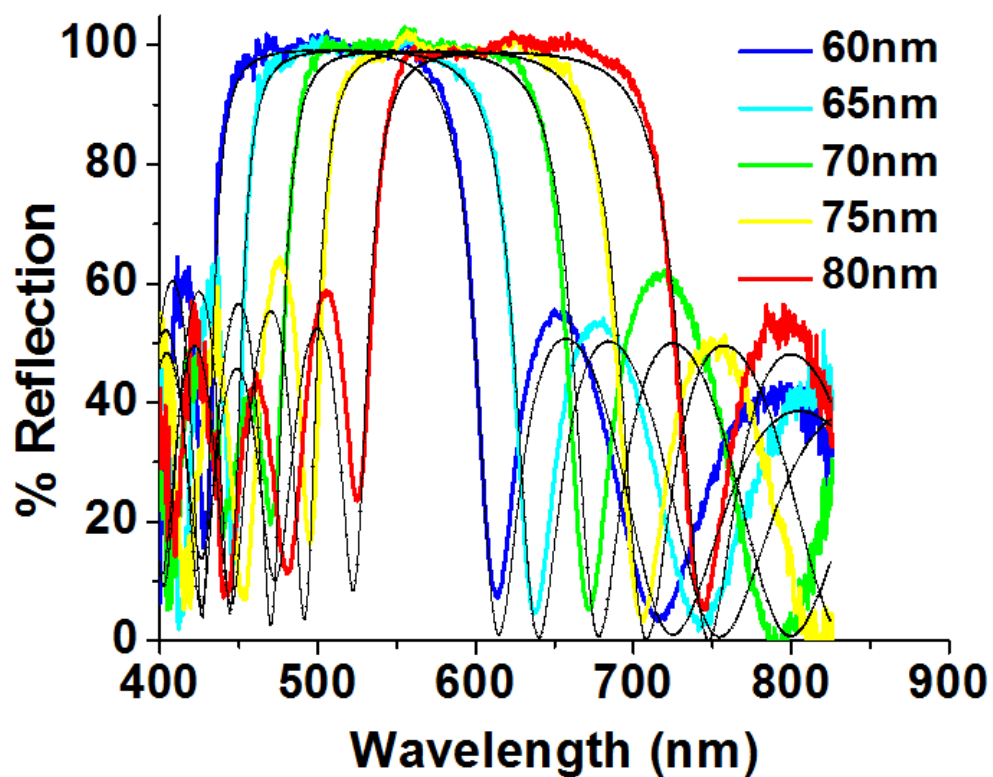


**Figure 4.5:** Optical reflection spectra of a Bragg stack of 12 alternating silica/titania layers. The silica layer thickness was held constant at  $88\pm 2$  nm, whereas the titania layer thickness was varied between  $60\pm 2$  and  $80\pm 2$  nm, as indicated in the figure. The simulated spectrum is given as a dotted line.

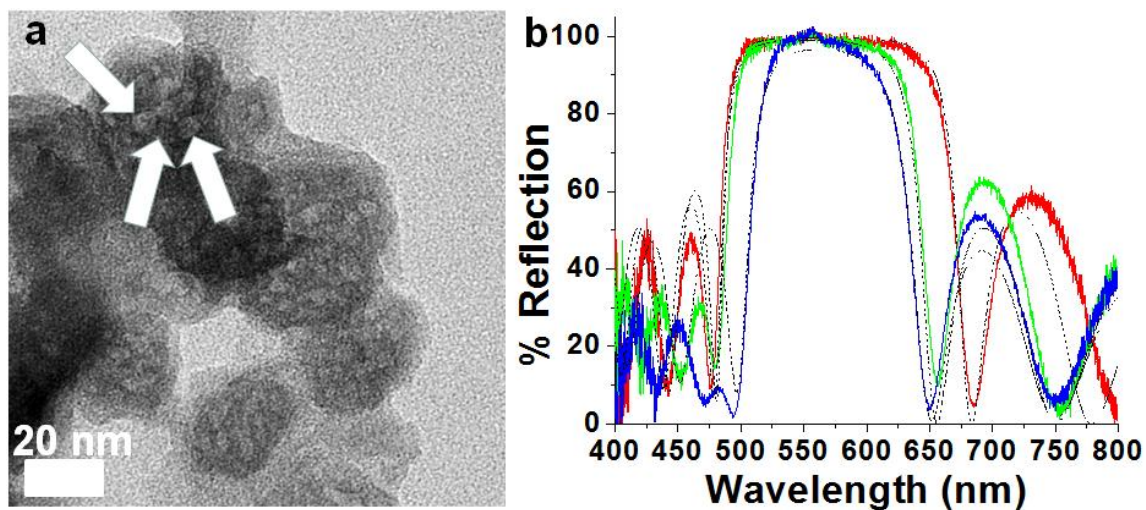


**Figure 4.6:** TEM image of a nanoporous titania thin-film sample (a). Some of the pores are indicated by arrows. b) Optical reflection spectra of three 14-layer silica/titania Bragg stacks with differing refractive indices of the titania layer deposited onto a silicon (100) substrate. The titania layer refractive indices are  $2.34 \pm 0.02$  (red spectrum),  $2.1 \pm 0.1$  (green spectrum), and  $1.8 \pm 0.1$  (blue spectrum). Simulated spectra are given as dotted lines.



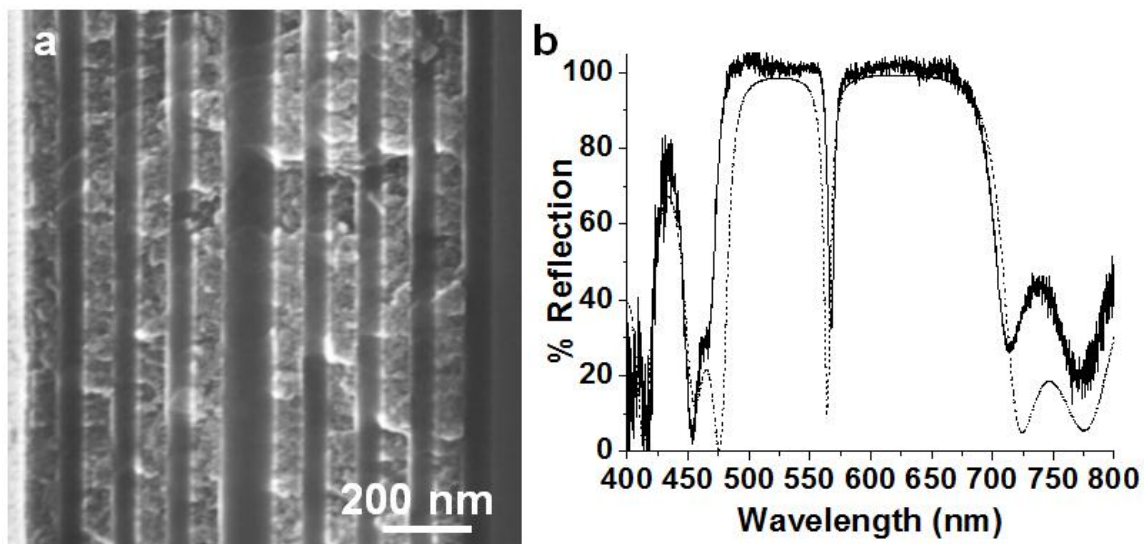


**Figure 4.7:** Cross-sectional SEM image (a) and optical reflection spectrum (b) of a Fabry-Perot microcavity structure deposited onto a silicon (100) substrate. The microcavity is composed of a central silica defect layer with a thickness of  $176\pm 2$  nm sandwiched between two 8-layer silica/titania Bragg stacks with silica and titania thicknesses of  $88\pm 2$  nm and  $70\pm 2$  nm, respectively. The optical cavity mode occurs at a wavelength position of 568 nm. The simulated spectrum is given as a dotted line.

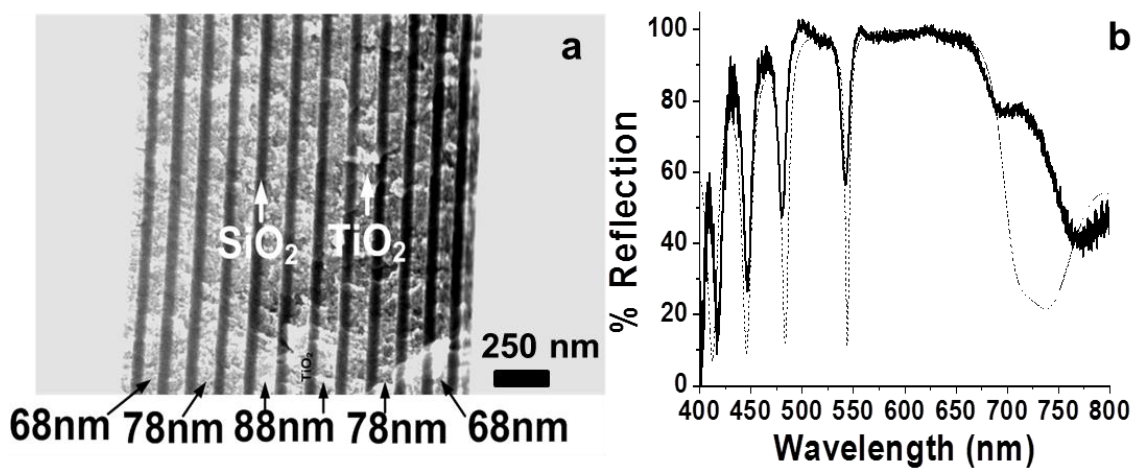


**Figure 4.8:** Cross-sectional SEM image (a) and an optical reflection spectrum (b) of an asymmetric 25-layer silica/titania Bragg stack deposited onto a silicon (100) substrate. The silica layer thickness was held constant at  $44 \pm 2$  nm, while the titania layer thickness was varied in 5 nm steps from  $68 \pm 2$  nm to  $88 \pm 2$  nm and back to  $68 \pm 2$  nm. The simulated spectrum is given as a dotted line.

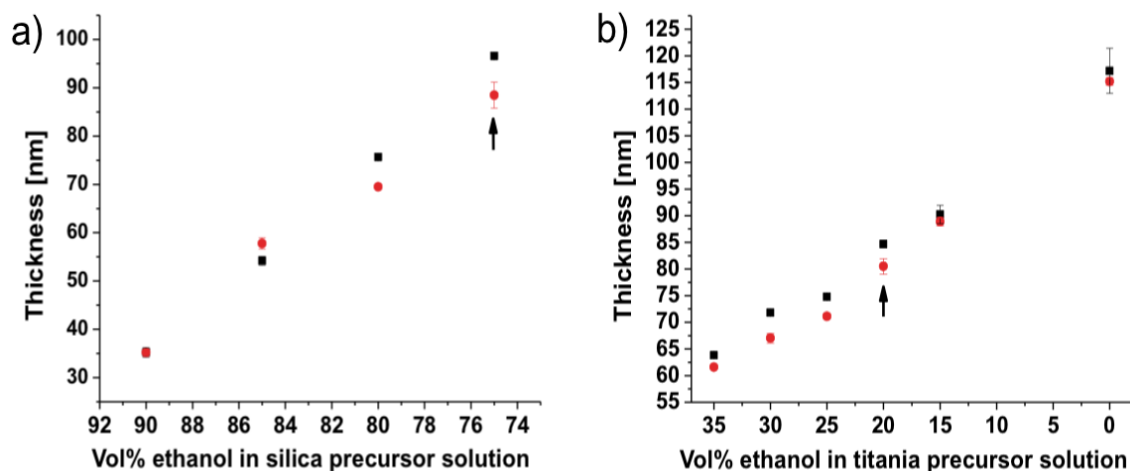


**Figure 4.9:** Graphs showing thickness of a) silica and b) titania thin films as a function of ethanol content of the respective precursor solutions (in volume percent). Film thicknesses were determined after a single deposition cycle (black) and after an additional heat treatment for at least 1 hour at 500 °C (red). For example, to fabricate a silica film with a thickness of  $88 \pm 2$  nm (arrow in (a)), 5 mL of the original silica stock solution was diluted with 15 mL ethanol. Likewise, to fabricate a  $80 \pm 2$  nm titania film (arrow in (b)), 16 mL of titania stock solution were diluted with 4 mL of ethanol.

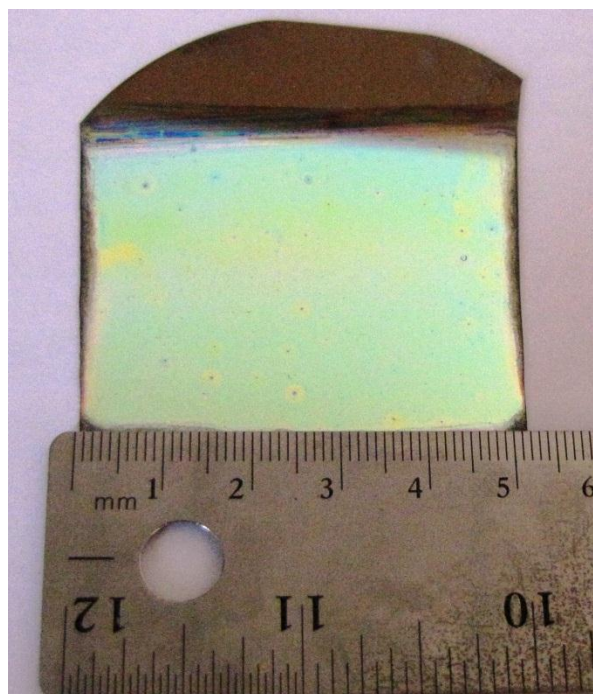


**Figure 4.10:** Photograph of a large-area (5x4 cm) thin-film Bragg stack consisting of 12 alternating layers of silica ( $88\pm 2$  nm) and titania ( $70\pm 2$  nm) deposited onto a silicon (100) wafer.

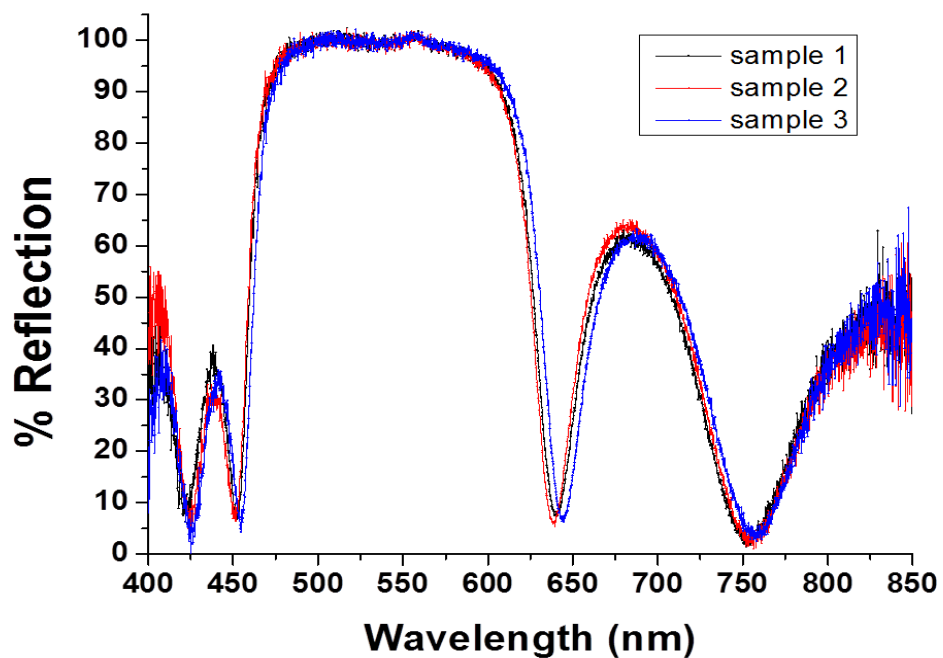


**Figure 4.11:** Optical reflection spectra of three thin-film Bragg stacks consisting of 12 alternating layers of silica and titania with thicknesses of  $88\pm 2$  nm and  $70\pm 2$  nm, respectively, deposited onto a silicon (100) wafer. The three samples were fabricated at different times but under the same experimental conditions (i.e., precursor solution composition, dip-coating parameters, drying and heat treatments) and demonstrate the excellent reproducibility of the deposition and processing method.

## CHAPTER 5

# MAGNETIC FUNCTIONALIZATION STUDIES AND MAGNETO-OPTICAL MEASUREMENTS OF SOL-GEL DERIVED TITANIA AND SILICA THIN FILMS

### 5.1 Introduction

The successful development of next generation spintronic devices will greatly depend on the magnetic functionalization capabilities of nanostructured thin-film materials. This involves the fabrication of distinct magnetic domains with nanometer feature sizes and reversible magnetic moments.<sup>1-4</sup> Additionally, the functionalization procedure has to be reproducible with nanometer resolution while being simultaneously fabricated at low cost as recently reviewed by Lau et al.<sup>5</sup> Although advances in lithography have met some criteria in developing next generation spintronic devices other challenges remain, especially those related to low-cost fabrication and higher resolution patterning.<sup>6</sup> While the remaining challenges seem contradictory using conventional lithography methods, low-cost self-assembly based processes might be able to address and solve them.

One emerging and promising self-assembly route is the fabrication of nanometer-sized features in structured oxide-materials using surfactant and colloidal assembly, and

templating sol-gel chemistry.<sup>7-10</sup> Not only is it a simple, rapid and inexpensive route for fabricating large-area periodically organized structures, but its sol-gel nature also provides versatility.<sup>11,12</sup> Research in the Bartl group applies such methods for creating nanostructured photonic materials, including replication of biological beetle scales to fabricate photonic crystals and sol-gel dip-coating of crack-free high-quality thin-film optical devices using surfactant based sol-gel chemistry.<sup>13-16</sup> Additionally, photonic crystals have been successfully synthesized using sol-gel routes and, if magnetically functionalized, they are potential candidates in exploring unprecedented magneto-optical phenomena.<sup>17-23</sup>

The area of magnetic functionalization of sol-gel derived thin films has not been fully explored yet. Especially the functionalization of sol-derived metal-oxide materials doped with transition metal ions is a promising route in obtaining high-Curie-temperature ferromagnetism in oxide materials.<sup>24,25</sup> Of special interest is the property of Co-ion-doped titania materials. The theoretical prediction of strong carrier-mediated room-temperature ferromagnetism in p-type ZnO with 5 at% Mn<sup>26</sup> and the experimental discovery of room-temperature ferromagnetism in 7 at% Co-doped TiO<sub>2</sub><sup>27</sup> has launched an effort in developing and improving possible magnetic semiconductors for next generation spintronic applications.<sup>24,25,27-29</sup>

The origin of the observed room-temperature ferromagnetism in the so-termed dilute magnetic semiconductors (DMS) is controversial.<sup>30</sup> An intrinsic ferromagnetic-origin model favors a long range ferromagnetic exchange between the ionic dopants or Weiss domains via the conduction band of the host system.<sup>25</sup> On the contrary an extrinsic ferromagnetic-origin model favors the formation of metallic nanoparticles responsible for

the ferromagnetic response at room temperature. Extensive studies on  $\text{Co}^{2+}$  ions incorporated into anatase titania hosts have shown evidence for both hypotheses.<sup>31</sup> Both the presence of metallic cobalt and  $\text{Co}^{2+}$  ions incorporated into the titania host system have been identified in high-temperature ferromagnetic DMS.<sup>24,32</sup> Despite the controversy about the ferromagnetic origin, room temperature ferromagnetism has been reported for a variety of semiconductors and oxide systems using various deposition methods. These methods include oxygen plasma assisted molecular beam epitaxy,<sup>33</sup> electrochemical deposition,<sup>29</sup> pulsed laser deposition,<sup>27</sup> reactive co-sputtering,<sup>34</sup> and colloidal nanocrystal synthesis.<sup>25</sup>

The goal of this study was to investigate a sol-gel route for fabricating room-temperature ferromagnetic DMS thin films and to measure their magneto-optical properties using a home-built Faraday rotation setup. The rest of this chapter is organized as follows: First, structural characterization studies of Co-doped anatase titania thin films are presented. Second, magnetic measurements of Co-doped samples using a superconducting quantum interference device (SQUID) magnetometer are described and results are discussed. Third, assembly of a home-built magneto-optical Faraday rotation measurement setup is presented and attempts to measure Faraday rotation angles of ion-doped titania thin films are discussed. The chapter concludes with a summary of the results and presents preliminary vibrating sample magnetometer (VSM) results of an alternative sol-gel route by synthesizing  $\text{Fe}_3\text{O}_4$  nanoparticles in-situ within titania and silica thin films.



## 5.2 Experimental Section

### 5.2.1 Preparation of ion-doped sol-gel precursor solutions

The titania precursor solution was prepared by mixing 60 mL titanium(IV)isopropoxide (Acros) and 65 mL ethanol under vigorous stirring for 30 minutes (careful, exothermic reaction!). A solution of 124 mL ethanol, 0.6 mL hydrochloric acid (12 M) and 1.15 mL of 18 $\Omega$  deionized water (DI water) was then added to the titania solution and stirred for an additional 30 minutes. This mixture was aged for at least 48 hours at room temperature before further use. The silica precursor solution was prepared by adding 105 mL tetraethylorthosilicate (Aldrich) to a mixture of 12.3 mL DI water, 76 mL ethanol and 6.3 mL HCl (0.01 M) and mixing for 30 minutes at room temperature. This solution was aged for at least 48 hours at 60 °C before further use.

For doping sol-gel derived thin-films metal-ion salts, such as cobalt (II) nitrate hexahydrate (Aldrich), ferric (III) nitrate nonahydrate (Mallinckrodt), iron (II) chloride tetrahydrate (Aldrich), iron (III) chloride hexahydrate (Aldrich), were first dissolved in ethanol and then added to the sol-gel precursor solution sample volume. The mixture was then mixed by vortexing before thin films were deposited by a dip-coating process. The amount of dissolved ions was varied typically between 0.1 at % and 3 at % relative to the amount of Ti-atoms present in the sample volume precursor solution.

### 5.2.2 Ion-doped thin film deposition process

Ion-doped thin films were deposited by dip-coating onto cleaned substrates. Cleaning of the substrates was done by rinsing with isopropanol and drying in a stream of nitrogen. Substrates were then immersed into the ion-doped sol (titania or silica precursor

solution) and vertically withdrawn at a constant speed of 12.5 cm/minute. The dip-coating process was immediately followed by heating the deposited film in a flowing stream of hot air (100-200 °C; produced by a heat gun) for rapid evaporation of volatile solvents. The dried films were heat-treated (calcined) for 3h at 450 °C in a muffle furnace and then allowed to cool down to room temperature.

### 5.2.3 X-Ray diffraction characterization of TiO<sub>2</sub> thin-films

The sol-gel thin film and powder crystallinity was studied by X-ray diffraction measurements conducted on a PANalytical Alpha 1 XRD System (Cu-K $\alpha$  radiation).

### 5.2.4 SQUID magnetic characterization of TiO<sub>2</sub> thin-films

Magnetic characterization studies of doped titania thin films were conducted using a Quantum Design MPMS-5XL 5T superconducting quantum interference device (SQUID) magnetometer. For these measurements, films samples were scraped off from the substrates using a sharp Si-waver edge and then loaded into gelatin capsules. Direct current magnetization studies at room temperature were conducted by sweeping the magnetic field (DC measurement) between  $\pm 10\,000$  Oersted (Oe). These measurements were performed on a SQUID instrument in the research group of Prof. Miller (Department of Chemistry, University of Utah) and with the assistance of his students.

### 5.2.5 VSM characterization of TiO<sub>2</sub> and SiO<sub>2</sub> thin-films

Vibrating sample magnetic characterization studies were conducted on a Quantum Design Vibrating Sample Magnetometer (VSM), a hardware add-on for the Physical

Property Measurement System (Quantum Design). Small thin-film samples on Si (100) waver substrates were loaded into a sample holder, vertically aligned relative to the magnetic field and oscillated with a frequency of 40Hz. A gradiometer detection coil measured changes in magnetic flux caused by the vibration of the sample. Temperature dependent (4 K to room temperature) direct current magnetization studies were conducted by sweeping the magnetic field (DC measurement) between  $\pm 10\,000$  Oe. These measurements were performed on a VSM instrument in the group of Prof. Chesnel (Department of Physics, Brigham Young University) and with her assistance.

### 5.2.6 Magneto-optical studies using a home-built

#### Faraday rotation measurement setup

Magneto-optical studies were conducted in the visible spectrum range using a home-built Faraday rotation measurement setup shown in Figure 5.5. The 532 nm laser beam (B&W Tek, Inc.) is circularly polarized by a quarter-wavelength plate and then split into a signal beam and a reference beam using a visible-range polarizing beam splitter. The signal beam is then linearly polarized using a Glen-Thompson polarizer and directed in normal incidence through the thin-film sample which is positioned between the two poles of a water-cooled electromagnet (GMW 5403FG). The electromagnet is oriented  $23^\circ$  relative to the signal beam and is powered by a unipolar power supply (Sorensen DCR-40-40B) interconnected through a home-built current-switch-box for current-reversing capabilities in the electromagnet. The transmitted signal beam is then passed through a Glen-Thompson analyzer that is oriented  $45^\circ$  relative to the polarizer and focused onto an autobalanced photodetector (New Focus, Nirvana 2007).

A Faraday experiment is conducted by sweeping the magnetic field measured by a Hall probe (SENIS GmbH, YM12-3-5-2T) of the electromagnet between  $\pm 1$  Tesla and by simultaneously measuring the intensity difference of the signal beam relative to the reference beam. The rotation angle  $\varphi$  can then be computed by rearranging Malus' law to:

$$\varphi = \cos^{-1} \sqrt{\frac{\Delta I}{I_0}} \quad [5.1]$$

An equal change in measured light intensity of the signal beam occurs if the polarizer is rotated by an angle  $\Delta\theta = \varphi$  with respect to the analyzer.

A NI-DAQmx card (National Instrument) was employed for interfacing the hardware components (power supply, current switch box, Hall probe, and differential amplifier) with a PC workstation. In-house GUI software written in LabView was used in controlling the hardware components and for measuring, plotting and analyzing the measured signal difference with respect to applied magnetic fields.

### 5.3 Results and Discussion

The goal of this work is to investigate the possibility of fabricating room-temperature dilute magnetic semiconductor thin films via a simple sol-gel route. Dilute magnetic semiconductors based on Co-doped anatase titania ( $\text{TiO}_2$ ) thin films have been extensively studied for a variety of deposition methods since the discovery of room-temperature ferromagnetism in Co-doped anatase  $\text{TiO}_2$  thin films.<sup>25,27,29,32</sup>

### 5.3.1 Sample preparation and magnetic studies

Titania samples were fabricated by a sol-gel chemistry route from liquid precursor solutions. For magnetically activated titania samples the dopant ions were dissolved in the precursor solution before thin-film or powder processing. To ensure samples fabricated in this way possess the desired anatase titania crystalline form, XRD studies were performed on thin-film and powder samples. Figure 5.1 shows the measured XRD spectra for a sol-gel titania thin film deposited by dip-coating onto a Si (100) wafer and a titania powder sample derived from the same sol-gel stock solution as the thin films (both samples were calcined at 450 °C for 3 hours). A comparison with tabulated diffraction peak positions reveals that the diffraction patterns of both can be assigned to the desired anatase titania crystalline phase.<sup>35</sup>

Room-temperature magnetization measurements of Co-doped anatase titania thin films were performed on a SQUID magnetometer. Magnetic hysteresis measurements on a 0.5 % Co-doped titania thin film sample are given in Figure 5.2 and show clear evidence of ferromagnetic response. The magnetization saturation of  $\pm 0.014$  emuOe/gram and the presence of a coercive force (in this case of 50 Oe) are typical features of ferromagnetic behavior. Figure 5.3A shows the result of a room-temperature hysteresis measurement of a 0.5% Co-doped mesostructured titania thin film sample (Figure 5.3B shows a representative TEM image of the mesoporosity). Despite the presence of mesoporosity throughout the thin-film sample, clear ferromagnetic behavior with a coercivity of 50 Oe was observed. However, for the mesoporous samples, the calculation of a saturation magnetization value is difficult due to the presence of a large

paramagnetic (from titania host) contribution superimposed onto the weaker ferromagnetic hysteresis signal.

Unfortunately, the ferromagnetic response for bulk and mesoporous titania thin films strongly varies from sample to sample and the results shown above are not representative. In fact, results varied from purely ferromagnetic to purely paramagnetic responses. Examples are shown in Figures 5.4A and 5.4B for 0.5 % Co-doped titania samples. It should be pointed out that extreme precaution was taken to exclude sample preparation inconsistencies. For example, samples were prepared from the same precursor solutions, under the same processing conditions and with the same heat-treatment protocol. Additionally, special care was taken during the studies to exclude any contamination in the thin-film fabrication process that could result in a magnetic response (no metal containers, needles, lab tools etc.). Nevertheless, even these very carefully conducted systematic studies to investigate the ferromagnetic origin in the measured hysteresis signal of Co-doped titania did not give conclusive results. A detailed summary of systematic susceptibility studies of varying Co-ion concentrations doped into the sol-gel derived titania thin films is summarized; see Table 5.1. The study revealed a negative susceptibility (diamagnetic response) for dopant concentrations of 1 at% measured at magnetic fields of 1000 Oe. Contrary, a doping concentration below 1 at% resulted in a positive susceptibility (either paramagnetic or ferromagnetic response). This finding stands in strong contrast to previously reported studies for which clear ferromagnetic responses were observed utilizing various deposition methods.<sup>24,25,27,28,32,36</sup>

It should be pointed out that the observed difficulties in reproducing magnetic responses in magnetically-doped titania samples is not that different from reported results

found in the literature. Especially for sol-gel-derived Co-doped titania samples one finds inconsistencies from study to study and often also within a given study.<sup>31,37</sup> These inconsistencies seem to be rooted in the intrinsic chemical/physical processes that occur during the heat treatment/calcination processes. For example, it is argued that oxygen vacancies play a crucial role as a long range ferromagnetic carrier.<sup>36</sup> A different study emphasizes the importance of oxygen vacancies in inhibiting the formation of non-magnetic CoTiO<sub>3</sub> clusters while simultaneously promoting the formation of Co-rich clusters.<sup>24</sup> Based on these findings, we carefully conducted several magnetization studies using a nitrogen carrier gas or by pulling a vacuum during the calcination process. Despite careful preparation and measurement procedures no enhancement in ferromagnetism was found to support the previously reported findings.

Results reported in the literature on magnetically doped metal-oxide compounds as well as results reported in this dissertation are perhaps best summarized in quoting a recent paper by Coey and Chambers titled ‘Oxide Dilute Magnetic Semiconductors- Fact or Fiction?’ in which the authors address the issue of drawing definite conclusions in observing DMS effects at room-temperature.<sup>31</sup> The report concludes that the measured ferromagnetism in numerous reports is often attributed to uncontrolled secondary phases in the host system induced by dopants. And if ferromagnetism was observed, it is most likely attributed to defects present in the metal-oxide film rather than being a DMS effect as often claimed.<sup>31,37</sup>

### 5.3.2 Magneto-optical Faraday rotation studies

An additional difficulty in studying the magnetic properties of sol-gel thin-film samples is the lack of large sample amounts. The thin-film thickness is on the order of 100 nm and thus much thinner than the diamagnetic substrate (quartz slide). This leads to very small signal-to-noise ratios in SQUID and VSM measurements, further contributing to inconsistencies. One way to circumvent this problem is to scrape many of these thin films off the substrate and load them into gel capsules for magnetic measurements. However, an inherent problem with this method is sample contamination during scraping and collecting of the thin films. Therefore, an alternative method for determining magnetic properties of thin-film samples was utilized: Magneto-optical Faraday rotation measurements.

The Faraday effect or magneto-optical rotation can be measured directly on thin-film samples deposited onto substrates without the need of further sample handling that could cause contamination. The Faraday effect describes a plane of polarization rotation of linearly polarized light as it passes through an isotropic medium oriented parallel to an applied magnetic field.<sup>38</sup> The angle of rotation  $\varphi$  is proportional to the applied magnetic-field intensity,  $B$ , and the length of the magnetized isotropic medium,  $l$ , and scales with a material specific proportionality constant termed the Verdet constant,  $V$ :

$$\varphi = VBl \quad [5.2]$$

The Faraday effect is based on artificial circular birefringence in that the left and right-handed circular components experience slightly different velocities in the magnetized



medium, causing a relative phase shift between them. Measuring the angle of rotation as a function of applied magnetic field allows investigating the magnetic dynamics of a magnetized medium fabricated under varying conditions.<sup>39-42</sup>

To improve the signal-to-noise ratio in a Faraday rotation measurement the relative orientation of both polarizers has to be optimized. The optimal orientation of both polarizers relative to each other can be determined by computing the maximum turning point of the intensity-response  $I(\theta)$  slope as a function of relative rotation angles  $\theta$  utilizing Malus' law<sup>38</sup>:

$$I(\theta) = I_0 \cos^2 \theta \quad [5.3]$$

A polarized beam subject to a Faraday effect experiences a plane of rotation,  $\varphi$ . The light intensity measured after the analyzer is then given by:

$$I(\theta, \varphi) = I_0 \cos^2(\theta - \varphi) \quad [5.4]$$

Taking the derivative with respect to the relative angle  $\theta$  results:

$$\frac{\partial I}{\partial \theta} = I_0 (\sin 2((\theta - \varphi))) \quad [5.5]$$

For small  $\varphi$  a maximum intensity difference occurs at  $\theta = 45^\circ$ .

To determine magneto-optical Faraday effect responses of the sol-gel derived thin-film samples, a Faraday rotation setup was assembled as described in section 5.2.3.

A schematic diagram of the setup is also given in Figure 5.5. In order to validate the home-built Faraday rotation setup, the magneto-optical response of a 0.17 mm thick VWR borosilicate glass coverslip was measured (Figure 5.6A) and a Verdet constant of  $0.0248 \pm 0.0025$  min/Gauss cm was determined. This value is within 5% of previously reported Verdet constants for borosilicate glass at 532 nm.<sup>38,43,44</sup> We further measured a 1 nm thick equiatomic CoPt thin-film layer sputtered on a glass substrate (courtesy of Prof. Guruswamy, Department of Metallurgical Engineering, University of Utah); see Figure 5.6B. A clear ferromagnetic/super paramagnetic magnetization curve was measured in accordance with previously reported magnetization curves.<sup>45</sup>

Following these test measurements, Faraday rotation measurements were attempted on 0.5% Co-doped titania and 0.5% Mn-doped titania thin films. Figure 5.7 compares the measured signals for the two samples to the background-rotation spectrum of the glass substrate only. While no change in the Faraday signal was obtained for the Co-doped sample a slight paramagnetic response was observed for the Mn-doped sample. However, it turned out that Faraday signals from sol-gel derived samples are also very difficult to obtain with high reliability. It seems that the magnetic response of sol-gel derived ion-doped titania thin-film samples are too low to be clearly distinguishable from the background signal of the used substrates. Additionally, noise sources not inherent to our setup (for example, building vibrations or laser power drifts) were hard to quantitatively account for and altered the detected signal. All these noise sources limit the angular-resolution detection sensitivity of our setup to less than  $0.01^\circ$ , as experimentally determined by analyzing the standard-deviation of the measured signal at varying magnetic fields. Additionally, the detection of magnetic properties in ion-doped thin

films lies in the magnetic dopant concentration. Dopant levels around 1-2 at% are not sufficient in reliably detecting Faraday signals for discriminating ferromagnetic from paramagnetic behavior in these films, as concluded from our magnetization/magneto-optical studies. Unfortunately, increasing dopant concentration to higher levels (4 or more at% relative to the Ti-atoms) leads to strong crack formation within the sol-derived thin-film samples, resulting in unwanted light scattering during the magneto-optical measurements. In summary, the fidelity of detecting ferromagnetic responses in sol-gel derived titania thin-film samples is not high enough to allow for detailed and systematic magnetization/magneto-optical studies. The feasibility of potentially utilizing sol-gel derived magnetic materials for spintronic and other magnetic applications is thus still in a state of uncertainty and other characterization methods and more efficient sample configurations will be needed in the future.

#### 5.4 Conclusion and Outlook

The feasibility of fabricating dilute magnetic semiconductor thin films using a simple sol-gel route was investigated. Detailed SQUID and Faraday rotation studies of Co-doped titania thin films showed no trend in its magnetization response at room temperature. Additionally, incorporating impurities other than Co-ions into sol-gel derived thin films showed no significant increase in the magnetic functionalization at room temperature. A home-built Faraday rotation setup was utilized to study magneto-optical effects of ion-doped titania and silica thin films. However, the resolution limit was not sufficient in resolving Faraday rotations much smaller than  $0.01^\circ$ .

We are currently investigating an alternative route in magnetically functionalizing sol-gel derived thin films via in-situ synthesis of  $\text{Fe}_3\text{O}_4$  nanoparticles into the titania or silica thin-film network. This one-pot functionalization synthesis method is a potentially very attractive route for incorporating nanoparticles into an oxide sol-gel network without surface functionalization during the fabrication process. Preliminary VSM results of varying amount of  $\text{Fe}_3\text{O}_4$  nanoparticles synthesized within titania thin films are shown in Figures 5.8, 5.9, and 5.10. A titania thin-film sample without the addition of  $\text{Fe}_3\text{O}_4$  nanoparticles showed no temperature dependence of field-cooled magnetization above 100K measured at a magnetic field of 1000Oe (see Figure 5.8). On the other hand, the addition of 2 %  $\text{Fe}_3\text{O}_4$  nanoparticles shows a significant temperature dependence of the field cooled magnetization, which increases with the thickness of deposited titania layers (compare Figures 5.9 and 5.10). Similar trends have been found for in-situ synthesis of  $\text{Fe}_3\text{O}_4$  nanoparticle into a silica thin-film network. We are currently investigating the sol-gel thin-film morphology after incorporating  $\text{Fe}_3\text{O}_4$  nanoparticles, the size and size distribution of the synthesized  $\text{Fe}_3\text{O}_4$  nanoparticles and we are additionally tuning the synthesis parameters to increase the magnetic functionalization of sol-gel derived thin films.

### 5.5 References

- (1) Wolf, S. A.; Awschalom, D. D.; Buhrman, R. A.; Daughton, J. M.; von Molnár, S.; Roukes, M. L.; Chtchelkanova, A. Y.; Treger, D. M. *Science* **2001**, 294, 1488.
- (2) Žutić, I.; Fabian, J.; Das Sarma, S. *Reviews of Modern Physics* **2004**, 76, 323.
- (3) Bader, S. D.; Parkin, S. S. P. *Annual Review of Condensed Matter Physics* **2010**, 1, 71.

- (4) Thomson, T.; Hu, G.; Terris, B. D. *Phys. Rev. Lett.* **2006**, *96*, 257204.
- (5) Lau, J. W.; Shaw, J. M. *J. Phys. D: Appl. Phys.* **2011**, *44*, 303001.
- (6) *Magnetic Nanostructures*; Aktas, B.; Tagirov, L.; Mikailov, F., Eds.; Springer, 2007; Vol. VIII.
- (7) Yang, P.; Deng, T.; Zhao, D.; Feng, P.; Pine, D.; Chmelka, B. F.; Whitesides, G. M.; Stucky, G. D. *Science* **1998**, *282*, 2244.
- (8) Caruso, R. A. *Angewandte Chemie International Edition* **2004**, *43*, 2746.
- (9) Mann, S.; Burkett, S. L.; Davis, S. A.; Fowler, C. E.; Mendelson, N. H.; Sims, S. D.; Walsh, D.; Whilton, N. T. *Chem. Mater.* **1997**, *9*, 2300.
- (10) Bartl, M. H.; Puls, S. P.; Tang, J.; Lichtenegger, H. C.; Stucky, G. D. *Angew Chem Int Ed Engl* **2004**, *43*, 3037.
- (11) Brinker, C. J.; Scherer, G. W. *Sol-gel Science*, 1990.
- (12) Livage, J.; Henry, M.; Sanchez, C. *Prog. Solid State Chem.* **1988**, *18*, 259.
- (13) Jorgensen, M. R.; Yonkee, B. P.; Bartl, M. H. *Scr. Mater.* **2011**, *65*, 954.
- (14) Galusha, J. W.; Richey, L. R.; Jorgensen, M. R.; Gardner, J. S.; Bartl, M. H. *J. Mater. Chem.* **2010**, *20*, 1277.
- (15) Barhoum, M.; Morrill, J. M.; Riassetto, D.; Bartl, M. H. *Chem. Mater.* **2011**, *23*, 5177
- (16) Galusha, J. W.; Jorgensen, M. R.; Bartl, M. H. *Adv. Mater. (Weinheim, Ger.)* **2010**, *22*, 107.
- (17) John, S. *Phys. Rev. Lett.* **1987**, *58*, 2486.
- (18) Yablonovitch, E. *Phys. Rev. Lett.* **1987**, *58*, 2059.
- (19) Joannopoulos, J. D.; Villeneuve, P. R.; Fan, S. *Nature* **1997**, *386*, 143.
- (20) Mesfin, W.; Sajeev, J. *Journal of Optics B: Quantum and Semiclassical Optics* **2003**, *5*, R43.
- (21) Inui, C.; Tsuge, Y.; Kura, H.; Fujihara, S.; Shiratori, S.; Sato, T. *Thin Solid Films* **2008**, *516*, 2454.
- (22) Inui, C.; Ozaki, S.; Kura, H.; Sato, T. *J. Magn. Magn. Mater.* **2011**, *323*, 2348.

- (23) Koerdt, C.; Rikken, G. L. J. A.; Petrov, E. P. *Appl. Phys. Lett.* **2003**, *82*, 1538.
- (24) Cho, J. H.; Kim, B. Y.; Kim, H. D.; Woo, S. I.; Moon, S. H.; Kim, J. P.; Cho, C. R.; Joh, Y. G.; Kim, E. C.; Kim, D. H. *Physica Status Solidi (b)* **2004**, *241*, 1537.
- (25) Bryan, J. D.; Heald, S. M.; Chambers, S. A.; Gamelin, D. R. *J. Am. Chem. Soc.* **2004**, *126*, 11640.
- (26) Dietl, T.; Ohno, H.; Matsukura, F.; Cibert, J.; Ferrand, D. *Science* **2000**, *287*, 1019.
- (27) Matsumoto, Y.; Murakami, M.; Shono, T.; Hasegawa, T.; Fukumura, T.; Kawasaki, M.; Ahmet, P.; Chikyow, T.; Koshihara, S.-y.; Koinuma, H. *Science* **2001**, *291*, 854.
- (28) Nguyen, H. H.; Prellier, W.; Sakai, J.; Ruyter, A. *J. Appl. Phys.* **2004**, *95*, 7378.
- (29) Wang, H.; Branford, W. R.; Cohen, L. F.; Skinner, S. J.; Ryan, M. P. *Chem. Mater.* **2007**, *19*, 3084.
- (30) Lee, Y. Ph.D Thesis, Enschede, 2010.
- (31) Coey, J. M. D.; Chambers, S. A. *MRS Bulletin* **2008**, *33*, 1053.
- (32) Griffin, K. A.; Pakhomov, A. B.; Wang, C. M.; Heald, S. M.; Krishnan, K. M. *Phys. Rev. Lett.* **2005**, *94*, 157204.
- (33) Chambers, S. A.; Thevuthasan, S.; Farrow, R. F. C.; Marks, R. F.; Thiele, J. U.; Folks, L.; Samant, M. G.; Kellock, A. J.; Ruzycski, N.; Ederer, D. L.; Diebold, U. *Appl. Phys. Lett.* **2001**, *79*, 3467.
- (34) Park, W. K.; Ortega-Hertogs, R. J.; Moodera, J. S.; Punnoose, A.; Seehra, M. S. *J. Appl. Phys.* **2002**, *91*, 8093.
- (35) Wang, C.-C.; Ying, J. Y. *Chem. Mater.* **1999**, *11*, 3113.
- (36) Pereira, L. C. J.; Nunes, M. R.; Monteiro, O. C.; Silvestre, A. J. *Appl. Phys. Lett.* **2008**, *93*, 222502.
- (37) Smith, C. S.; Joseph, N.; Rieger, B.; Lidke, K. A. *Nat Meth* **2010**, *7*, 373.
- (38) Jain, A.; Kumar, J.; Zhou, F.; Li, L.; Tripathy, S. *American Journal of Physics* **1999**, *67*, 714.
- (39) Kett, H.; Gebhardt, W.; Krey, U.; Furdyna, J. K. *J. Magn. Magn. Mater.* **1981**, *25*, 215.

- (40) Crossley, W. A.; Cooper, R. W.; Page, J. L.; van Stapele, R. P. *Physical Review* **1969**, *181*, 896.
- (41) Jacob, D.; Vallet, M.; Bretenaker, F.; Le Floch, A.; Le Naour, R. *Appl. Phys. Lett.* **1995**, *66*, 3546.
- (42) Villaverde, A. B.; Donatti, D. A. *The Journal of Chemical Physics* **1979**, *71*, 4021.
- (43) Spears, T. G. *Handbook of Chemistry and Physics* **2003**, 44691, 1-4.
- (44) Valev, V. K.; Wouters, J.; Verbiest, T. *European Journal of Physics* **2008**, *29*, 1099.
- (45) Visokay, M. R.; Sinclair, R. *Appl. Phys. Lett.* **1995**, *66*, 1692.

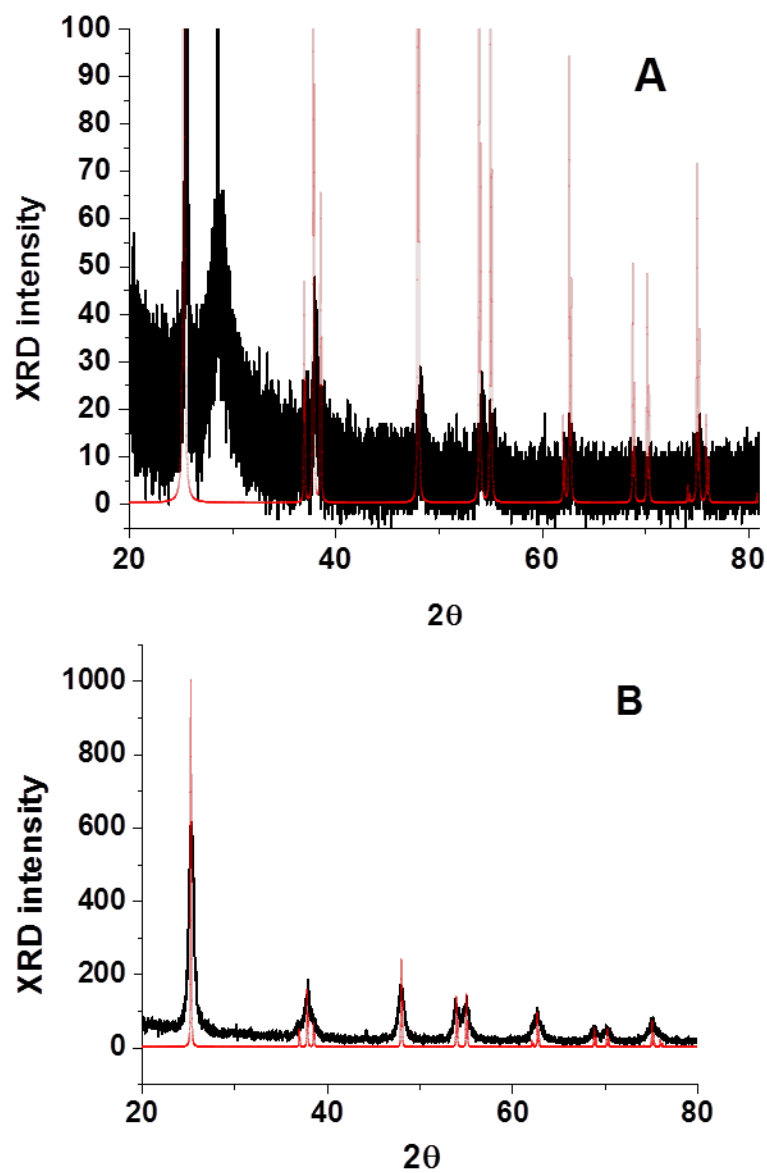


**Figure 5.1:** XRD pattern (black line) for a sol-gel derived  $\text{TiO}_2$  thin film (5.1A) and powder (5.1B) calcined at  $450^\circ\text{C}$  for 3 hours. Simulated XRD patterns of anatase  $\text{TiO}_2$  are additionally plotted for comparison (red spectrum).



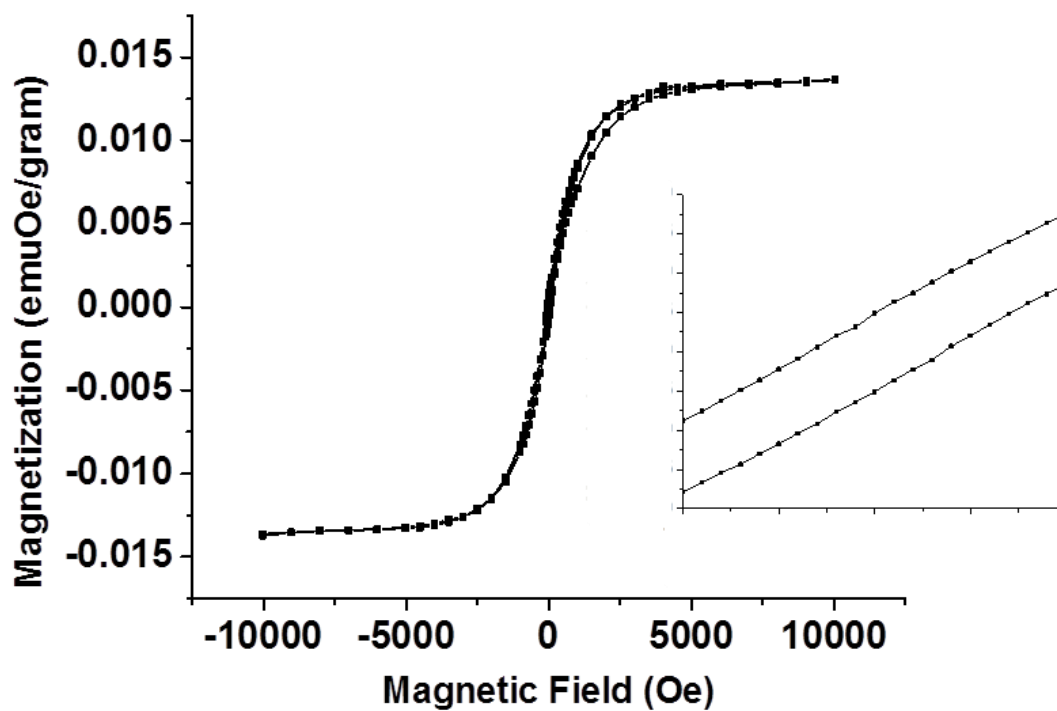


**Figure 5.2:** RT SQUID hysteresis measurement of a 0.5% Co-doped TiO<sub>2</sub> thin-film sample exhibiting a ferromagnetic response. Inset: Zoomed-in region between  $\pm 100$  Oe shows a coercivity of  $\sim 50$  Oersted.

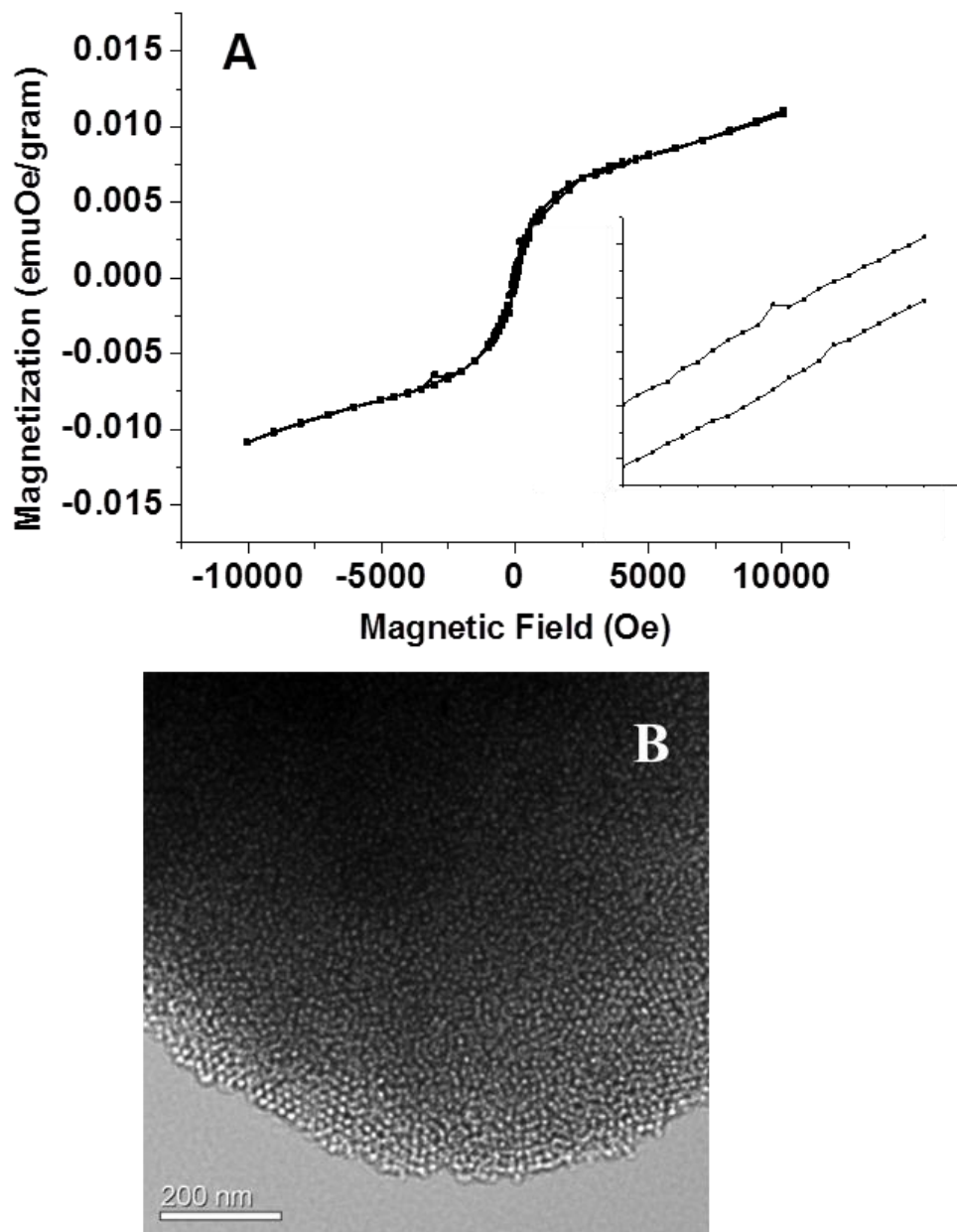


**Figure 5.3:** RT SQUID hysteresis measurements of 0.5% Co-doped mesoporous  $\text{TiO}_2$  thin-film sample exhibiting ferromagnetic response (5.3A). Inset: Zoomed-in region between  $\pm 100$  Oe shows a coercivity of  $\sim 50$  Oersted. (5.3B) TEM image of a mesoporous sol-gel derived  $\text{TiO}_2$  thin-film using Pluronic P123 surfactant chemistry.

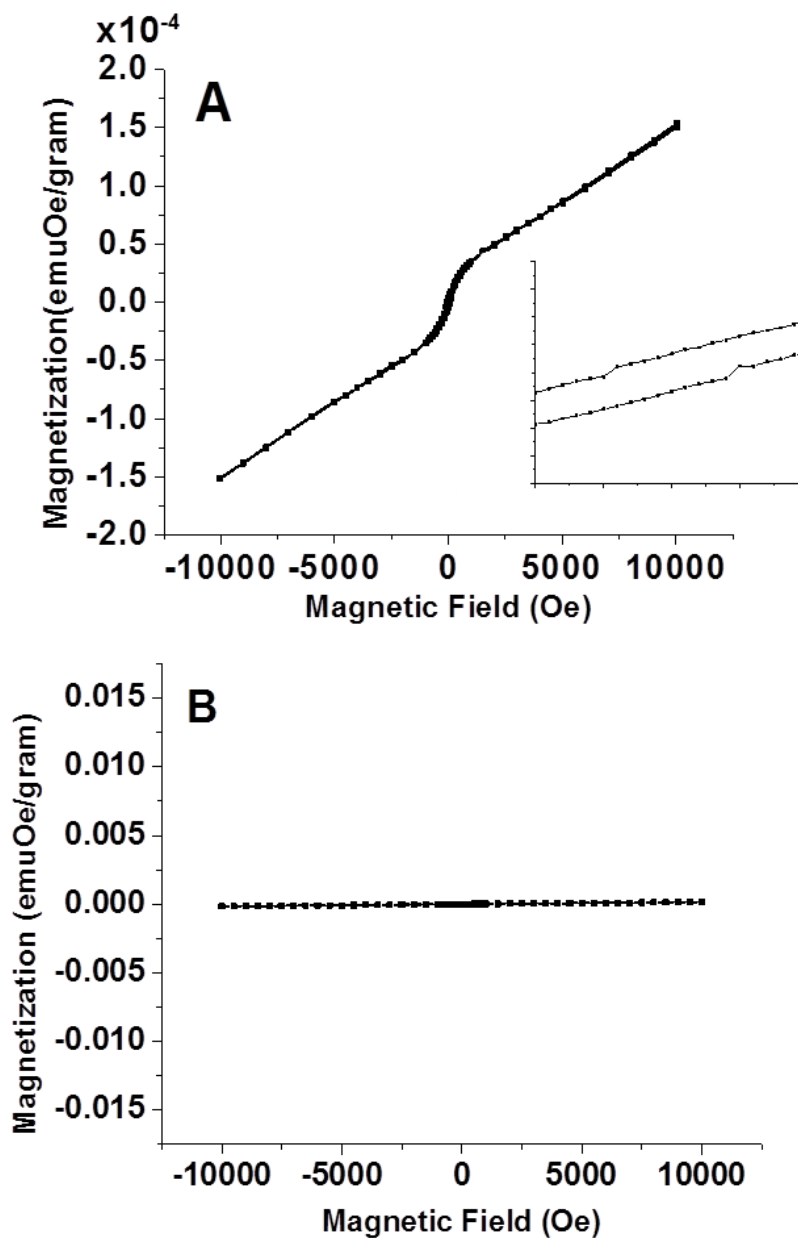


**Figure 5.4:** RT SQUID hysteresis measurements of a 0.5% Co-doped TiO<sub>2</sub> thin-film sample exhibiting ferromagnetic response superimposed on a paramagnetic response(5.4A), and measurement of a 0.5% Co-doped TiO<sub>2</sub> thin-film sample exhibiting a purely paramagnetic response (5.4B). Inset of (5.4A): Zoomed-in region between  $\pm 100$  Oe shows a coercivity of  $\sim 50$  Oersted.

**Table 5.1:** RT-SQUID susceptibility measurements of sol-gel derived 0.5% Co-doped TiO<sub>2</sub>

samples measured at a constant magnetic field of 1000 Oe.

Sample	Mass(g)	Field(Oe)	Temperature (K)	Raw Magnetic Moment (emu,Oe)	Standard Dev (emuOe)	susceptibility per gram	Comment
1%	0.0029	1000	298	-1.56E-05	4.60E-08	-5.38E-06	diam.
	0.0029	1000	298	-1.56E-05	2.72E-08	-5.38E-06	diam.
	0.0029	1000	298	-1.56E-05	4.71E-08	-5.39E-06	diam.
0.50%	0.0035	1000	298	2.80E-05	1.04E-07	8.00E-06	param./ferrom.
	0.0035	1000	298	2.79E-05	1.04E-07	7.99E-06	param./ferrom.
	0.0035	1000	298	2.79E-05	1.26E-09	7.98E-06	param./ferrom.
	0.0035	1000	298	2.78E-05	1.23E-08	7.96E-06	param./ferrom.
0.10%	0.0032	1000	298	1.95E-05	3.85E-08	6.09E-06	param./ferrom.
	0.0032	1000	298	1.96E-05	1.43E-07	6.12E-06	param./ferrom.
	0.0032	1000	298	1.95E-05	1.86E-08	6.09E-06	param./ferrom.

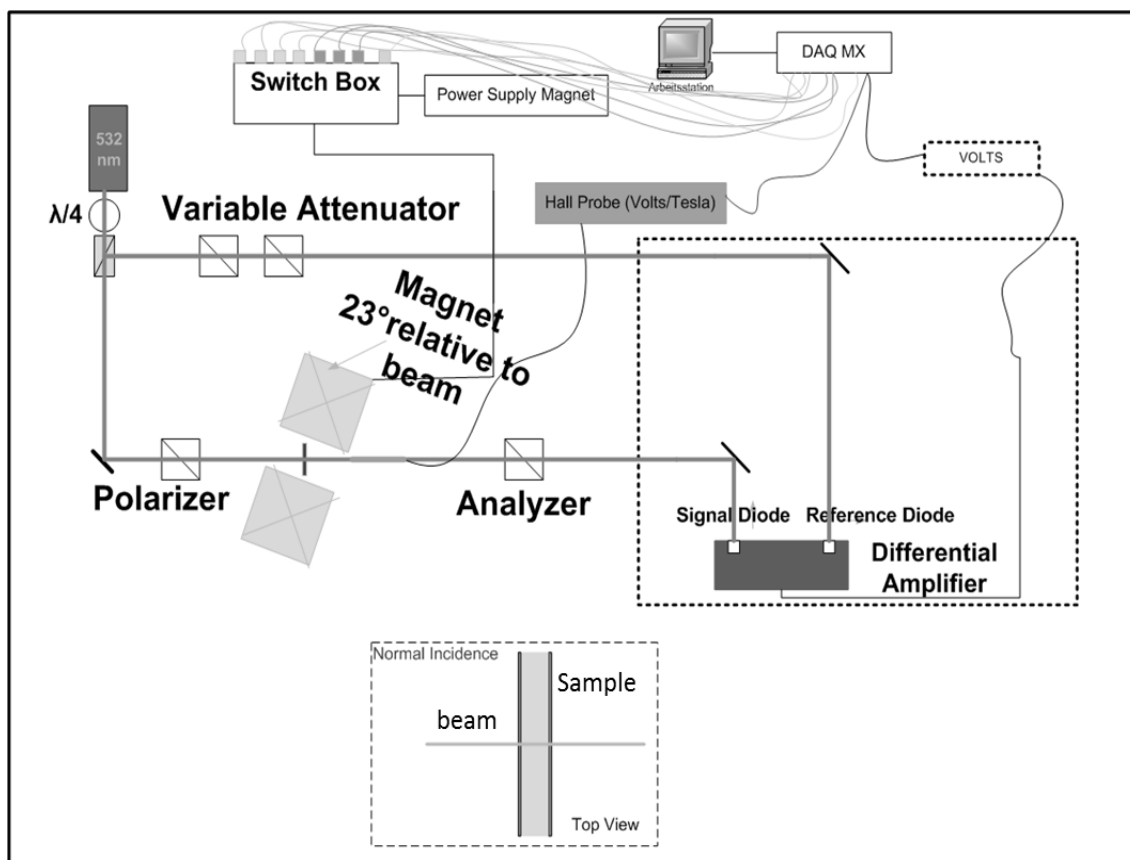


**Figure 5.5:** A schematic diagram of the home-built Faraday rotation setup utilized in the magneto-optical studies of thin films.

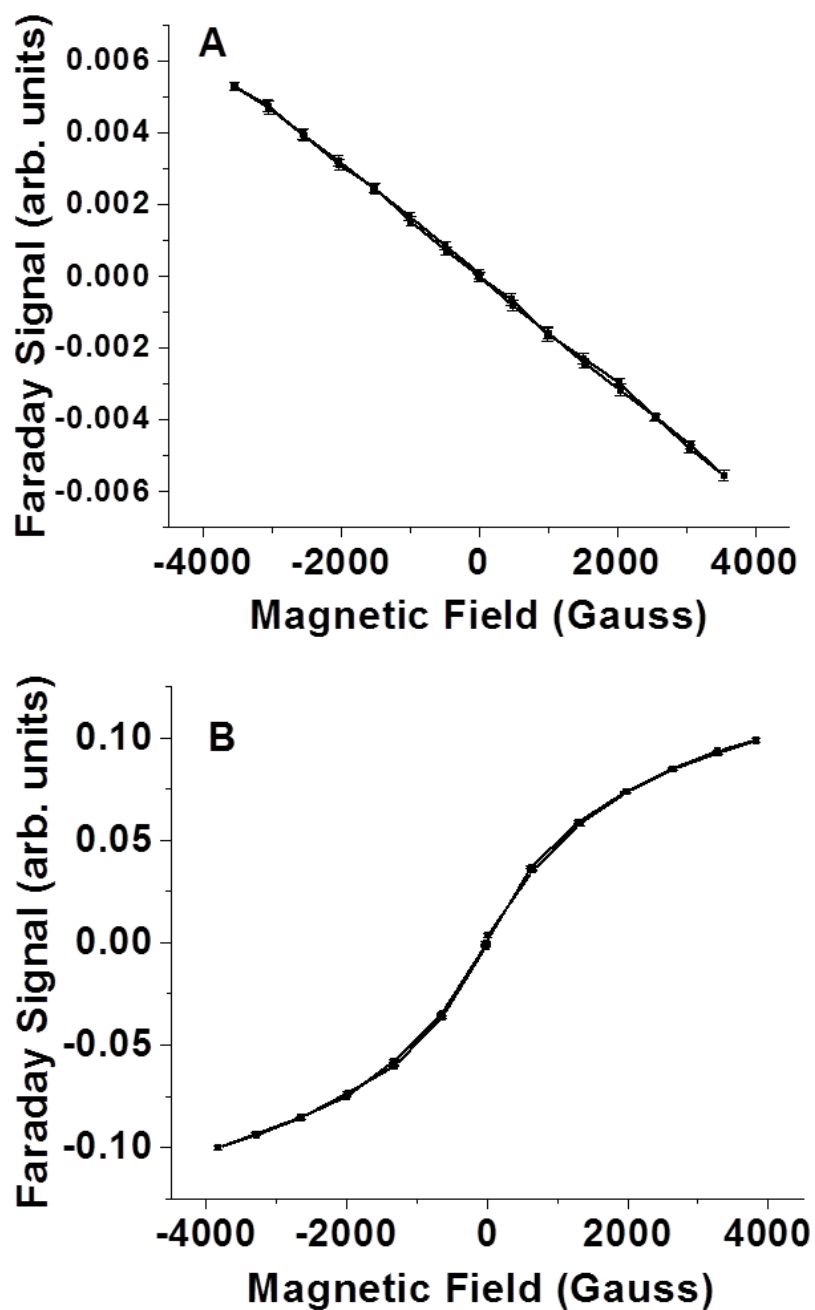


**Figure 5.6:** Magneto-optical measurements of (5.6A) 0.17mm thick VWR glass coverslip and (5.6B) 1nm thick equiatomic CoPt thin-film layer deposited on glass by chemical vapor deposition.

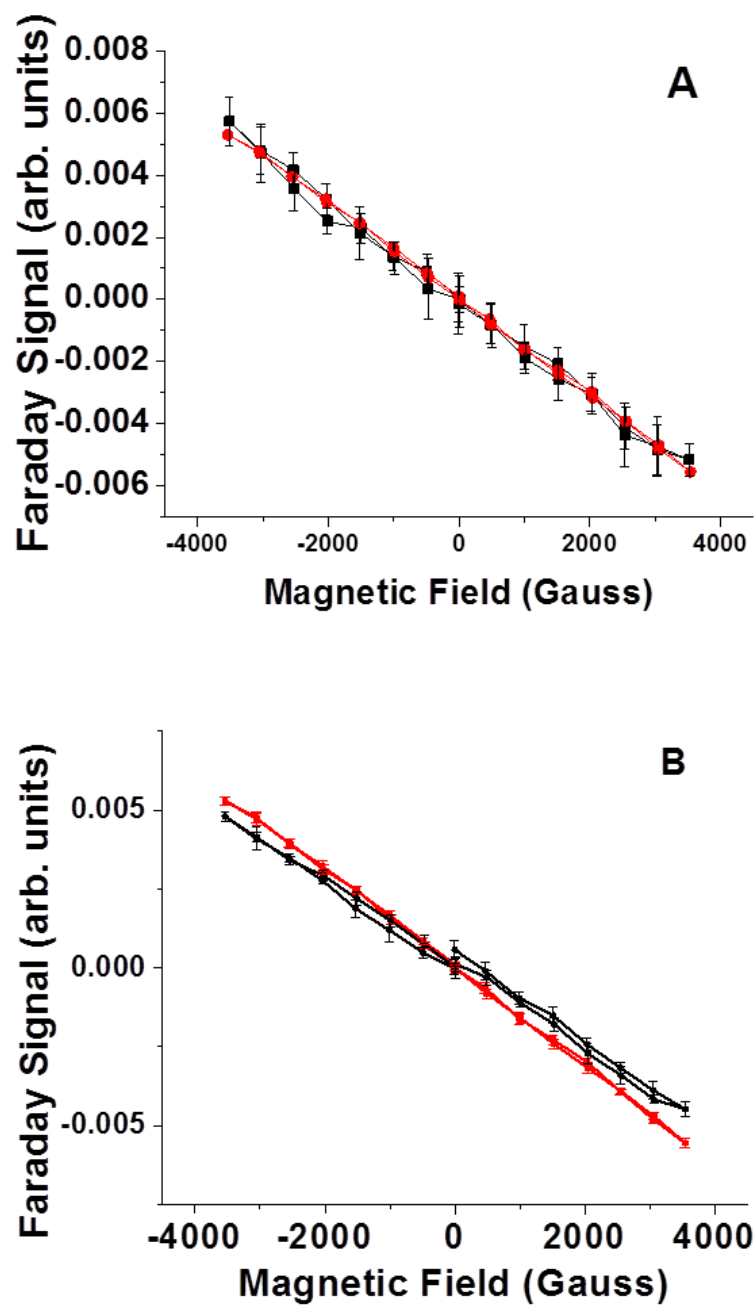


**Figure 5.7:** Faraday-signal comparison of (5.7A) 0.5% Co-doped TiO<sub>2</sub> and (5.7B) 0.5% Mn-doped TiO<sub>2</sub> (both thin-films deposited on glass) to the glass substrate.

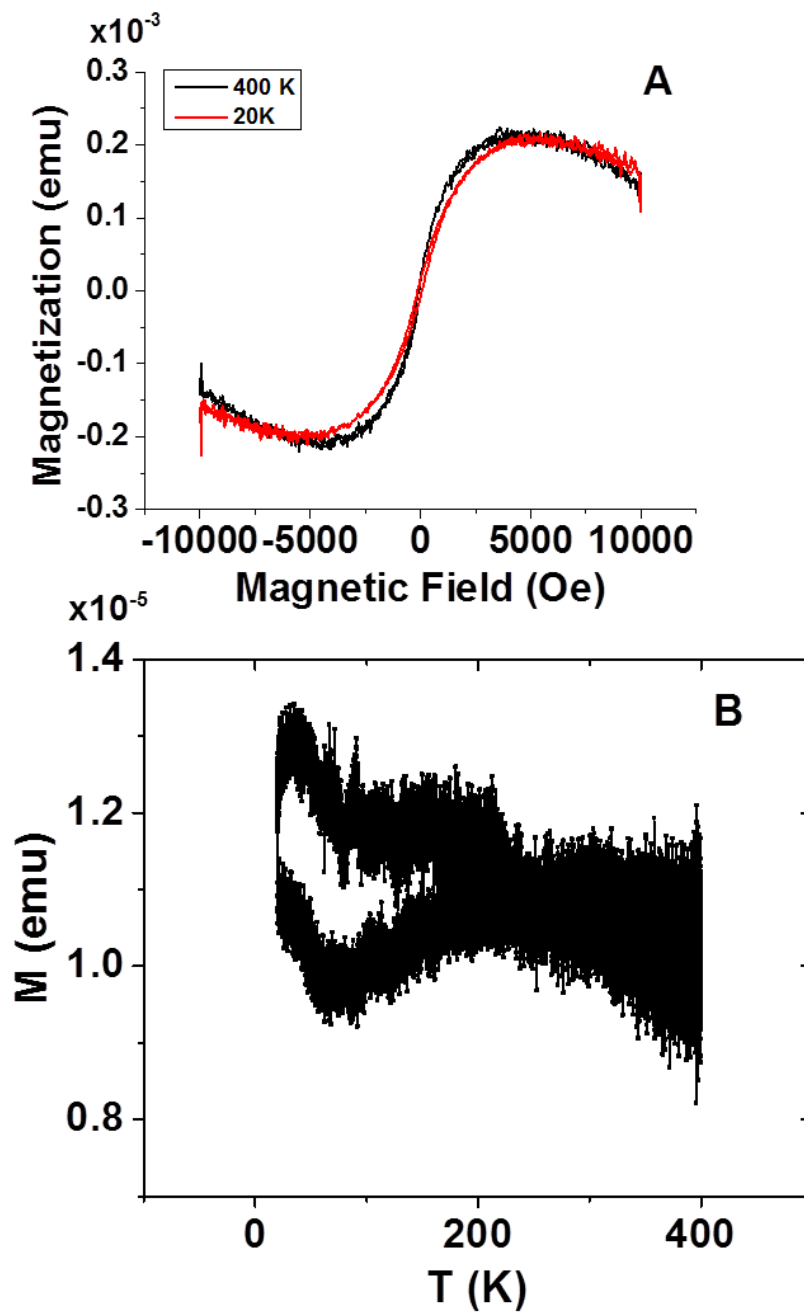


**Figure 5.8:** VSM hysteresis curve measurements at 400K (black) and 20K (red) of 77nm thick TiO<sub>2</sub> thin-film sample deposited on Si (100) waver (5.8A) and field cooling measurements at a constant magnetic field of 1000 Oe (5.8B).



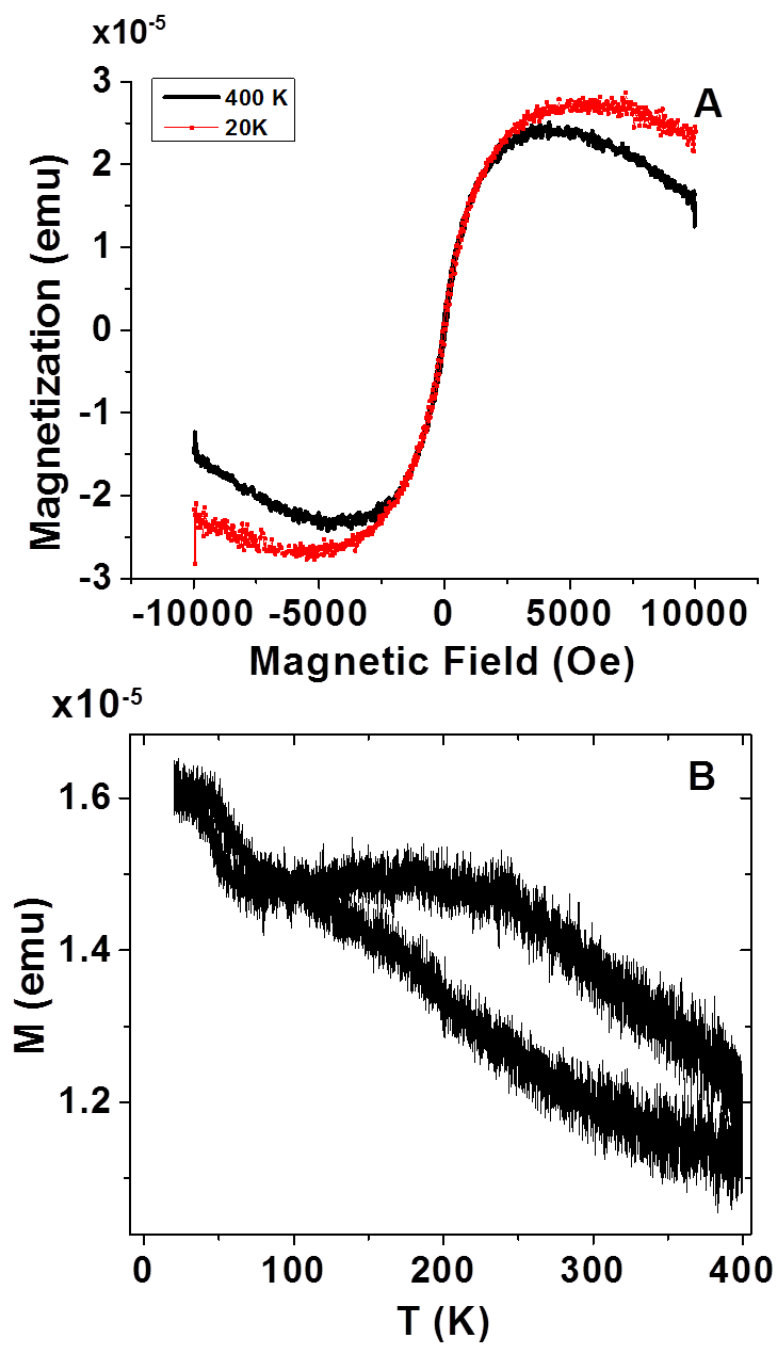


**Figure 5.9:** VSM hysteresis curve measurements at 400K (black) and 20K (red) of 77nm thick 0.5% Co-doped TiO<sub>2</sub> thin-film sample deposited on Si (100) waver (5.9A) and field cooling measurements at a constant magnetic field of 1000 Oe (5.9B).

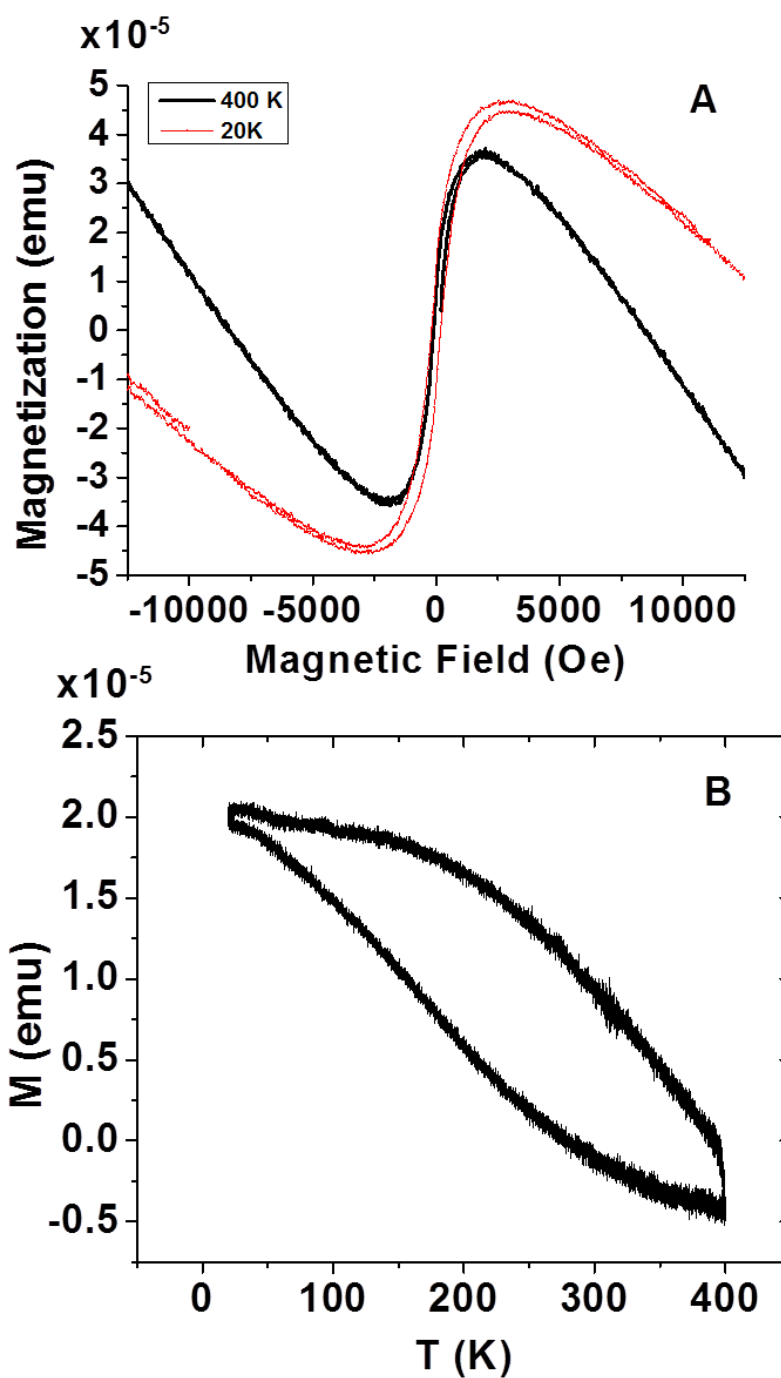


**Figure 5.10:** VSM hysteresis curve measurements at 400K (black) and 20K (red) of 385nm thick 0.5% Co-doped TiO<sub>2</sub> thin-film sample deposited on Si (100) waver (5.10A) and field cooling measurements at constant magnetic field of 1000 Oe (5.10B).

## CHAPTER 6

### SUMMARY AND OUTLOOK

#### 6.1 Summary

The present dissertation encompasses single molecule tracking studies at liquid/solid and liquid/bilayer interfaces, and a sol-gel fabrication process of high-quality one-dimensional photonic bandgap materials, including an attempt to magnetically functionalize them. A brief summary including the scientific significance for each research chapter follows.

Chapter 2 introduced a statistical concept for discerning molecular motion from stationary molecules in single-molecule tracking experiments. This statistical concept was based on Fisher's F-test statistics and includes the computation of local S/N ratios for every single- molecule trajectory point. This combination allowed for establishing upper confidence boundaries in detecting subdiffraction molecular motion in single molecule diffusional trajectories. The statistical criteria were used in investigating diffusion of single DiI molecules on planar supported 1,2-Dimyristoyl-sn-glycero-3-phosphocholine (DMPC) bilayers at different temperatures, and was demonstrated to be useful in detecting and evaluating confined subdiffraction-diffusion events. Furthermore, the

incorporation of local S/N ratios in automated tracking software allowed detection of diffusional heterogeneities which are often accompanied with a change in the local S/N of the probe molecule.

In Chapter 3 the same single-molecule tracking concept was used in differentiating subdiffraction diffusional confinement events from stationary single Rhodamine6G molecules in polymer brushes of poly (N-isopropylacrylamide), pNIPAAm, above its lower critical solution temperature (LCST) of 32°C. The study reports the detection of increased fraction for subdiffusional confinement events above pNIPAAm's LCST compared to diffusional trajectories below its LCST. The statistical criteria for detecting subdiffraction molecular motion were determined to be crucial in examining nanometer sized hydrophobic compartments in polymer brushes.

Chapter 4 details the optimization of a sol-gel dip-coating process for the fabrication of high-quality one-dimensional photonic band-gap materials. A crucial finding in this study was the incorporation of a shock-cooling step immediately following the calcination step in the sol-gel deposition cycle. This shock-cooling step enables fabrication of sol-gel derived one-dimensional photonic bandgap materials of outstanding optical and structural quality, rivaling other cost-intensive deposition methods. This chapter further discussed crack formation sources during the various steps of thin-film formation, and provided strategies to counteract or suppress these unwanted processes. These findings will be of great importance in establishing sol-gel thin-film deposition methods as a serious alternative to traditional high-vacuum deposition methods.

Chapter 5 described an attempt to measure magnetic and magneto-optical properties of Co-doped titania thin films. The reasoning for investigating Co-doped

titania compounds was based on a recent finding of room-temperature ferromagnetism in these systems. A home-built magneto-optical Faraday rotation measurement setup was assembled to study these magnetic films in concert with SQUID and VSM methods. However, it was found that irregularities in magnetization measurements made the interpretation of our results difficult. We were not able to identify a clear trend, despite our efforts in excluding any possible contamination source that could give rise to a magnetic signal during the sol-gel deposition process. Furthermore, the detection sensitivity of our home-built Faraday rotation setup was too low for detecting any reliable Faraday effects in these potentially magnetic functionalized thin-films. The conclusion of this research effort is perhaps best described in a recent paper titled “Oxide Dilute Magnetic Semiconductors-Fact or Fiction” in which the author discusses the difficulty of measuring ferromagnetism from dilute magnetic semiconductors.<sup>1</sup> The paper concludes further that the irregularities in measuring ferromagnetic signals in dilute magnetic semiconductor materials result from the formation of uncontrolled secondary phases. We further presented preliminary data on an alternative sol-gel magnetic-functionalization method by synthesizing Fe<sub>3</sub>O<sub>4</sub> nanoparticles within titania or silica thin-film host without the need of prior functionalization of these magnetic particles.

## 6.2 Outlook

Current research efforts are focused on the statistical characterization of hop events within single molecule diffusional trajectories. Our strategy in identifying single molecule hops is based on an extended single molecule tracking method. The position of the Gaussian centroid, and the local S/N (yielding the spot size) of the diffracted limited

single molecule image is computed. Preliminary results of this trajectory analysis method on single DiI-C<sub>18</sub> fluorophores diffusing on C<sub>18</sub>-chromatographic interfaces at different solvent compositions allows for distinguishing two different diffusion mechanisms: first, a hopping diffusion mechanism in which the average spot size of the fluorophore is smaller than its step size for a given image frame, and second, a continuous diffusion mechanism with overlapping spot sizes much larger than its step size for a given image frame. Statistical criteria were established for reliably detecting hop events and quantifying population occupancy of the competing mechanisms. Trajectory analysis of the single molecules in varying solvent compositions at the C<sub>18</sub>-chromatographic interfaces could provide insight into the previously observed trend of the mean diffusion coefficients for conventionally tracked (reporting only x,y –positions) DiI molecules under similar conditions.<sup>2</sup>

A simultaneously ongoing research effort is focused in the magnetic functionalization studies of sol-gel derived thin films. This study conducted in collaboration with Prof. Karine Chesnel (Brigham-Young-University) investigates the feasibility of synthesizing Fe<sub>3</sub>O<sub>4</sub> nanoparticles within titania and silica thin-film host without the need of prior functionalization of these magnetic particles. Preliminary vibrating sample magnetometer measurements suggest a successful one pot in-situ formation of these super-paramagnetic nanoparticles within the titania and silica hosts.

### 6.3 References

- (1) Coey, J. M. D.; Chambers, S. A. *MRS Bulletin* **2008**, *33*, 1053.
- (2) Barhoum, M., *Diplom-Thesis*, TU-Braunschweig, 2006.